UNIVERSIDADE ESTADUAL DE CAMPINAS

INSTITUTO DE QUÍMICA

NAIARA VIEIRA GODOY

PRODUCTION OF PAPER-BASED SERS SUBSTRATES BY INKJET-PRINTING METHOD

PRODUÇÃO DE SUBSTRATOS SERS A BASE DE PAPEL PELO MÉTODO *INKJET-PRINTING*

CAMPINAS
2020

NAIARA VIEIRA GODOY

PRODUCTION OF PAPER-BASED SERS SUBSTRATES BY INKJET-PRINTING METHOD

PRODUÇÃO DE SUBSTRATOS SERS A BASE DE PAPEL PELO MÉTODO *INKJET-PRINTING*

Tese de Doutorado apresentada ao Instituto de Química da Universidade Estadual de Campinas como parte dos requisitos exigidos para a obtenção do título de Doutora em Ciências.

Doctor's Thesis presented to the Institute of Chemistry of the University of Campinas as part of the requirements to obtain the title of Doctor in Sciences.

Supervisor: Dr. Italo Odone Mazali

O arquivo digital corresponde à versão final da Tese defendida pela aluna Naiara Vieira Godoy e orientada pelo Prof. Dr. Italo Odone Mazali.

CAMPINAS
2020

Ficha catalográfica
Universidade Estadual de Campinas
Biblioteca do Instituto de Química
Simone Luiz Alves - CRB 8/9094

G548p

Godoy, Naiara Vieira, 1991-
Production of paper-based SERS substrates by inkjet-printing method / Naiara Vieira Godoy. – Campinas, SP : [s.n.], 2020.

Orientador: Italo Odone Mazali.
Tese (doutorado) – Universidade Estadual de Campinas, Instituto de Química.

1. Nanopartículas metálicas. 2. Quantificação. 3. Impressão a jato de tinta. 4. Sensor. 5. Espalhamento Raman intensificado por superfície. I. Mazali, Italo Odone, 1972-. II. Universidade Estadual de Campinas. Instituto de Química. III. Título.

Informações para Biblioteca Digital

Título em outro idioma: Produção de substratos SERS a base de papel pelo método *inkjet-printing*
Palavras-chave em inglês:
Metal nanoparticles
Quantification
Inkjet printing
Sensor
Surface-enhanced Raman scattering
Área de concentração: Química Inorgânica
Titulação: Doutora em Ciências
Banca examinadora:
Italo Odone Mazali [Orientador]
Paulo Cesar de Sousa Filho
Juliano Alves Bonacin
Mariana Ramos de Almeida
Alexandre Guimarães Brolo
Data de defesa: 21-09-2020
Programa de Pós-Graduação: Química

Identificação e informações acadêmicas do(a) aluno(a)
- ORCID do autor: https://orcid.org/0000-0002-8172-0821
- Currículo Lattes do autor: http://lattes.cnpq.br/7212880086414531

BANCA EXAMINADORA

Prof. Dr. Italo Odone Mazali (Orientador)

Profa. Dra. Mariana Ramos de Almeida (Departamento de Química – UFMG)

Prof. Dr. Alexandre Guimarães Brolo (Chemistry Department – University of Victoria)

Prof. Dr. Paulo Cesar de Sousa Filho (Instituto de Química – UNICAMP)

Prof. Dr. Juliano Alves Bonacin (Instituto de Química – UNICAMP)

A Ata da defesa assinada pelos membros da Comissão Examinadora, consta no SIGA/Sistema de Fluxo de Dissertação/Tese e na Secretaria do Programa da Unidade.

Este exemplar corresponde à redação final da Tese de Doutorado defendida pela aluna **NAIARA VIEIRA GODOY**, aprovada pela Comissão Julgadora em 21 de setembro de 2020.

To my parents Ana Maria and Simão, who worked hard to support me and my dreams.

ACKNOWLEDGMENTS

To God for all the blessings in my life. Thank you for always listening to my sorrows, guiding me through difficult times, and being the source of my strength. To the Virgin Mary who intercedes for her beloved daughter and enlights my path.

To my parents Ana Maria and Simão, who are my fortress. Thank you for being so supportive and understandable about my dreams and desires. Thank you for the hard work to provide me the best education. Thank you for trying your best to make sure that I had love and all the opportunities. Also, I would like to thank my sister Meiriele for being there when I needed, for sharing great moments, for all the good talks, and give me the other two persons that I love the most, my brother-in-law João Roberto and my niece Kauane. João, thank you for all the good and funny talks, and for being a great man. Kauane, thank you for being a shining light in my life. I love you all.

To Dr. Italo Odone Mazali for supervising me during all these years. I am grateful for your support, especially during the most difficult times. I will always fondly remember our talks. You taught me that a dose of diplomacy is always welcome, mainly when it is hard to do so. You proved that leadership walks side by side with kindness. I hope that our friendship lasts a lifetime. And do not forget, I can beat you in a racing car.

To Dr. Fernando Aparecido Sigoli for all the teaching and jokes. I am grateful for our moving and inspiring talks. On many occasions, I felt like you were advising your own daughter. I will always remember that, once, you told me that life is like a river that we are navigating. Sometimes we face a wall and we are afraid to go through it without knowing what is on the other side. However, sometimes the garden on the other side has more beautiful flowers than the side that we know. We must have courage. I am very grateful for your friendship.

To Dr. Isabel Pastoriza-Santos and Dr. Jorge Pérez-Juste who received and supervised me during the student exchange program in Colloid Chemistry Group (Vigo, Spain). Thank you for being so supportive and friendly to me. I am sure that my experience in your group changed my way to see science and life itself. I would like to thank everybody that I met in the group for always being friendly to me. Thank you for all the chats, coffees, and great meals that we shared. I would particularly like to thank

Dany for being so friendly, kind, and supportive during the time that we worked together. I am very grateful for your friendship, you certainly help me in moments that you don't even know. So, like always, *Gracias cariño*.

To Dr. Marco Aurélio Zezzi Arruda for opening his laboratory's door and supervising me during our collaborative work. I am grateful for the teachings and fun talks. I am grateful to Rodrigo for being so friendly and professional during the development of our work. I am also grateful to Katherine for being a great coworker and becoming a dear friend. I would like to thank Pedro and Daniel for helping me without asking anything in return, and being so friendly to me.

To all my colleagues from the Laboratory of Functional Materials (LMF): Gabi, Jorge, João, Emille, Cris, Filipe, Rafael, Diogo, Isaías, Carla, Lidiane, Murilo, Bia, Lanousse, Josi, Laura, Gilmar, William, Ane, Adriana, Alice, Amanda, Isa, Flávia, Jaci, Gesi, Raisa, Deborah, Rafa, Raul, Edison, Rodrigo, Tainá, Geovanna, Hana, Lohana, Sérgio, and Claudia. Thank you for all the help and happy moments. Thank you for teaching me so much about chemistry, science, life, and humanity. Thank you for being my family during these years. Thank you for constantly listening to my complaints (and not shut me up). Thank you for being understandable when I needed and celebrating my wins. My win is also yours. Quoting one of my *bests*: "you were formidable".

To my dear friends that life gave me during my Ph.D.: Lanousse, Flávia, Raisa, Ane, Josi, Amanda, Emille, Diogo, Raul, Jorge, Gabi, Yuri, Mayara, Murilo, Bia, and Isaías. Thank you for letting me into your lives and be part of mine. Thank you for all the encouraging chats, listening to my sorrows, many and many laughs, and great meals that we shared. Your friendship is my most precious achievement.

To Raul for your surprising and refreshing friendship. I certainly learned a lot with you about science and even more about life. Thank you for being a funny and sweet *copain*.

To Lanousse for being such a good friend, and one of my best ones. I appreciate our discussions, chats, running workouts, and your advice. You are an inspiration.

To Amanda, Raisa, and Emille for your funny and lovely friendship. Thank you for making my life lighter, and fighting my fights with me. Thank you for your kindness, and for being powerful women.

To my beloved soul sisters Flávia, Josi, and Ane. You celebrated my wins and dried my tears (usually with a gin, beer, or wine for both cases). You walked by my side through my darkest times. You listened to my sorrows and my silence. You encouraged and rebuked me when I needed it. You took care of me as older sisters when my heart was broken and after many glasses of wine. You helped me to dream and fly. I will always treasure our friendship. Thank you for just being yourself. You are my inspiration.

To all my friends from Dysprosium Team for being so friendly and awesome. Thank you for waiting for me during our running workouts. Thank you for patiently listening to my complaints. Thank you for not letting me give up.

To Bruna and Jeferson for more than ten years of sincere friendship. For always being by my side, even when the distance separated us. For all the jokes, chats, and happy moments. I also would like to thank Allan for your friendship, patience, and laughs.

To my grandparents, cousins, uncles, and aunts who always cheered for my success. For all the wisdom that you shared and the happy moments that made my life lighter. I especially thank my uncle Luiz, aunt Eunice, and my cousins Luiz, Stefanie, and Ada for being my family in Campinas. Thank you for all the help, chats, and happy meals.

To Cláudia, Milene, Sônia, and Douglas for being great professionals and being so helpful during our time together. I am also grateful for the sweet friendship that we developed over these years.

To all the staff of the Institute of Chemistry (UNICAMP) for being friendly and helpful.

To Psychologist Mariana Soares, who help me to see the light in my darkest times. My own light. I will always be grateful for her professionalism, kindness, and patience. I will always remember her sweet, powerful, and harsh words.

This study was financed in part by the Coordenação de Aperfeiçoamento de Pessoal de Nível Superior - Brasil (CAPES) - Finance Code 001.

To Santander Bank for the scholarship provided by "*Programa Santander de Bolsas de Mobilidade Internacional*".

To Conselho Nacional de Desenvolvimento Científico e Tecnológico (CNPq) for financial support.

To Fundação de Amparo à Pesquisa do Estado de São Paulo (FAPESP) for financial support.

I will always remember my failures and defeats to remind myself that I can always stand up and fight for my wins.

Naiara Vieira Godoy

RESUMO

Nesse trabalho, foi reportado um conjunto completo de estratégias de caracterização e aplicação de nanopartículas metálicas. Primeiro, uma plataforma de decomposição assistida por micro-ondas foi desenvolvida para a quantificação de ouro em nanopartículas metálicas com matrizes complexas com alto teor de matéria orgânica. Para isso, um colóide de nanobastões de ouro (AuNR) com elevado teor de brometo de hexadeciltrimetilamônio (CTAB) foi sintetizado. A decomposição assistida por micro-ondas de pequeno volume de amostra (200 µL) com uma mistura ácida de água régia invertida (1:3 v/v, $HCl:HNO_3$) e H_2SO_4 proporcionou a quantificação precisa de ouro no colóide por ICP OES e ICP-MS. Além disso, o procedimento de decomposição proposto também foi eficiente na decomposição de colóides de nanoesferas de ouro (AuSph) e nanobastões caroço-casca do tipo ouro-prata (Au@AgNR). O primeiro apresenta elevado teor de CTAB enquanto o último apresenta elevado teor de polivinilpirrolidona (PVP) em adição à matriz com CTAB. A plataforma de decomposição assistida por micro-ondas proposta demonstrou ser uma ferramenta de caracterização eficiente e robusta para a quantificação de ouro em nanopartículas metálicas, não apresentando interferência da matriz complexa com alto teor de matéria orgânica. A segunda parte do trabalho engloba a fabricação de um sensor a base de papel de baixo custo para detecção por Espectroscopia Raman intensificada por superfície (SERS, do inglês *surface-enhanced Raman scattering spectroscopy*). O sensor SERS a base de papel foi fabricado a partir do desenvolvimento de uma tinta efetiva de nanopartículas AuSph e com o emprego do método *inkjet-printing*. O sensor consiste em uma dispersão de glicerol/etanol com elevada concentração de AuSph impressas em papel cromatográfico hidrofóbico na forma de círculos com cerca de 1 mm de diâmetro. O efeito da quantidade de nanopartículas na performance SERS dos sensores foi avaliada pelo ajuste de número de ciclos de impressão e concentração de nanopartículas da tinta. Os resultados mostram que a combinação da tinta AuSph com a concentração de ouro de 113 mmol L^{-1} (em termos de Au^0) e 5 ciclos de impressão originou sensores com excelente resposta SERS em termos de reprodutibilidade e sensibilidade. O sensor SERS a base de papel foi testado na detecção da molécula sonda cristal violeta (CV) e o fungicida thiram. Para ambos os analitos, 10^{-11} mol L^{-1} foi a menor concentração quantificada. O substrato SERS impresso demonstrou ser eficiente, reprodutível e robusto, com um custo menor que $ 0,01 (ou R$ 0,03) por *spot* (considerando somente os consumíveis).

ABSTRACT

In this work, it is reported a complete set of strategies for characterization and application of metallic nanoparticles. First, a microwave-assisted decomposition platform was developed for the gold quantification metallic nanoparticles with complex matrices and a high content of organic matter. For this, gold nanorods (AuNR) colloid with a high content of hexadecyltrimethylammonium bromide (CTAB) was synthesized. The microwave-assisted decomposition of a low sample volume (200 µL) with an acidic mixture of reverse *aqua regia* (1:3 v/v, HCl:HNO_3), and H_2SO_4 provided an accurate gold quantification in AuNR colloid by ICP OES and ICP-MS. The proposed platform was also efficient in the decomposition of the gold nanospheres (AuSph) and gold-silver core-shell nanorods (Au@AgNR). The first presents a high content of CTAB while the latter presents a high content of polyvinylpyrrolidone (PVP) in addition to the matrix with CTAB. The proposed microwave-assisted decomposition platform demonstrated to be an efficient and robust characterization tool for the gold quantification in the metallic nanoparticles, presenting no interference of the complex matrix with high organic content. The second part of the work involves the fabrication of a low-cost paper-based sensor for SERS (surface-enhanced Raman scattering spectroscopy) detection. The paper-based SERS sensor was fabricated by developing an effective AuSph Ink and using the inkjet-printing method. The sensor consists of a highly concentrated glycerol/ethanol dispersion AuSph inkjet-printed on hydrophobic chromatographic paper forming circular sensing spots of ca. 1 mm in diameter. The effect of the amount of the nanoparticles in the SERS performance of the plasmonic spots was analyzed by tuning the number of printing cycles and nanoparticle concentration of the ink. The results show that the combination of AuSph Ink with a gold concentration of 113 mmol L^{-1} (terms of Au^0) and 5 printing cycles gave rise to sensing platforms with great SERS response in terms of reproducibility and sensibility. The paper-based SERS sensor was tested towards the detection of the probe molecule crystal violet (CV) and the fungicide thiram. For both analytes, 10^{-11} mol L^{-1} was the lowest quantified quantification. The inkjet-printed SERS substrate demonstrated to be efficient, reproducible, and robust, with a cost less than $ 0.01 (or R$ 0.03) per spot (considering only consumables).

LIST OF FIGURES

LIST OF TABLES

LIST OF ABBREVIATIONS

2D-CCD	2D-charge coupled device
4-NBT	4-nitrobenzenethiol
a.u.....	Arbitrary units
AuSeed.....	Gold seed
AuSph.....	Gold nanosphere
CA.....	Contact angle
CE.....	Chemical enhancement
CTAB	Cetyltrimethylammonium bromide
cts	Counts
CV.....	Crystal Violet
DDSA.....	(2-dodecen-1-yl)-succinic anhydride
EF	Enhancement factor
EM	Electromagnetic enhancement
EPA	Environmental Protection Agency
ICP OES	Inductively coupled plasma optical emission
ICP-MS	Inductively coupled plasma mass spectrometry
IUPAC.....	International Union of Pure and Applied Chemistry
LOD	Detection limit
LOQ	Quantification limit
LSPR	Localized surface plasmon resonance
MNP.....	Metallic nanoparticle
NIR	Near-infrared
PoC.....	Point-of-care
ppb.....	Parts-per-billion
ppm.....	Parts-per-million

ppt	Parts-per-trillion
RSD	Relative standard deviation
SEF	Surface-enhanced fluorescence
SEIRA	Surface-enhanced infrared absorption
SEM	Scanning electron microscopy
SERS	Surface-enhanced Raman spectroscopy/scattering
SM-SERS	Single-molecule surface-enhanced Raman scattering
TEM	Transmission electron microscopy
UV	Ultraviolet
VIS	Visible

LIST OF SYMBOLS

a	Radius
$[Au^+]$	Concentration of ions Au^+
$[Au^0]_{Ink}$	Au^0 concentration of the AuSph Ink
$[Seed]$	Concentration of gold seed
d_{Au}	Density of gold
D_{final}	Final diameter of the gold nanosphere
D_{Seed}	Diameter of the gold seed
D_{sphere}	Average diameter of the gold nanosphere
E_0	Electric field of the incident electromagnetic radiation
E_i	Energy of the incident photon
E_{out}	Electric field outside the metallic nanoparticle
h	Planck's constant
E_R	Energy of the Rayleigh scattered photon
E_{RAS}	Energy of the anti-Stokes Raman scattered photon
E_{RS}	Energy of the Stokes Raman scattered photon
I_0	Incident photon flux
I_{Raman}	Intensity of the Raman band/Raman scattering
I_{SERS}	Intensity of the SERS band
$m_{Au/NP}$	Mass of Au^0 per nanoparticle
Mm	Molar mass
N_{surf}	Number of adsorbed molecules in the scattering volume for the SERS experiment
N_{vol}	Number of molecules in the scattering volume of the Raman experiment
ø	Aromatic ring
r	Distance

V_{Au+} ..... Volume of precursor Au^{+}

V_{final} ..... Reaction volume

V_{Seed} ..... Volume of gold seed

V_{Sphere} ..... Volume of a sphere

x, y, and z ..... Cartesians coordinates

$\hat{x}$, $\hat{y}$, and $\hat{z}$ ..... Vectors units

α ..... Polarizability

δ ..... Deformation mode

δ_{as} ..... Asymmetric deformation mode

δ_{s} ..... Symmetric deformation mode

ε_0 ..... Dielectric constant of the surrounding medium

ε_1 ..... Real component of the dielectric function

ε_1 ..... Imaginary component of the dielectric function

λ ..... Wavelength

μ_{ind} ..... Induced dipole moment

ν_i ..... Frequency of an incident photon

ν_v ..... Frequency of a molecular vibrational transition

ν_{as} ..... Asymmetric stretching mode

ν_s ..... Symmetric stretching mode

ν_{st} ..... Stretching mode

ρ ..... Rocking mode

σ_{ext} ..... Extinction cross-section

σ_{RS} ..... Raman cross-section

ω ..... Angular frequency

ω_i ..... Angular frequency of an incident photon

ω_{RS} ..... Angular frequency of a molecular vibrational transition

SUMMARY

THESIS SCOPE

The search for analytical methods that allow the detection of analytes at low concentrations and present simple and convenient operation, being portable, cost-efficient, and fast, is one of the main goals of several researchers and companies nowadays, particularly considering the technological and sustainable today's world.

Surface-enhanced Raman Spectroscopy (SERS) is a vibrational technique capable of detecting molecules adsorbed or near to plasmonic nanostructures at ultralow concentrations. As the main advantages, it allows the vibrational discernible fingerprint of molecules and may achieve detection limits as low as femto- and attomolar. The high sensitivity makes the surface-enhanced Raman spectroscopy a highlighted analytical tool for qualitative and quantitative purposes and a versatile technique for applications in several fields of interest, such as food safety, environmental monitoring, clinical diagnostics, and drugs detection.

Since its first observation in 1974, the number of publications concerning the SERS effect has dramatically increased, achieving more than 40,000 publications up to September 2020*. The increasing interest in the SERS field may be associated with the instrumentation improvement of the Raman spectrometers as well as the evolution of the Nanotechnology with the improvement of nanofabrication techniques. Studies of the SERS effect present promising growth, encompassing several areas of knowledge such as *Materials Science*, *Chemistry*, *Surface Science*, *Physics*, *Optics*, and *Nanotechnology*, among others.

The demand to understand the physical and chemical effects that concern the SERS effect drives the research of the field together with the development of high throughput, facile, and cost-effective fabrication methods of new SERS platforms. For the fabrication of SERS platforms, several challenges need to be overcome, such as high yield synthesis and great stability of the nanoparticle colloid, effective deposition method, obtainment of reproducible hot spots, and high efficient optical enhancing capabilities.

* A Search in Web of Science as "surface enhanced Raman (topic) or SERS (topic)" in September 2020.

In this context, this thesis focuses on the search for a low-cost and robust SERS substrate that provides reproducible and accurate analysis of molecules of interest at ultralow concentrations. A complete set of strategies for the characterization of metallic nanoparticles and fabrication of a low-cost paper-based SERS platform is reported.

The thesis is structured in a total of four chapters. Chapter 1 presents a general introduction concerning the plasmonic nanoparticles and their optical properties, Raman and SERS scattering theory, and the fabrication of SERS sensors and subjects related to it. The aim of Chapter 1 is to introduce the readers to the theory of the subjects approached in this thesis as well as address a brief overview of the issues related to the production and application of SERS sensors. Chapters 2 and 3 are organized in the introduction, experimental section, results and discussion, conclusions, cRediT authorship contribution statement, and acknowledgments. The introduction of each chapter addresses specific topics related to the subject matter, presenting an overview of the state-of-the-art of the field. Each chapter also has an associated-appendix at the end of the thesis.

Chapter 2 presents the development of a microwave-assisted decomposition procedure coupled with plasma-based spectrometric techniques for the gold quantification in gold and gold-silver core-shell nanoparticles in complex matrices with a high content of organic matter. The decomposition strategy is proposed as a characterization tool for the gold quantification in single- and multi-elemental nanoparticle colloids.

Chapter 3 presents the fabrication of a high-performance gold nanosphere ink and its use in the manufacturing of an ultrasensitive plasmonic hydrophobic paper-based SERS platform by the inkjet printing method. The proposed inkjet-printed SERS substrate together with a recently developed digital protocol allowed the quantification of the probe molecule crystal violet and the fungicide thiram at ultralow concentrations while working in the single-molecule SERS regime. The inkjet printing method in conjunction with the characteristics of the ink proved to be a low-cost, efficient, reliable, and robust fabrication method for highly sensible and reproducible paper-based SERS sensors.

Chapter 4 summarizes general concluding remarks concerning the works reported in Chapters 2 and 3, and future perspectives of this thesis. It is expected that

this thesis contributes towards the development of new strategies for the characterization of metallic nanoparticles and fabrication of SERS substrates platforms.

1 GENERAL INTRODUCTION

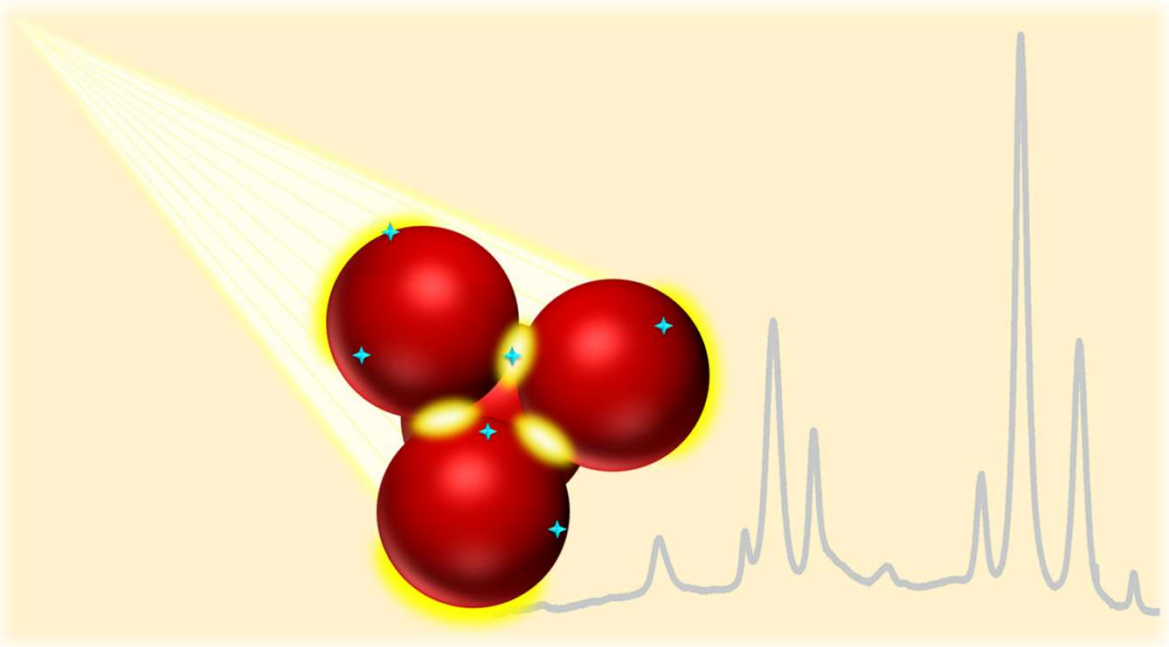

Naiara Vieira Godoy

1.1 PLASMONIC NANOPARTICLES

The use of metallic nanoparticles (MNPs) to give rise to colored glasses is an ancient strategy of the glass industry. The most famous colored glass artifact containing metallic nanoparticles is the Lycurgus cup, a Roman vessel dated to the 4th century AD (Figure 1.1a). The Lycurgus cup was first reported in 1845, and it gained attention due to its unusual optical properties, presenting two different colors depending on the lighting orientation: a greenish color when illuminated from outside and a reddish color when illuminated from the inside (Figure 1.1a). Since the 1950s, studies were carried out to determine the colorant of the glass and, in the 1960s, the dichroic effect was attributed to the presence of silver and gold submicroscopic crystals or colloids of the metals.[1] Nonetheless, only with the development of modern transmission electronic microscopy (TEM) in the 1980s, the presence of 50–100 nm silver-gold alloy nanoparticles was confirmed (Figure 1.1b).[2]

Before the report of the Lycurgus cup, the German chemist Johann Kunckels make the first mention to the gold nanoparticles, which should be present in colloidal gold sols used in the medicine in the 16th century.[3] Nonetheless, the investigation of the light interaction with gold nanoparticles was first reported by Michael Faraday in 1857.[4] After testing some synthesis conditions, Faraday synthesized gold nanoparticles by reducing a $NaAuCl_4$ aqueous solution with phosphorus in carbon disulfide. He reported the immediate color change of the colloid from yellow to red, which became ruby after at least six hours.

The original gold nanoparticles colloid synthesized by Faraday are still preserved in the Royal Institution in The Faraday Museum (Figure 1.1c). After the synthesis, Faraday evidenced the presence of the gold nanoparticles after observing the behavior of the light within the nanoparticle colloid:

> the particles are easily rendered evident, by gathering the rays of the sun (or a lamp) into a cone by a lens, and sending the part of the cone near the focus into the fluid; the cone becomes visible, and though the illuminated particles cannot be distinguished because of their minuteness, yet the light they reflect is golden in character, and seen to be abundant in proportion to the quantity of solid gold present (Faraday, 1857, p. 160).[4]

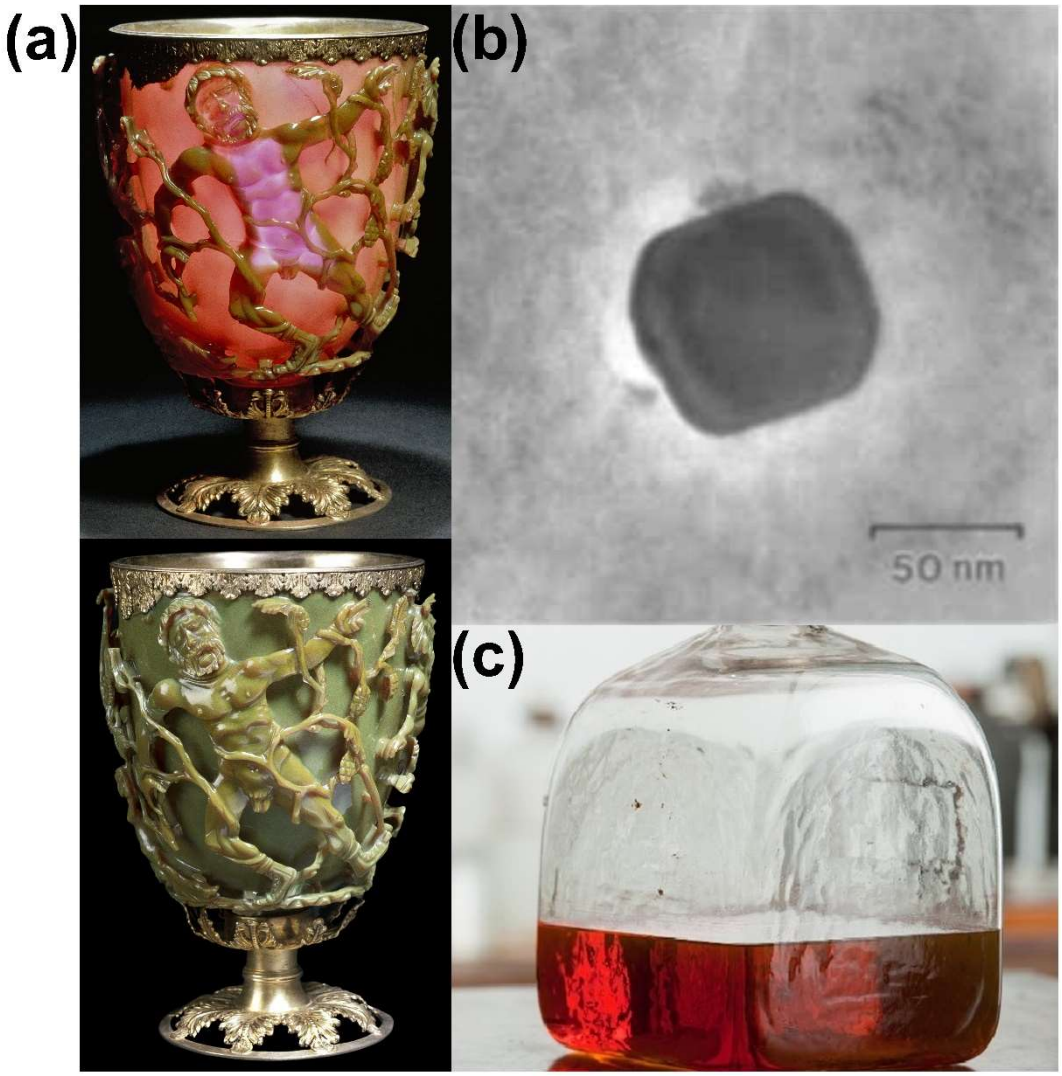

Figure 1.1. (a) Photographs of the Lycurgus cup when illuminated from the inside (above) and outside (below). © The Trustees of the British Museum. (b) TEM image of silver-gold alloy nanoparticle within the glass of the Lycurgus cup. Reprinted with permission from reference 2. Copyright 2007 John Wiley and Sons. (c) Faraday's colloidal gold nanoparticles. Credit: Paul Wilkinson (https://www.rigb.org/our-history/iconic-objects/iconic-objects-list).

Among Faraday's observations, he noticed the increase of the scattering intensity as the concentration and size of nanoparticles increase. He also reported the color difference between the reflected and transmitted light when illuminating the colloids from the front and behind, respectively.

Faraday's work revolutionized the world of science, marking the birth of the Modern Colloid Chemistry and Nanoscience. At the time, Faraday was amazed by the

optical properties of the nanoparticle colloids and, probably, he knew the importance of his work:

> the particles in these fluids are remarkable for a set of physical alterations occasioned by bodies in small quantities, which do not act chemically on the gold, or change its intrinsic nature; for through all of them it seems to remain gold in a fine state of division (Faraday, 1857, p. 165).[4]

As initially observed by Faraday, the noble MNPs present outstanding optical properties, which nowadays is attributed to the phenomenon known as localized surface plasmon resonance (LSPR). It describes the collective oscillation of free electrons of the conduction band on the metallic nanoparticle surface, which is originated from the interaction between the electron cloud and electromagnetic radiation.[5]

When the metallic nanoparticle is much smaller than the wavelength of the incident electromagnetic radiation (known as *quasi-static approximation*, where $a \ll \lambda$, and a is the radius of the nanoparticle), the electric field interacts with the conduction electrons of the metal, being considered uniform inside the nanoparticle. The electric field displaces the electron cloud from their equilibrium position (i.e., away from the positive nuclei of the metallic network), and induces an electric dipole on the nanoparticle surface. The Coulombic force between the electrons and the positive nuclei acts as a restoring force, giving rise to the collective oscillation of the electron cloud in-phase with the incident electromagnetic radiation (Figure 1.2).

The optical properties of bulk materials are characterized by its complex dielectric function ε, which is dependent on angular frequency (ω) and wavelength (λ) of the incident radiation[†]. For metals, the dielectric function is complex, and it is described as

$$\varepsilon(\omega) = \varepsilon_1(\omega) + i\varepsilon_2(\omega) \quad (1.1)$$

where $\varepsilon_1(\omega)$ and $\varepsilon_2(\omega)$ are the real and imaginary components of the dielectric function, respectively. The complex dielectric function is related to the polarity of the materials and also describes the behavior of the electromagnetic radiation within the materials.[6]

[†] ω is related to λ by $\omega = 2\pi c/\lambda$, where c is the speed of light (3.0 10^8 m s^{-1}).

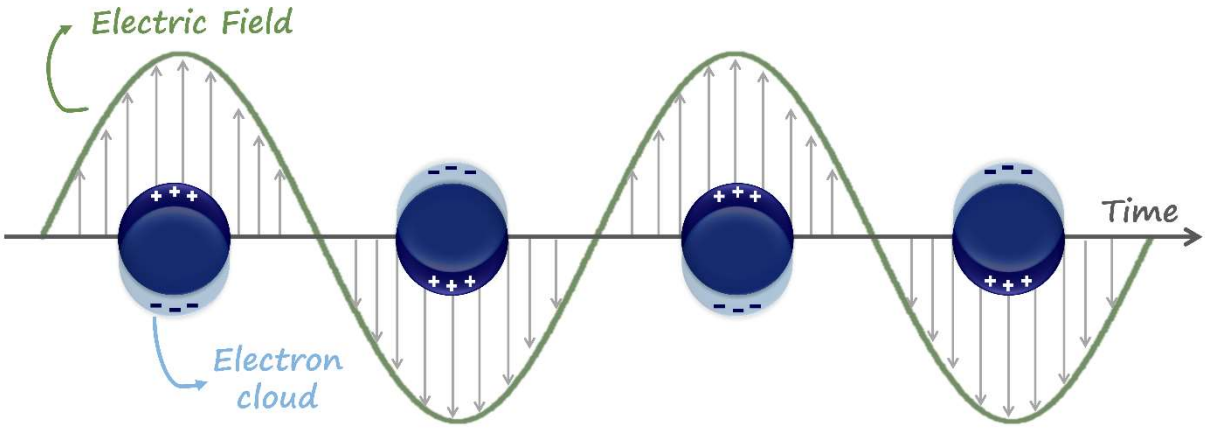

Figure 1.2. Localized surface plasmon resonance (LSPR) on a metallic nanosphere after the interaction of the incident electric field and the electron cloud.

Figure 1.3 presents the ε_1 and ε_2 of gold and silver as a function of wavelength. The high electron density of the metals leads to high negative values for ε_1 in the range of visible (VIS) to near-infrared (NIR) region of the spectrum. The similar behavior of ε_1 for both metals indicates a similar electronic density. The negative values of ε_1 are responsible for the scattering properties of gold and silver, and it explains the high efficiency of both metals in reflecting electromagnetic radiation in the VIS region.[7]

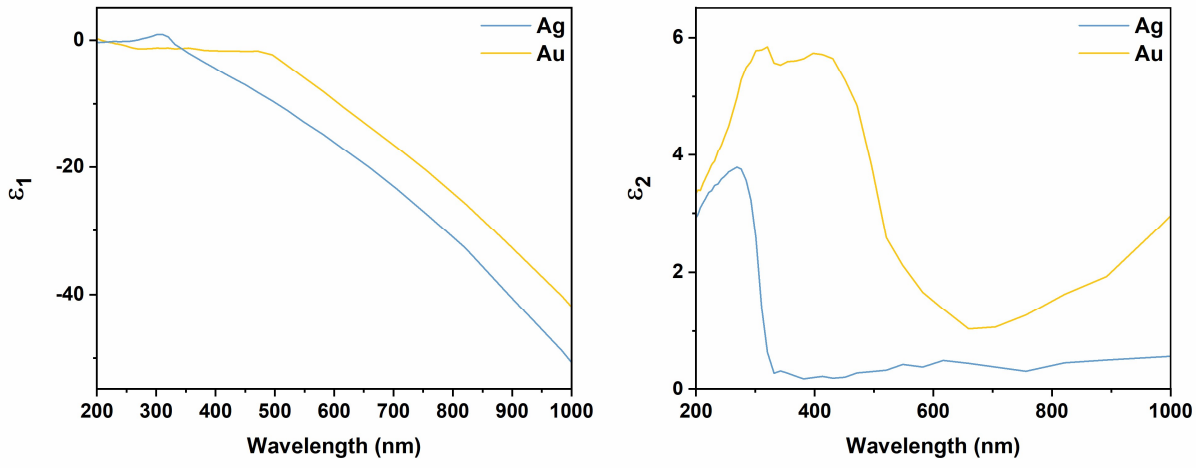

Figure 1.3. Experimental values of real (ε_1, left) and imaginary (ε_2, right) components of the dielectric function of gold and silver as a function of wavelength extracted from reference 8.

Meanwhile, ε_2 is related to absorption processes that lead to energy damping, presenting small positive values for both metals.[6] At higher wavelengths (λ

$>$ 600 nm), both metals present similar ε_2 values, indicating similar optical properties in the NIR range. However, at lower wavelengths ($\lambda <$ 600 nm), gold shows higher ε_2 values due to the interband transition band around 520 nm (2.4 eV), while the interband transition for silver relies on the ultraviolet (UV) region approx. 370 nm (3.9 eV). This explains the higher efficiency of silver in electromagnetic radiation scattering in the UV-VIS range compared with gold.[9]

The interaction of the electromagnetic radiation with MNPs was described by Gustav Mie in 1908.[10] Mie proposed an analytical solution to Maxwell's equations to describe the extinction spectra (i.e., the sum of the absorption and scattering) of spherical particles, with arbitrary radius a, much smaller than the wavelength of the incident radiation ($a \ll \lambda$). Mie's theory considers the complex dielectric function $\varepsilon(\omega)$ of the metal, the constant electric field around the nanoparticle (constrained by the condition of $a \ll \lambda$), and only dipole oscillations contribute to the extinction cross-section (σ_{ext}). In this way, σ_{ext} is described as

$$\sigma_{ext} = \frac{24\pi^2 a^3 {\varepsilon_0}^{3/2} \varepsilon_2}{\lambda[(\varepsilon_1+2\varepsilon_0)^2+{\varepsilon_2}^2]} \tag{1.2}$$

where ε_0 is the dielectric constant of the surrounding medium. If the resonance condition of positive and small ε_2 and $\varepsilon_1 = -2\varepsilon_0$ is achieved, a maximum is observed in the extinction spectrum of the nanoparticle.[6] The negative value of ε_1 allows the resonance condition, leading to the maximum polarizability of the metallic nanoparticle. Subsequently, a maximum electromagnetic radiation scattering is achieved. Since ε_1 is wavelength-dependent, it will determine the LSPR frequency of the nanoparticle, however, the dimension of the resonance and the optical response will be constrained by ε_2.[7]

Considering the quasi-static approximation used in Mie's theory and solving the LaPlace's equation for the electrostatic potential at a given distance r, the electric field outside the metallic nanosphere (E_{out}) can be obtained by Eq.(1.3) as follows[11]

$$\overrightarrow{E_{out}} = |\overrightarrow{E_0}|\hat{z} - \alpha|\overrightarrow{E_0}|\left[\frac{\hat{z}}{r^3} - \frac{3z}{r^5}(x\hat{x}+y\hat{y}+z\hat{z})\right] \tag{1.3}$$

where E_0 is the electric field of the incident electromagnetic radiation, α is the polarizability of the metallic nanoparticle, x, y, and z are the Cartesians coordinates,

and $\hat{x}$, $\hat{y}$, and $\hat{z}$ are vectors units. E_0 is represented together with the unit vector $\hat{z}$ since it is assumed to be in the z-direction. The term αE_0 is the induced dipole moment (μ_{ind}) resulted from the electron cloud polarization. Therefore, the second term corresponds to the contribution of the scattered electric field arising from the LSPR to the incident electric field at a given distance r.[12]

The strong dependency of the metallic nanoparticle's polarizability on its dielectric function and the dielectric constant of the surrounding medium is described by Eq.(1.4).[11] Considering this dependency, Eq.(1.3) is rewritten in Eq.(1.5).

$$\alpha = \left(\frac{\varepsilon(\omega) - \varepsilon_0}{\varepsilon(\omega) + 2\varepsilon_0}\right) a^3 \tag{1.4}$$

$$\overrightarrow{E_{out}} = |\overrightarrow{E_0}|\hat{z} - |\overrightarrow{E_0}|a^3 \left(\frac{\varepsilon_1(\omega) + i\varepsilon_2(\omega) - \varepsilon_0}{\varepsilon_1(\omega) + i\varepsilon_2(\omega) + 2\varepsilon_0}\right)\left[\frac{\hat{x}}{r^3} - \frac{3x}{r^5}(x\hat{x} + y\hat{y} + z\hat{z})\right] \tag{1.5}$$

Eq.(1.5) evidences the electric field enhancement dependency on the properties of the MNP (ε_1 and ε_2) and the surrounding medium (ε_0). It is noticed from Eq.(1.5) that a maximum enhanced electric field outside the nanoparticle arises from the maximum electromagnetic radiation scattering achieved by the resonance condition (small positive ε_2 and $\varepsilon_1 = -2\varepsilon_0$). The enhancement of the electric field is the basis for surface-enhanced spectroscopies that relies on the intensity of the electromagnetic radiation, such as surface-enhanced Raman spectroscopy (SERS), surface-enhanced infrared absorption (SEIRA), and surface-enhanced fluorescence (SEF).

It is worth to remark that the resonance condition $\varepsilon_1 = -2\varepsilon_0$ was defined considering a nanoparticle with a spherical shape (when $a \ll \lambda$). Therefore, nanoparticles with different shapes will satisfy other specific boundary conditions, and different resonance conditions are required for each shape.[9] Since Maxwell's or LaPlace's equation can be analytically resolved only for spherical and spheroid nanoparticles, modern numerical techniques were developed to simulate the optical properties of MNPs with arbitrary shape and size within an arbitrary dielectric medium.[11]

As aforementioned, the dielectric constant of the surrounding medium plays an essential role in the enhancement of the electric field and the optical properties of the MNPs. When the LSPR of the MNPs is excited, the electric field that arises from

the induced dipole moment induces the polarization of the dielectric medium. This polarization produces a charge accumulation at the interface between the dielectric medium and the MNP, which will partially reduce the charge accumulation on the nanoparticle surface. This effect gives rise to a lowering of the restoring force of the electron cloud oscillation, leading to an LSPR with lower frequency. Therefore, the higher the dielectric constant of the medium, the higher its polarization, and a more significant effect on the LSPR is observed, resulting in a larger shift of the LSPR towards lower frequencies.[13] The red-shift effect of the LSPR by the increase of the dielectric medium is shown in Figure 1.4a.

The plasmonic properties of the MNPs are also dependent on their size. Figure 1.4b shows the extinction spectra of gold nanospheres with the diameter in the range of 8 up to 180 nm. As the nanoparticle increases, the dipole resonance shifts to lower frequencies since the increase of the distance between the charge accumulation leads to a weaker restoring force. Then, the nanoparticle size will determine the LSPR frequency. This effect also increases the induced dipole moment, leading to an increase in the electromagnetic radiation scattering. Additional effects of increasing the nanoparticle size are the broadening of the dipole resonance due to radiation losses and the appearance of higher-order LSPR as the electrostatic approximation fails.[9,13,14] The broadening of the extinction band is also a result of the size dispersion effect.

Besides the influence of the surrounding medium and size of the nanoparticles, the optical properties of the MNPs are tuned by their shape, presenting different superficial polarization patterns according to each specific morphology. The influence of the nanoparticle shape in the LSPR properties of silver and gold nanoparticles is shown in Figure 1.4c and 1.4d, respectively. Typically, anisotropic nanoparticles present the dipole resonance red-shifted regarding the dipole resonance of a sphere due to the enhanced charge separation that is induced by the sharp corners. More than one LSPR is also observed for some nanoparticles due to different polarization symmetries in the structure, besides the appearance of multipolar resonances.[15] Therefore, the polarization of each specific nanoparticle will lead to a different contribution to the local electric field in the vicinity of the nanoparticle. Anisotropic nanoparticles with sharp corners play a special role in the surface-enhanced spectroscopies since the higher charge accumulation on the tips leads to a higher electric field enhancement.

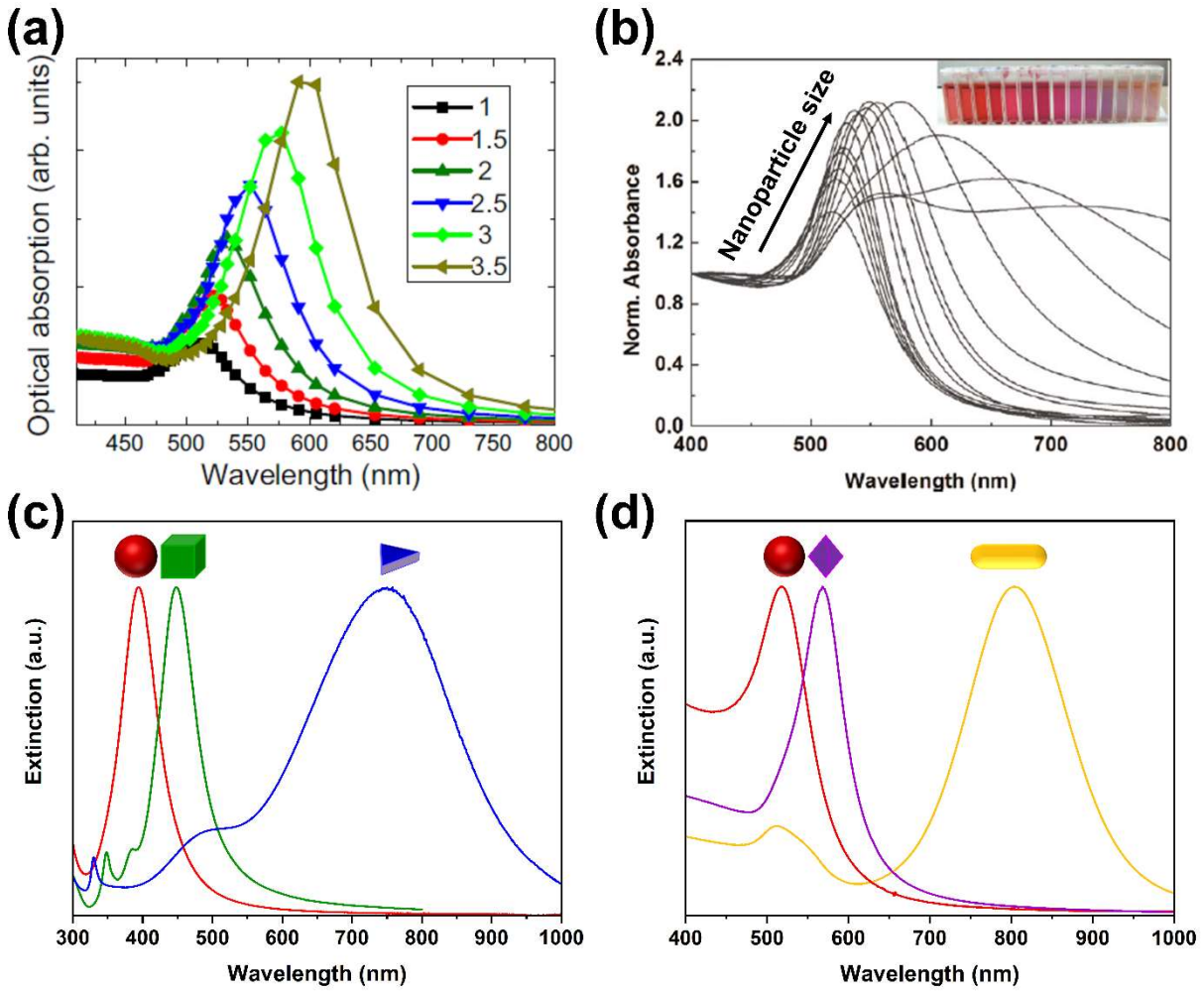

Figure 1.4. (a) Optical absorption spectra for gold nanoparticles with 10 nm size in a dielectric medium with different dielectric constant. Reprinted with permission from reference 13. Copyright 2011 IOP Publishing, Ltd. (b) Extinction spectra of gold nanospheres with varying sizes from 8 up to 180 nm. Adapted with permission from reference 16. Copyright 2011 American Chemical Society. (c) Extinction spectra of silver nanoparticles with the shapes of a sphere (red), cube (green), and prism (blue). (d) Extinction spectra of gold nanoparticles with shapes of a sphere (red), octahedron (purple), and rod (yellow).

1.2 SURFACE-ENHANCED RAMAN SPECTROSCOPY – SERS

In 1928, Raman and Krishnan[17] described "*a new type of secondary radiation*" that arises from the fluctuations of the normal optical properties of molecules or atoms. By using a telescope to converge a beam of the sunlight and a pair of radiation filters, they observed the difference between the incident and scattered radiation for sixty different liquids. It was observed a "*modified scattered radiation*" with

a different wavelength from the incident radiation, in addition to the scattered radiation with the same wavelength as the incident radiation. Although Landsberg and Mandelstam[18] simultaneously described the phenomenon, and Smekal[19] theoretically predicted it, the effect was named after the Indian physicist Chandrasekhara Venkata Raman. Raman was awarded the Nobel Prize in Physics in 1930 for his discovery of the *Raman effect*.[20,21]

After the discovery of the Raman effect, the development of the Raman spectroscopy was stimulated, and, until nowadays, it is widely used as a characterization tool for different types of systems, providing compositional and structural information.[22–25] The *Raman Spectroscopy* is a vibrational spectroscopic technique based on the inelastic scattering of the electromagnetic radiation by the matter, where an energy transfer between the incident radiation and the matter leads to scattered radiation with a different energy. The technique is an outstanding tool for molecular characterization since it provides specific vibrational information that acts as a molecular fingerprint. Furthermore, the technique has several advantages such as the low (or non) consume solvents, minimal (or non) sample preparation, simple measurement acquisition, and non-destructive analysis. Although these several advantages make the Raman spectroscopy a highlighted analytical tool for qualitative purposes, its use as a quantitative tool for trace-level analysis is limited by its low sensitivity, which is resulted from the *intrinsic low-intensity* of the Raman scattering.[12]

The *Surface-enhanced Raman Spectroscopy (SERS)* emerges to overcome the low-intensity limitation of the Raman spectroscopy. It is based on the enhancement of the Raman scattering of molecules adsorbed or near to rough metal surfaces or metal nanoparticles. The SERS technique is widely used as an analytical tool for qualitative and quantitative purposes. Its outstanding application relies on the main advantage of high sensitivity offered by the technique in addition to the advantages of conventional Raman spectroscopy. The high sensitivity of the technique allows the achievement of ultralow detection limits (LOD) in the order of 10^{-9} mol L^{-1} or even as low as 10^{-20} mol L^{-1}.[26,27]

The SERS effect was first observed in 1974 by Fleischmann et al.[28] during the study of Raman scattering of pyridine adsorbed on a rough silver electrode. At the time, the enhanced Raman scattering of the molecules was attributed to a surface-area effect. In 1977, Jeanmaire and Van Duyne[29] and Albrecht and Creighton[30]

simultaneously studied the enhancement of the Rama spectra of adsorbed pyridine at a silver electrode. Both works suggested an enhancement of approx. 10^5–10^6 of the Raman spectra of the molecule. In the paper, Jeanmaire and Van Duyne explained the enhancement of the Raman spectra of pyridine and other molecules due to "*a resonance Raman enhancement effect due to the coupling of the scattering process with an electronic transition in the adsorbed molecule*" and an "*electric field enhancement of the Raman scattering cross section*".[29] Meanwhile, Albrecht and Creighton attributed the phenom to "*a surface effect which greatly increases the molecular Raman scattering cross sections*".[30] Albrecht and Creighton also connected their results to the resonant Raman effect‡ involving the coupling of the molecule through the surface plasmon modes as proposed by Philpott in 1975.[31] Then, in 1978, Moskovits[32] explained the SERS intensities by plasmon resonances of metal nanostructures at resonance and preresonance conditions. Also, Moskovits predicts the SERS enhancement for silver, gold, and copper nanostructures.

The ideas concerning the Raman scattering enhancement that arose from an electronic transition of the absorbed molecule due to the metal surface and the enhancement of the electric field gave rise to the known *chemical* and *electromagnetic enhancement mechanisms*, respectively.[33] The Raman and SERS effects will be discussed in the following sections. Complete overviews of the principles and applications of SERS and Raman effects are described in several books and reviews.[5,7,9,12,20,34–36]

1.2.1 Raman Effect

When electromagnetic radiation interacts with a molecule, it gives rise to the distortion of the molecule's electron cloud (i.e., it changes its electronic density distribution) and induces the electron oscillation at the same frequency of the incident radiation. The distortion of the electron cloud causes a dipole moment on the molecule and its oscillation leads to the emission of electromagnetic radiation in all directions. This phenomenon is known as *scattering*. When the scattering process occurs without changing the photon energy (elastic scattering), it is called the *Rayleigh scattering*.

‡ Raman resonant effect: transition between two electronic states of the molecule induced by an excitation wavelength with energy close to the transition energy.

Meanwhile, if an energy transfer between the incident radiation and the molecule occurs and the photon energy is changed (inelastic scattering), it is called the *Raman scattering*.[7,34,36]

The energy difference between the scattered and incident photon observed for the Raman scattering process may be a result of molecular vibrations. Figure 1.5 shows a simplified energy diagram that illustrates the Raman and Rayleigh scattering processes at molecular quantum states. For all the scattering processes, the vibrational transition occurs through an intermediate higher-energy level that corresponds to the perturbed state of the molecule (i.e., the distortion of the molecule's electron cloud), known as the *virtual state*.[7] In the Rayleigh scattering, the process does not change the vibrational state of the molecule since the scattered photon has the same energy as the incident photon ($h\nu_i$)[§]. Meanwhile, in the Raman scattering, the final vibrational state of the molecule is different from its initial vibrational state.

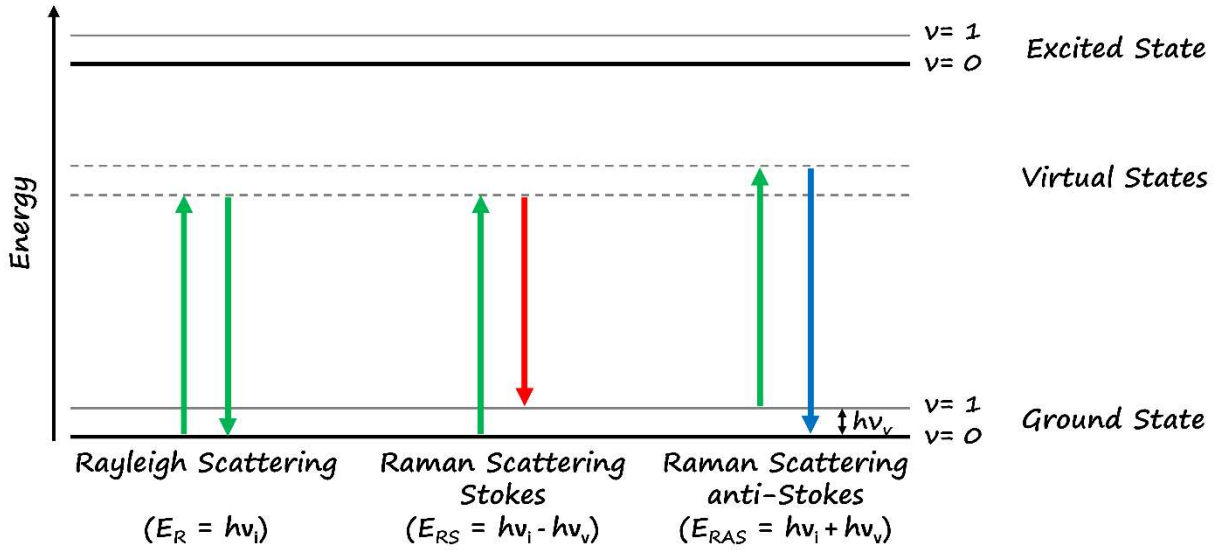

Figure 1.5. Representation of the Rayleigh and Raman scattering processes in a simplified energy diagram. Green arrows indicate the energy of the incident ($h\nu_i$) and Rayleigh scattered (E_R) photons. Red and blue arrows indicate the energy of Stokes (E_{RS}) and anti-Stokes (E_{RAS}) Raman scattered photons, respectively. $h\nu_v$ represents the energy of the molecular vibrational transition.

[§] Energy (E) and frequency (ν) of a photon are related by: $E=h\nu$, where h is the Planck's constant ($6.626\ 10^{-34}$ J.s).

As can be observed in Figure 1.5, the Raman scattering can result in two types of vibrational transitions: Stokes and anti-Stokes processes. When the molecule is excited from the ground state into a higher vibrational state, it is called the Stokes process. In this case, the scattered photon has lower energy than the incident photon. On the contrary, when the molecule is relaxed from an excited vibrational state to the ground state, it is called the anti-Stokes process. For the latter, the scattered photon has higher energy than the incident photon. Note that the energy difference between the scattered and incident radiation for both Raman scattering processes corresponds to the vibrational frequency of a specific molecular vibrational transition ($h\nu_v$) (Figure 1.5). This characteristic establishes the vibrational fingerprint of a specific molecule in a Raman scattering spectrum, where each band corresponds to a specific molecular vibrational transition.[12]

The intensity of the scattered radiation depends on the dipole moment induced by the electron cloud distortion of the molecule which, in turn, is dependent on the electric field of the incoming radiation and the molecular polarizability, described in terms of *Raman polarizability tensor*. The Raman polarizability tensor is a response function that represents the volume and shape of the molecular electronic cloud, being associated with the facility for the electron cloud distortion.[12,34] This implies that a fluctuation (i.e., a change) in the polarizability with vibrational motion is required for the Raman scattering to occur. This statement is a selection rule for Raman scattering.[7]

The intensity of the Raman scattering (I_{Raman}) averaged over all the molecular orientations can be described by the Raman cross-section (σ_{RS}) and the incident photon flux (I_0) according to Eq. 1.6.[34] The Raman cross-section describes the effective area of a homogeneous incoming beam from which the molecule will scatter every photon by Raman scattering processes.[7] Typically, the Raman cross-section has low magnitude (approx. in the order of 10^{-29} cm^2)[34] that reflects the low efficiency of the Raman scattering and the subsequent intrinsic low-intensity of the phenomenon.

$$I_{Raman} = \sigma_{RS} I_0 \tag{1.6}$$

1.2.2 SERS Effect

As aforementioned, the SERS enhancement arises from the chemical (CE) and electromagnetic (EM) enhancement mechanisms. The CE mechanism arises from the modification of the Raman polarizability tensor of the molecule that is absorbed (adsorbate) onto the metallic nanostructure surface. The change of the Raman polarizability of the molecule can occur regardless of the formation of a metal-adsorbate complex. However, the most studied description of the mechanism requires the formation of the metal-adsorbate complex by a new chemical bond, known as the *charge-transfer mechanism* (Figure 1.6a).[7,37]

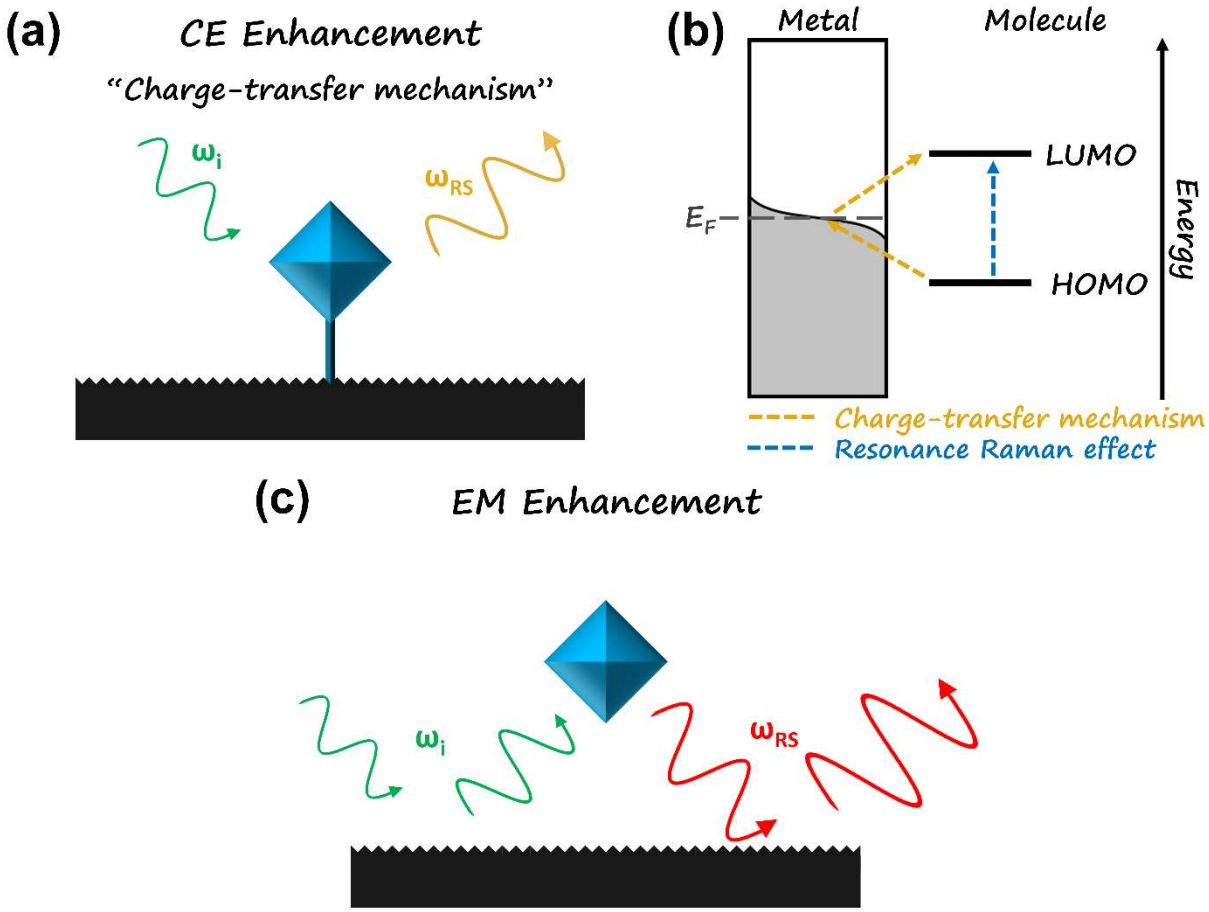

Figure 1.6. Representation of the (a) chemical (CE) and (c) electromagnetic (EM) enhancement mechanisms for SERS. (b) Representation of the photoinduced electronic transitions in the metal-adsorbate complex. In (a) and (b), ω_i and ω_{RS} are respectively the excitation and Raman scattering angular frequencies, and the blue square represents the molecule.

The mechanism consists of the photoinduced charge-transfer between the metal states close to the Fermi level (E_F) and the molecular energy levels (HOMO[**] or LUMO[††]), as shown in Figure 1.6b. However, it may occur only if the excitation energy matches the energy difference between the molecular energy levels and the E_F of the metal. Once the condition of the energy difference is achieved, the transition from the molecule to the metal (HOMO→ unoccupied states above E_F) or from the metal to the molecule (occupied states slightly below E_F → LUMO) can be triggered (Figure 1.6b).

When the exciting energy is close to the energy difference between the molecular energy levels, the HOMO–LUMO transition may be directly excited. It is known as the Raman resonance effect (Figure 1.6b). If the excitation of the HOMO–LUMO transition occurs in resonance with the LSPR excitation, it leads to a further enhancement of the Raman scattering of the molecule, known as surface-enhanced resonance Raman scattering (SERRS).[7]

Whereas the CE enhancement relies on the analyte properties, the EM enhancement results from the plasmonic properties of the metallic nanostructures. Another difference is that the EM mechanism does not require the formation of the metal-adsorbate complex. The coupling of the metallic nanostructure's LSPR and the incident electromagnetic radiation (ω_i)[‡‡] enhances the electric field in its vicinity. Then, the molecule adsorbed or near the nanostructure surface experiences this stronger electric field that excites its Raman modes, giving rise to an enhanced Raman scattering.[12] The emitted Raman scattering from the molecule (ω_{RS}) is further enhanced by the same effect, providing a second contribution to the SERS enhancement (Figure 1.6b).[37]

In this way, both "exciting" and "emitting" electric field contributes to the SERS enhancement. Considering that the excitation wavelength frequency ω_i is close to the Raman scattering frequency ω_{RS} (only shifted by a vibrational quantum $h\nu_v$) (Figure 1.5), the electric field enhancement for both emitted Raman scattering and exciting electromagnetic radiation are similar. Thus, the overall enhancement factor (EF) will be proportional to approx. $|E_{out}(r)|^4/|E_0(r)|^4$, known as E^4-approximation.[9,12] It is widely accepted that the EM mechanism is the main contribution to the SERS

[**] HOMO means highest occupied molecular orbital.
[††] LUMO means lowest unoccupied molecular orbital.
[‡‡] ω is related to ν by: $\omega=2\pi\nu$.

effect, achieving EF in the order of 10^4–10^8 in contrast to EF of 10–10^6 for the CE mechanism.[37,38]

1.3 SERS SUBSTRATES

As described in the previous section, the enhancement of the Raman scattering mainly relies on the electric field enhancement (i.e., the EM enhancement mechanism) being strongly dependent on the SERS enhancing capabilities of the substrate. Therefore, the magnitude of the enhanced electric field depends on the plasmonic properties of the MNPs that, in turn, are influenced by their size, morphology, composition, and arrangement.

Concerning the composition, gold and silver are the most used metals for the fabrication of SERS substrates since they exhibit higher scattering efficiency in the VIS-NIR range than other metals, such as palladium and platinum, due to the lower non-radiative decay.[7] Another advantage of gold and silver nanoparticles is that their LSPR is easily tunable in the VIS-NIR range by changing their size and morphology (Figure 1.4). These characteristics of gold and silver nanoparticles are interesting since the laser lines available for Raman spectrometers commonly have wavelengths in the VIS-NIR range.[39] However, gold is often preferable for the fabrication of SERS substrates than silver due to its higher chemical stability.

Among the several morphologies, nanospheres are the simplest and easiest to synthesize, being one of the most used in the fabrication of SERS substrates.[40–43] On the other hand, anisotropic nanoparticles such as rod,[38] stars,[44] cube,[45] and octahedra[46] gained attention for SERS sensing due to the high electric field enhancement that arises from the high charge accumulation on their tips. Regardless of the morphology, the synthesis of MNPs is a fundamental step to obtain SERS substrates with excellent performance since a heterogeneous morphology and/or size may lead to poor optical properties. In this sense, several studies report synthetic routes to obtain shape- and size-controlled plasmonic nanoparticles that can be used to improve the SERS properties of the substrates.[14,16,47–50]

Besides the control of the shape and size of the nanoparticles, their arrangement in the SERS substrates must be considered since it influences the formation of nanoparticle aggregates and the subsequent optical properties of the

SERS substrate. Nanoparticles aggregates play a critical role in the SERS performance when they lead to the formation of hot spot regions. The hot spot is characterized by a subwavelength distance between the MNPs that induces the plasmon coupling of the neighboring nanoparticles. Then, the plasmon coupling results in the highest EF of the electric field in this region.[51] In this way, once a molecule is adsorbed on a hot spot, it will result in a Raman scattering more intense than in the SERS condition at one nanoparticle (or outside the hot spot region), being more significant than in the normal Raman condition as well (Figure 1.7a).

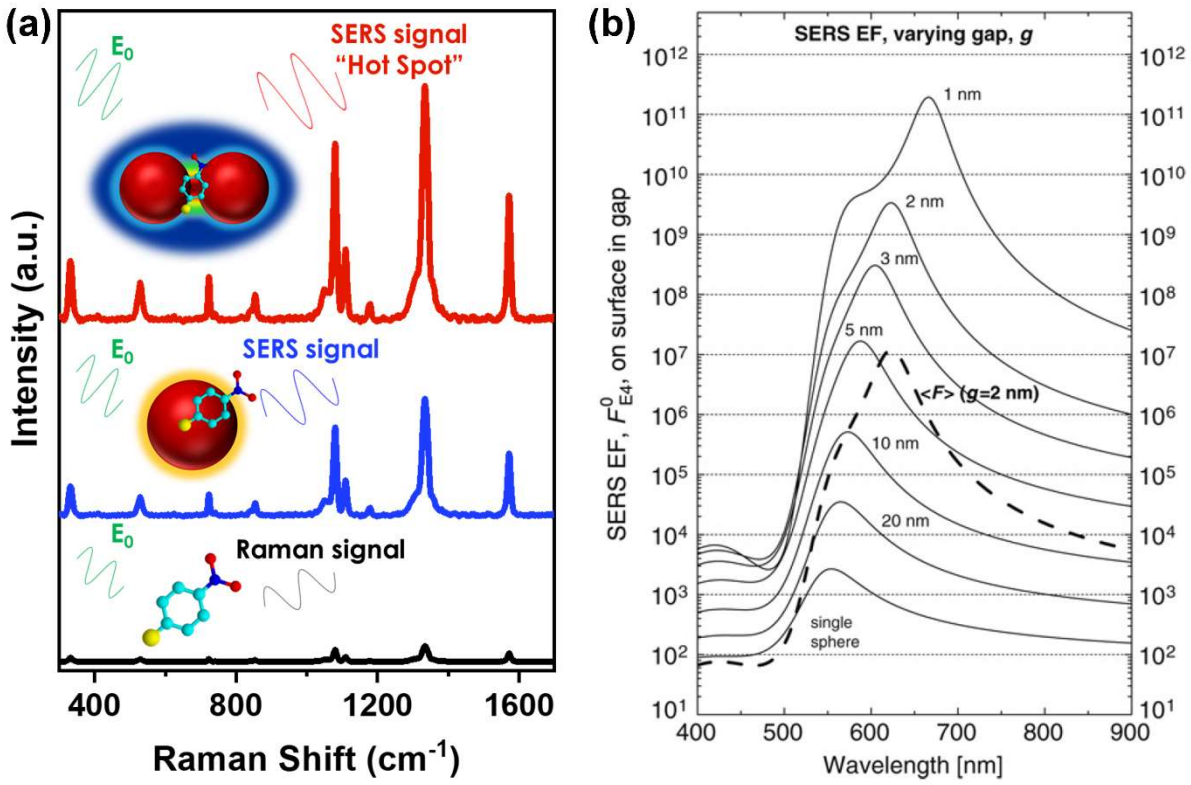

Figure 1.7. (a) Representation of the Raman scattering of an analyte under normal Raman, SERS, and hot spot conditions. (b) Maximum SERS EF (F^0_{E4}) (solid line) at the hot spot of a dimer of gold nanospheres (a = 25 nm) in water for different gap distances (g), and average SERS EF (<F>) for g= 2 nm (dashed line). The incident wave is polarized along the dimer axis. Reprinted with permission from reference 7. Copyright 2009 Elsevier.

The magnitude of the SERS enhancement at the hot spot is extremely sensitive to the gap distance (interparticle distance). Figure 1.7b shows the variation of the SERS EF for different gap distances between two identical gold nanospheres (a = 25 nm). As the gap distance of a nanoparticle dimer decreases, the plasmon

coupling becomes stronger, and the SERS enhancement increases.[7,52] It is noticed that the maximum SERS EF red-shifts as the gap distance decreases. It follows the lowering of the LSPR energy as the strength of the plasmon coupling increases.[7] Moreover, the lower magnitude of the average SERS EF (<F>) for g= 2 nm compared to the maximum SERS EF (Figure 1.7b) reflects the spatial distribution of EF over the hot spot that will be discussed later.

Assemblies of MNPs with more than two nanoparticles, such as three-dimensional hot spots nanostructures[53] and linear arrays[54], can lead to further considerable SERS enhancement. However, the increase of the nanoparticle array length does not always result in a further increase in the SERS enhancement. A decrease of the SERS enhancement can be observed when arrays of larger MNPs increases, where radiation losses arise.[52,54] The number of nanoparticles in the aggregates also influences their LSPR position. For instance, the rise in the nanoparticle number in a linear array decreases the energy of the LSPR.[55] Besides, the LSPR position of dimers and nanoparticle arrays is also red-shifted LSPR as the MNP size increases as well as observed for single MNPs (Figure 1.4b).[54]

Due to their remarkable enhancing properties, a high density of hot spots is required for obtaining substrates with high SERS performance. Several techniques are available for the fabrication of SERS substrates that can be divided into the main categories of MNPs in colloidal suspension, nanostructures fabricated directly on solid substrates, and MNPs immobilized on solid substrates. Aspects and examples of the fabrication of these three categories of SERS substrates are described in a comprehensive review.[56] Regardless of the chosen method, all the fabrication procedures have parameters that should be carefully evaluated and optimized, mainly regarding the nanoparticle aggregation. For instance, one parameter that should be evaluated is the MNP colloid concentration, since it can be useful to optimize sampling steps during the fabrication of the SERS substrate, such as surface coverage of solid surfaces or even to optimize the MNP colloid concentration for SERS measurements in MNPs suspensions.

Regarding the surface coverage optimization of MNPs immobilized on solid substrates, Solís et al.[57] demonstrated computational analysis of the SERS enhancement dependence on both the shape of gold nanoparticles and the surface coverage of a substrate, as shown in Figure 1.8a. For this, random monolayers of gold

nanoparticles with the shapes of nanospheres, nanorods, and nanostars were evaluated. Moreover, excitation wavelengths at 785, 633, and 900 nm were chosen for the calculations to achieve optimum SERS performance of nanorods, nanospheres, and nanostars, respectively.

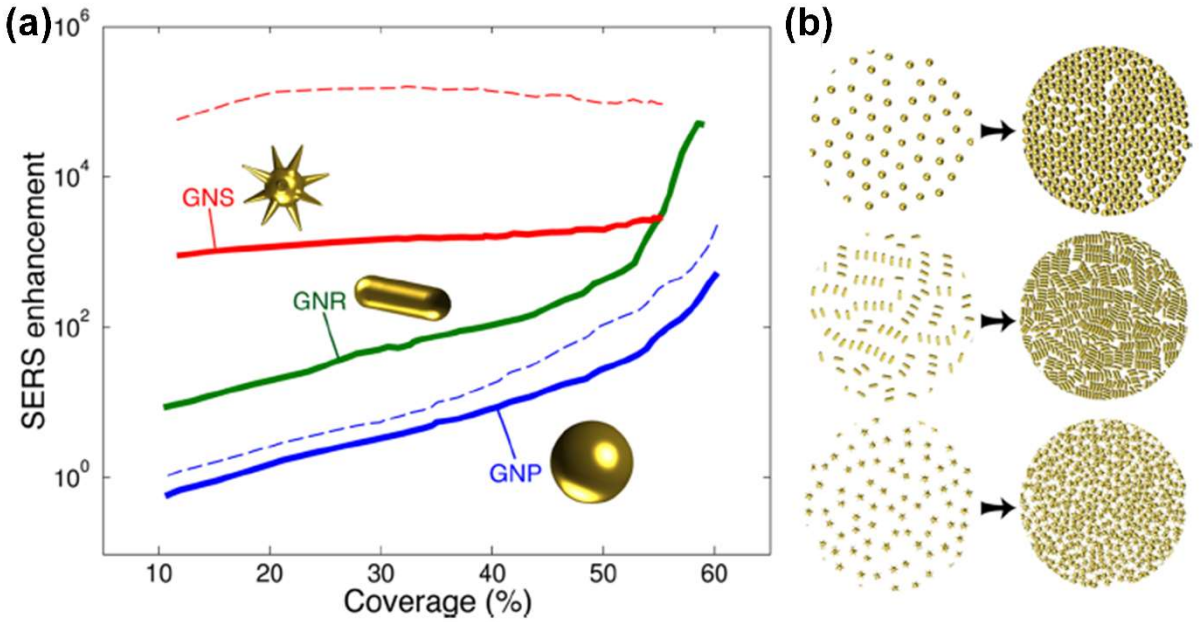

Figure 1.8. (a) Dependence of the SERS enhancement on the surface coverage of a SERS substrate for monolayers of gold nanoparticles with different shapes. Solid curves are calculated for the excitation wavelength at 785 nm (resonant with nanorods), and dashed curves are calculated for excitation wavelength at 633 nm (resonant with nanosphere) and 900 nm (resonant with nanostar) for nanospheres and nanostars, respectively. Note that the SERS enhancement scale is logarithmic. (b) Scheme of the surface coverage increase from low- to high-density of nanoparticles. Reprinted with permission from reference 57 (https://pubs.acs.org/doi/full/10.1021/acsphotonics.6b00786). Copyright © 2016 American Chemical Society. Note: further permissions related to the material excerpted should be directed to the ACS.

Firstly, the analysis of the single nanoparticles shows that the nanosphere presents the lowest SERS enhancement. In contrast, the nanorod shows an intermediate response, and the nanostar exhibits the highest enhancement due to the presence of sharp tips, as expected. This behavior reflects on the SERS enhancement of the substrates with low-density nanoparticles as observed for surface coverage of

approx. 10 % (Figure 1.8a), when the optical properties of the substrate arise from nanoparticles highly dispersed (Figure 1.8b).

When the density of nanoparticles increases and the hot spots arise (Figure 1.8b), the SERS enhancement rapidly increases for nanospheres and nanorods up to surface coverage of approx. 60 % (Figure 1.8a). For the nanosphere, this behavior is observed whether or not the excitation wavelength is resonant with the optimum SERS performance of the nanoparticle. Meanwhile, the nanostar shows only a slight improvement in its performance as the density of nanoparticles increases. It occurs independently if the excitation wavelength is resonant with the optimum SERS performance of the nanoparticle or not (Figure 1.8a). This behavior can be explained by the conformations of nanostar aggregates, where the nanostars are often intertwined with valley-to-tip contacts. This type of conformation does not give rise to hotter hot spots or can even damp the electric field enhancement from the single particles.[57] The latter is probably one of the causes of the decrease of SERS enhancement above approx. 30 % of surface coverage when using the excitation wavelength at 900 nm (Figure 1.8a).

These results are quite impressive since they demonstrate that different strategies for the fabrication of SERS platforms can be established depending on the nanoparticle morphology, substrate, and excitation wavelength that will be used. The optimization of the surface coverage of the substrate by increasing the nanoparticle density is an excellent path to follow, although it does not give rise to the same result for all of the cases. However, it is worth to remark that the increase of the EF with the size of the nanoparticle assembly occurs up to a threshold. From this, a hot spot deactivation may take place as the electromagnetic field is delocalized over a large assembly of nanoparticles.[41] Additionally, it was already shown that the highest enhancement of the electromagnetic field occurs at the nanoparticles in the border of a large monolayer assembly of nanoparticles.[58]

Furthermore, as pointed out by the SERS performance of the nanostars in Figure 1.8a, nanoparticle aggregates do not always lead to enhancement of SERS properties as expected. Likewise, Lee et al.[59] demonstrated that the SERS performance of assemblies of gold nanorods depends on the nanoparticle orientation. The study was carried out for gold nanorod assemblies in colloidal suspension. The results showed a decrease in the SERS intensity as the nanoparticles align according

to the side-by-side orientation. In contrast, the end-to-end alignment of nanorods induces an enhancement of the SERS performance.[52] The authors attributed the poor SERS properties of the side-by-side assembly due to the decrease in the electric field that arises from the destructive interference between the plasmon modes of the adjacent nanoparticles.

In summary, the SERS enhancement by hot spots may be affected by several factors, such as irregular architectures of aggregates (which also include heterogeneous nanoparticles), irregular gap distances, nanoparticle orientation, and the number of nanoparticles in the assembly. Up to this point, it should be noted that all the factors that influence the plasmonic properties of the substrate will affect the reproducibility of the SERS enhancement as a consequence. Needless to say, the fine control over the several factors concerning the nanoparticle aggregation to achieve reproducible SERS enhancement is still a highly difficult task to accomplish.

The reproducibility issue of the SERS substrates is still hindered by the *intrinsic spatial distribution* of the electric field enhancement around the hot spot. Figure 1.9 illustrates the spatial distribution of the EF around the hot spot between two gold nanospheres with a gap distance of 2 nm. As it moves away from the hot spot center, the EF decreases rapidly by orders of magnitude just a few nanometers away from the hot spot.

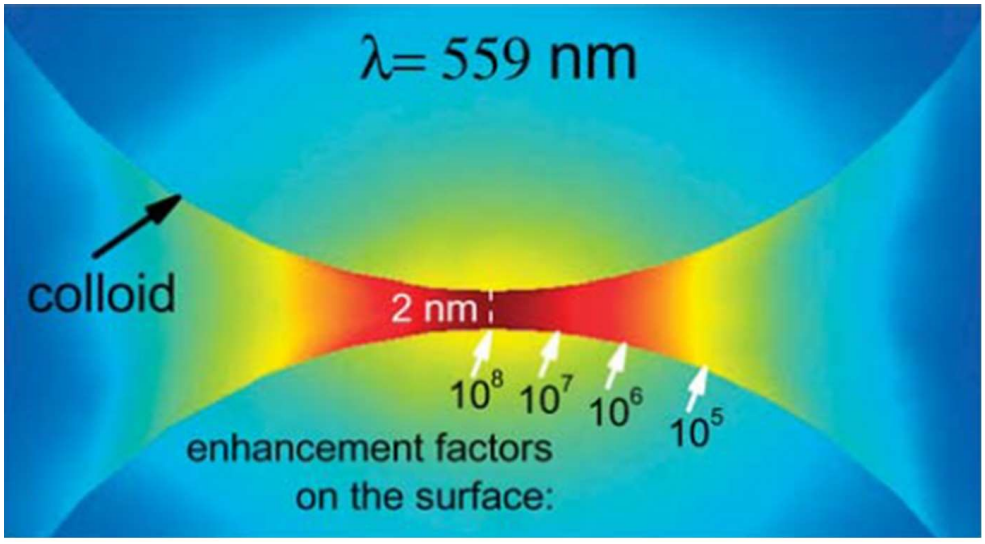

Figure 1.9. Calculated enhancement factor in the nanogap of 2 nm between two gold nanospheres (a = 30 nm) according to the E^4- and electrostatic approximations, with λ= 559 nm. Adapted with permission from reference 51. Copyright 2008 Royal Society of Chemistry.

The spatial distribution of EF plays a key role in the SERS properties of a substrate since hot spot areas with the highest EFs are smaller than the total surface area of a substrate (approx. only 1 % or less of a substrate area contains hot spots).[51] Along with this, it is estimated that less than 1 % of the molecules are adsorbed on very effective hot spots (*hotter* hot spots), giving rise to approx. 70 % of the overall SERS intensity. Meanwhile, 61 % of the molecules are adsorbed on less efficient hot spots (*colder* hot spots) that contribute to only 4 % of the overall SERS intensity. [60] It reflects on the smaller magnitude of the average SERS EF compared to the maximum SERS EF at the hot spot (Figure 1.7b).

The low probability of the molecules to be adsorbed at hotter hot spots together with the spatial distribution of the EF over the hot spot region (Figure 1.9) results in an *intrinsic* SERS intensity fluctuation. This behavior is particularly important at the single-molecule SERS regime (SM-SERS regime), where the lower surface coverage of the substrate by the molecules is an additional factor that leads to a more pronounced SERS intensity fluctuation. These factors are the main causes of the long-tail distribution of SERS intensity observed for the SM-SERS regime, which is characterized by a large number of SERS spectra with low intensity and a pronounced decrease to a small number of SERS spectra with high intensity.[51,61]

The resulting SERS intensity fluctuation, mainly for the SM-SERS regime, is one of the main challenges to overcome in the field of SERS-based sensors. Besides the issues of the fabrication steps to obtaining a homogeneous distribution of reproducible hot spots over the substrate area, the sampling and data processing procedures also are a challenging task to accomplish. Firstly, the high SERS intensity fluctuation demands the performance of spatial mapping to increase the sample size, allowing the analysis of a greater part of the substrate or even all of its area.[20,46,62,63] Although it demands a long analysis time, the SERS mapping tool leads to more meaningful statistical data since the spectral information is extracted from all the mapped area. Secondly, the data processing of SERS measurements is still a developing field. Statistical tools have been used together with the SERS imaging tools to improve the data processing step and achieve more accurate results.[64–66]

The most common method to evaluate the SERS data to determine the detection and quantification limits is calculating the average and standard deviation SERS signal for each analyte concentration. Although this method is a conventional

methodology for the analytical applications in general, and it is defined by the International Union of Pure and Applied Chemistry[67] (IUPAC), it leads to a misinterpretation of the SERS phenomenon. Average signals equal or close to zero are commonly obtained due to the small number of SERS events regardless of their intensity. Thus, it leads to a misunderstanding of the absence of the analyte and low sensitivity of the sensor. Nevertheless, the rarity of the SERS events as the analyte concentration decreases is an *intrinsic property* of the stochastic characteristic of the SERS phenomenon at low concentrations, mainly at the SM-SERS regime.

Therefore, to consider the randomness of the SERS phenomenon that relies on the probabilities of the molecules being adsorbed on an effective hot spot, Brolo and collaborators[68] proposed a new protocol to process the SERS data called as *Digital Protocol*. The method consists of analyzing the relationship between the analyte solution concentration with the number of SERS events at the SM-SERS regime by considering that each SERS event is derived from a single molecule adsorbed on a hot spot. The digital protocol was successfully employed for the analysis of the emerging contaminant of aquatic environments enrofloxacin at the SM-SERS regime. A quantification limit (LOQ) of 2.8 pmol L^{-1} was estimated for the analyte using the digital protocol, while the estimation of the analyte concentration lost linearity for concentrations below 70 nmol L^{-1} using average values.

Since it considers the intrinsic properties of the SERS phenomenon, the digital protocol demonstrated to be more interesting and effective than the conventional method for the analysis of ultralow concentrations at the SM-SERS regime. The new methodology opens up the way to the improvement and development of new strategies for the evaluation of the SERS response of SERS-based sensors at low concentrations, including for systems outside the SM-SERS regime.

2 CHARACTERIZATION OF METALLIC NANOPARTICLES BY MICROWAVE-ASSISTED DECOMPOSITION PLATFORM AND AND PLASMA-BASED SPECTROMETRIC TECHNIQUES (ICP-MS AND ICP OES)

The content of this chapter is an adaptation of the article entitled “Evaluating the total gold concentration in metallic nanoparticles with a high content of organic matter through microwave-assisted decomposition platform and plasma-based spectrometric techniques (ICP-MS and ICP OES)” by N.V. Godoy, R.M. Galazzi, K. Chacón-Madrid, M.A.Z. Arruda, I.O. Mazali, reference 69.

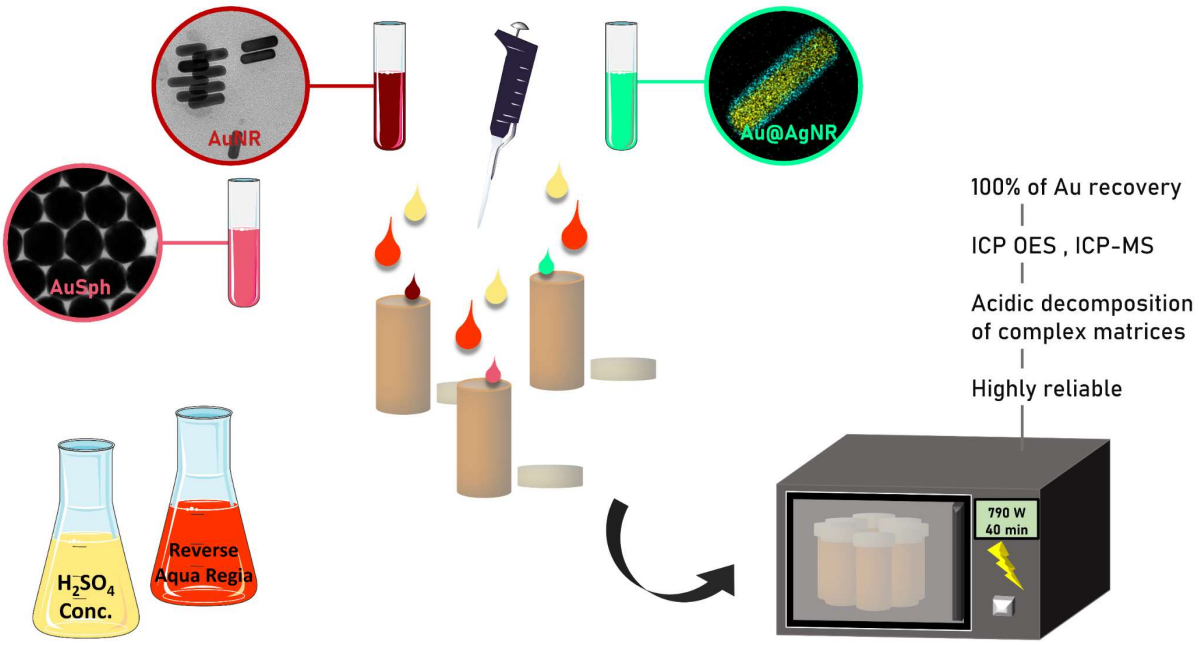

Naiara Vieira Godoy

2.1 INTRODUCTION

The unique properties of the metallic nanoparticles (MNPs), such as the large surface-to-volume ratio, high surface energy, and photonic properties, have been stimulated their study on a wide range of applications, such as biosensors, electronics, nanomedicine, catalysis, and surface-enhanced Raman spectroscopy (SERS). Besides the researches on the applications of MNPs, many studies investigate new synthetic routes for the obtainment of the desired type of MNPs,[43,70–72] while others focus on obtaining new structures of MNPs, for example, core-shell nanostructures[49,73,74] and alloy nanoparticles.[47,75]

Regardless of the goal, the characterization of the MNPs is a fundamental step covering mainly the morphological, nanoparticle size, compositional, and crystalline phase characterization. In this context, several techniques with different advantages and limitations are available, such as UV-VIS spectroscopy, dynamic light scattering (DLS), transmission electron microscopy (TEM), scanning electron microscopy (SEM), energy dispersive spectroscopy (EDS), atomic force microscopy (AFM), electron energy-loss spectroscopy (EELS), X-ray photoelectron spectroscopy (XPS), X-ray absorption spectroscopy (XAS) and powder X-ray diffraction (XRD).

The characterization of the MNPS based on the metal concentration may be interesting for the evaluation of some features of the MNPs, for example, synthesis yield, separation and sampling steps, and stability over storage time. Concerning the synthesis yield, the characterization of the metal concentration is especially interesting for multi-elemental nanostructures, being possible to evaluate the relative concentration of different metals in the nanoparticles and investigate their structural evolution during the synthesis. The metal quantification of MNPs has been used with different kinds of purposes, such as the monitoring of MNPs in the environment,[76] food,[77] biological media,[78] and toxicological analysis.[79] However, studies focusing on the metal quantification as a tool for the characterization of MNPS has not been widely explored.

For the gold quantification, UV-VIS spectroscopy has been usually applied since it is a low-cost and simple technique in addition to its wide availability. The method commonly used is based on the correlation between the extinction (or absorbance) value in the wavelength range of 400–450 nm in the extinction UV-VIS

spectrum and the Au^0 concentration. Below 500 nm, the interband transition region for bulk gold allows obtaining a linear correlation of the increase of extinction value at this wavelength range when increasing the nanoparticle volume (i.e., the Au^0 concentration) independently of the size and morphology of the MNPs.[80–82] Scarabelli et al.[83] demonstrated a valid correlation for the gold quantification in AuNR, where 0.5 mmol L^{-1} of Au^0 concentration corresponds to an extinction value of 1.2 at 400 nm.

Although the correlation between the extinction value in the wavelength range of 400–450 nm and the gold concentration has been demonstrated to provide an accurate result for gold quantification in gold nanoparticles, this strategy presents some important limitations. For instance, Hendel et al.[84] highlighted that the method should be used carefully since some deviations up to 30 % can be reached when the influence of some parameters such as particle size, oxidation state, or surface modification is not correctly considered. Besides, the gold quantification in MNPs by UV-VIS spectroscopy presents a high limit of detection in the order of mg L^{-1},[84] which can prevent the analysis of diluted samples. Finally, the UV-VIS method is not effective for the gold quantification in systems where interferences are observed in the wavelength range of 400–450 nm, such as absorption from organic molecules or localized surface plasmon resonance (LSPR) modes derived from multi-elemental nanoparticles.

Inductively coupled plasma mass spectrometry (ICP-MS) is a highlighted technique concerning the elemental quantification of inorganic nanoparticles in general, including MNPs. The use of ICP-MS-based platforms for this purpose, such as single-particle inductively coupled plasma mass spectrometry (spICP-MS), laser ablation coupled to ICP-MS (LA-ICP-MS), and liquid chromatography (LC) coupled to ICP-MS (LC/ICP-MS) are described in a comprehensive review.[85] The reasons for the wide use of ICP-MS-based platforms include high accuracy, selectivity, multi-elemental quantification, and the ultralow detection limit (LOD) in the order of ng L^{-1}, allowing the analysis of diluted samples and low consumption of sample volume.

When using conventional ICP-MS, it is common a sample preparation step, known as pre-digestion, to eliminate the interference of the matrix, where both nanoparticles and matrix are decomposed before the quantification analysis. In general, concentrated mineral acids such as nitric, hydrochloric, and sulfuric acid are used as oxidant agents for the digestion of inorganic nanoparticles. Some

nanoparticles demand specific mixtures, *e.g.*, *aqua regia* is used for the decomposition of gold nanoparticles.[86] However, the specific composition of the mixture depends on both nanoparticle and matrix composition.

Microwave-assisted decomposition is a technique widely used for the digestion of metallic nanoparticles since closed systems offer a minimal loss of the sample and allow the decomposition to occur at higher pressures and temperatures, increasing the digestion efficiency.[87] For instance, Fabricius et al.[88] demonstrated that the microwave-assisted decomposition is the most reliable method for the digestion of silver and gold nanoparticles, among others, compared to the acidification and direct measurement methods. The authors also highlighted the necessity of evaluating the sample preparation procedure for each specific type of nanoparticle.

For the purpose of characterizing a citrate capped-AgNP colloid, Galazzi et al.[89] determined the silver concentration of silver nanoparticles (AgNP) and other silver species (derived from unreacted precursor) presented in the colloid. After the fractionation and purification of the AgNP colloid by using a centrifugation step, a microwave-assisted decomposition procedure based on a mixture of nitric acid and hydrogen peroxide was applied previously to the silver quantification by ICP-MS and ICP OES (inductively coupled plasma optical emission spectroscopy). The authors found out a low synthesis yield of 50 %, indicating that 50 % of the silver remains as free ions in the suspension. Additionally, the authors evaluated the stability of the AgNP colloid over three months of storage, and a decrease of 7 % in the silver concentration of the nanoparticles fraction was verified, indicating the oxidation of the AgNP during the storage.

In this chapter, we report a microwave-assisted decomposition platform as a characterization tool for the accurate gold quantification in MNPs colloids with complex matrices and high content of organic matter. To achieve this goal, AuNR and AuSph with a high content of CTAB, and Au@AgNR with a high content of PVP were synthesized. The optimization of the microwave-assisted decomposition procedure of the AuNR colloid is described, where different sample volume, acidic mixture, and microwave program were tested. For the evaluation of the decomposition procedure, AuNR colloid was divided into three fractions AuNR-total, AuNR-res (AuNR-resuspended), and AuNR-sup (AuNR-supernatant) by a centrifugation method. The gold quantification was performed by ICP-MS and ICP OES to evaluate the accuracy

of the proposed method. After the optimization of the microwave-assisted decomposition procedure, this technology was used for the decomposition of Au@AgNR and AuSph colloids, and the subsequent gold quantification.

2.2 EXPERIMENTAL SECTION

2.2.1 Reagents and Solutions

For the synthesis of the MNPs, hydrogen tetrachloroaurate(III) trihydrate ($HAuCl_4.3H_2O$, ≥99.9 %), cetyltrimethylammonium bromide (CTAB, ≥99 %), sodium borohydride ($NaBH_4$, ≥99.99 %), silver nitrate ($AgNO_3$, >97 %), trisodium citrate dihydrate (≥98 %), L-ascorbic acid (≥99 %) and polyvinylpyrrolidone (PVP, Mm ~55000 g mol^{-1}) were purchased from Sigma-Aldrich. Hydrogen peroxide (H_2O_2, 30 %) and sodium hydroxide (NaOH, >97 %) were purchased from Anidrol and Synth, respectively. The glassware was cleaned with *aqua regia* solution (3:1 v/v, HCl:HNO_3) and washed with deionized water before the synthesis. For the sample decomposition, all reagents were purchased from Merck, and for microwave-assisted acid decomposition and standard/sample dilutions, sub-boiling nitric acid was employed. Before using, all glassware was cleaned with 10 % (v/v) HNO_3 and rinsed with deionized water. Throughout all this work, it was used deionized water (≥18.2 MΩ cm) from a Milli-Q water purification system (Millipore).

2.2.2 Synthesis of Metallic Nanoparticles

2.2.2.1 Synthesis of AuNR

AuNR synthesis was performed via a seed-mediated growth method following the procedure reported by Xu et al.[90] First, AuSeed nanoparticles were synthesized. In a round-bottom flask immersed in a water bath at 28 °C, 40.5 µL 1 % (w/v) $HAuCl_4$ was added to 4 mL 0.1 mol L^{-1} CTAB under stirring. Then, 24 µL 0.1 mol L^{-1} $NaBH_4$ was added to this solution. The stirring was stopped after 2 min and the colloid was aged at least for 2 h.

The second step consists of AuNR growth. 50 mL 0.1 mol L^{-1} CTAB, 20 µL 0.1 mol L^{-1} $AgNO_3$, and 1.03 mL 24.28 mmol L^{-1} $HAuCl_4$ were added in a round-bottom

flask immersed in a water bath at 28 °C. Next, 163 µL 1 mol L^{-1} NaOH and 27.5 µL 30 % H_2O_2 were added and the solution was stirred for 1 min 150 µL of the seed colloid was added and the stirring was maintained for 30 s. The stirring was stopped, and the solution was kept at 28 °C at least for 1.5 h.

2.2.2.2 Synthesis of Au@AgNR

AuNR_Core synthesis was performed via a seed-mediated growth method following the procedure reported by Xu et al.[90] First, AuSeed nanoparticles were synthesized. In a round-bottom flask immersed in a water bath at 28 °C, 40.5 µL 1 % (w/v) $HAuCl_4$ was added to 4 mL 0.1 mol L^{-1} CTAB under stirring. Then, 24 µL 0.1 mol L^{-1} $NaBH_4$ was added to this solution. The stirring was stopped after 2 min and the colloid was aged at least for 2 h.

The second step consists of AuNR_Core growth. 50 mL 0.1 mol L^{-1} CTAB, 50 µL 0.1 mol L^{-1} $AgNO_3$, and 1.03 mL 24.28 mmol L^{-1} $HAuCl_4$ were added in a round-bottom flask immersed in a water bath at 28 °C. Next, 215 µL 1 mol L^{-1} NaOH and 28.5 µL 30 % H_2O_2 were added and the solution was stirred for 1 min 150 µL of the seed colloid was added and the stirring was maintained for 30 s. The stirring was stopped, and the solution was kept at 28 °C at least for 1.5 h. The AuNR colloid was washed by centrifugation (8100 *g* for 60 min), where the supernatant was discarded, and the settled colloid was resuspended in the same volume of deionized water as the discarded supernatant.

The Au@AgNR synthesis was performed following the procedure reported by Fu et al.[91] 8 mL of AuNR colloid was dispersed in 40 mL of 2 % (w/v) PVP (Mm ~ 55 000 g mol^{-1}). Then, 3 mL of 1 mmol L^{-1} $AgNO_3$ and 1 mL of 0.1 mol L^{-1} L-ascorbic acid were added in this order to the AuNR colloid under slowly stirring at room temperature. After 2 min, 5 mL of 0.1 mol L^{-1} NaOH was quickly added. The reaction finished in a few minutes, where no further change in color was observed.

2.2.2.3 Synthesis of AuSph

Gold nanospheres (AuSph) were synthesized via a seed-mediated growth method. First, ca. 16 nm AuSeed nanoparticles were synthesized according to the

Turkevich method[92] in which Au^{3+} ions are reduced by sodium citrate. Briefly, 250 mL of 0.5 mmol L^{-1} $HAuCl_4$ was heated to boiling, and 12.5 mL 1 % (w/v) sodium citrate was added to it under vigorous stirring. The heating and stirring were stopped after 17 min, and the colloid suspension was cooled to room temperature.

AuSph growth was performed following the procedure described by Rodriguéz-Fernández et al.[93] 1 mL of 100 mmol L^{-1} L-ascorbic acid was added to 48.37 mL of an aqueous solution containing 1 mmol L^{-1} $HAuCl_4$ and 15 mmol L^{-1} CTAB, followed by the fast addition of 630 μL of 0.77 mmol L^{-1} AuSeed (concentration in terms of Au^0). The reaction was allowed reacting at 35 °C for 1 h in a thermostatic bath.

2.2.3 Separation Method for Obtaining the Metallic Nanoparticles Fractions

2.2.3.1 Separation Method for AuNR Fractions

After the synthesis of AuNR, the final colloids were separated into three fractions. In the protocol adapted from Galazzi et al.[89], the colloid obtained at the end of the synthesis was named as AuNR-total. Part of AuNR-total was centrifuged in eppendorf at 8100 *g* resulting in the fractions of supernatant (AuNR-sup) and the settled AuNRs (pellet) resuspended in deionized water (AuNR-res) (n=3). The centrifugation time was optimized to achieve a baseline signal for the AuNR-sup fraction, which indicates the major content of AuNR was settled. The optimization of the centrifugation time was monitored by the VIS-NIR extinction spectrum of AuNR-sup obtained at different times. Finally, the total content of gold of AuNR-total, AuNR-res, and AuNR-sup samples was determined.

2.2.3.2 Separation Method for AuSph Fractions

The AuSph colloid was also separated into three fractions: AuSph-total (colloid after synthesis), AuSph-sup (supernatant), and AuSph-res (settled AuSph resuspended in deionized water) (n=3). The centrifugation was realized in eppendorf at 1055 *g*, and the centrifugation time was also optimized to achieve a baseline signal for the AuNR-sup fraction. The optimization of the centrifugation time was monitored by the VIS-NIR extinction spectrum of AuSph-sup obtained at different times. Finally,

the total content of gold of AuSph-total, AuSph-res, and AuSph-sup samples was determined.

2.2.4 Characterization of Metallic Nanoparticles

UV-VIS-NIR spectra of the samples were recorded on a Varian Cary® 50 and Shimadzu UV-2450 spectrophotometer. UV-VIS-NIR extinction spectra were recorded with path lengths of 5 or 10 mm. Transmission electron microscopy (TEM) images of AuNR and AuSph colloids were recorded on a Zeiss–Libra operating at 80 kV, JEOL JEM-2100 operating at 200 kV, and JEOL JEM 1010 operating at 100 kV transmission electron microscopes. The Energy Dispersive X-ray Spectroscopy (EDS) mapping characterization of Au@AgNR was recorded by the acquisition of high-angle annular dark-field (HAADF-STEM) images in an FEI Titan Themis cubed 60-300 aberration-corrected scanning transmission electron microscope operating at 300 kV. Compositional maps were acquired by EDS spectrum imaging using a Super-X detector controlled by an FEI Velox software. The samples of TEM, HAADF-STEM, and EDS mapping were prepared by directly drop-drying the colloid on a holey carbon-coated Cu grid (sample holder).

2.2.5 Gold Quantification in Metallic Nanoparticles

The fractions obtained were subjected to microwave-assisted acid decomposition using DTG-100 microwave oven (Provecto Analitica, Jundiaí, Brazil) with Teflon® vessels (maximum volume of 90 mL) and a magnetron of 2450 ± 13 MHz with a nominal power of 1200W. For this task, the optimization of the decomposition method was carried out to achieve appropriate conditions for sample preparation by mixing a 200 µL of each fraction with distinct reactants and following different microwave programs divided into some steps, as shown in Table 2.1. The microwave programs were performed twice. Each fraction was decomposed in quadruplicate and separated from the other fractions. In this way, the tubes containing samples were equally distributed in the microwave oven together with tubes containing those respective blanks. The decomposed samples were diluted up to 25 mL with deionized water.

Table 2.1. Microwave-assisted decomposition procedures tested in this work to decompose AuNR-total, AuNR-res, and AuNR-sup.

Procedure	Volume of AuNR fraction (mL)	Reagents	Microwave Program
1	3	4 mL HNO_3 + 0.5 mL H_2O_2	5'@400W, 8'@790W, 4'@320W, 3'@0W
2	3	4 mL HNO_3 + 1 mL H_2O_2	5'@400W, 8'@790W, 4'@320W, 3'@0W
3	3	4 mL *aqua regia* (3HCl:1HNO_3) + 1 mL H_2O_2	5'@400W, 8'@790W, 4'@320W, 3'@0W
4	3	4 mL reverse *aqua regia* (1HCl:3HNO_3) + 2 mL H_2O_2	5'@400W, 8'@790W, 4'@320W, 3'@0W
5	2	4 mL reverse *aqua regia* (1HCl:3HNO_3) + 2 mL H_2O_2	5'@400W, 8'@790W, 4'@320W, 3'@0W
6	2	4 mL reverse *aqua regia* (1HCl:3HNO_3) + 1 mL H_2SO_4+ 2 mL H_2O_2	Without digestion
7	2	4 mL reverse *aqua regia* (1HCl:3HNO_3) + 1 mL H_2SO_4	5'@400W, 20'@790W, 4'@320W, 3'@0W
8	2	4 mL reverse *aqua regia* (1HCl:3HNO_3) + 1 mL H_2SO_4	5'@400W, 40'@790W, 4'@320W, 3'@0W

Table 2.1. (continued).

Procedure	Volume of AuNR fraction (mL)	Reagents	Microwave Program
9	2	4 mL reverse *aqua regia* (1HCl:3HNO_3) + 1 mL H_2SO_4	**1st Step:** 5'@400W, 40'@790W, 4'@320W, 3'@0W **2nd Step:** 5'@400W, 20'@790W, 4'@320W, 3'@0W
10	1	4 mL reverse *aqua regia* (1HCl:3HNO_3) + 1 mL H_2SO_4	**1st Step:** 5'@400W, 40'@790W, 4'@320W, 3'@0W **2nd Step:** 5'@400W, 20'@790W, 4'@320W, 3'@0W
11	1	4 mL reverse *aqua regia* (1HCl:3HNO_3) + 1 mL H_2SO_4	**1st Step:** 5'@400W, 40'@790W, 4'@320W, 3'@0W **2nd Step:** 5'@400W, 20'@790W, 4'@320W, 3'@0W Separated digestion of each fraction
12	1	4 mL reverse *aqua regia* (1HCl:3HNO_3) + 1 mL H_2SO_4	**1st Step:** 5'@400W, 40'@790W, 4'@320W, 3'@0W **2nd Step:** 5'@400W, 40'@790W, 4'@320W, 3'@0W Separated digestion of each fraction
13	0.5	4 mL reverse *aqua regia* (1HCl:3HNO_3) + 1 mL H_2SO_4	**1st Step:** 5'@400W, 40'@790W, 4'@320W, 3'@0W **2nd Step:** 5'@400W, 40'@790W, 4'@320W, 3'@0W Separated digestion of each fraction
14	0.2	4 mL reverse *aqua regia* (1HCl:3HNO_3) + 1 mL H_2SO_4	**1st Step:** 5'@400W, 40'@790W, 4'@320W, 3'@0W **2nd Step:** 5'@400W, 40'@790W, 4'@320W, 3'@0W Separated digestion of each fraction

The decomposed samples were appropriately diluted (Table A.1, Appendix A) and the gold content in the sample was determined. The Au quantification in the solutions was performed on Elan DRC-e quadrupole ICP-MS (PerkinElmer, Norwalk, CT, USA) and iCAP 6000 Series ICP OES (Thermo Fisher Scientific, England). The ICP-MS is located inside a 10000 class clean room and equipped with a dynamic reaction/collision cell for interference remotion. The sample introduction system for both instruments comprises a glass Meinhard® concentric nebulizer and a cyclonic glass spray chamber.

2.3 RESULTS AND DISCUSSION

2.3.1 Metallic Nanoparticles Characterization

The MNPs were characterized by UV-VIS spectroscopy, TEM, HAADF-STEM, and EDS mappings, as shown in Figure 2.1. Figure 2.1a shows a representative TEM image of AuNR confirming the formation of the nanoparticles with large size and morphology homogeneity, with an average length and diameter of 56.9 ± 10.7 and 19.3 ± 3.3 nm, respectively, and an average aspect ratio (ratio of length and diameter dimensions) of 3.0 ± 0.6, as determined by TEM analysis (n=250). The histograms of the diameter and length size of AuNR nanoparticles are shown in Figure A.1 (Appendix A). Moreover, Figure 2.1b presents the VIS-NIR extinction spectrum of AuNR with the characteristic LSPR bands of rod-shaped nanoparticles at 740 and 518 nm associated with longitudinal (direction of the length) and transversal (direction of the diameter) LSPR, respectively.[94]

Figure 2.1c shows a representative HAADF-STEM image and the EDS mapping of Au@AgNR showing the hierarchical structure of the core-shell nanorod, where it is observed a core of AuNR and a homogeneous shell of Ag. The Au@AgNR shows a thicker Ag shell across the lateral side of the AuNR and a thinner one at the end of the nanoparticle. AuNR_Core nanoparticles presented an average length and diameter of 41.4 ± 6.2 and 11.0 ± 1.1 nm (n=250), respectively, and an average aspect ratio of 3.8 ± 0.6. A representative TEM image and histograms of diameter and length size of AuNR_Core nanoparticles are shown in Figure A.2 (Appendix A). The Ag shell

presented a thickness between 0.2–1.4 and 0.9–2.8 nm at the end and lateral side of the nanoparticle, respectively, leading to an average aspect ratio of 3.0 ± 0.6 (n=8).

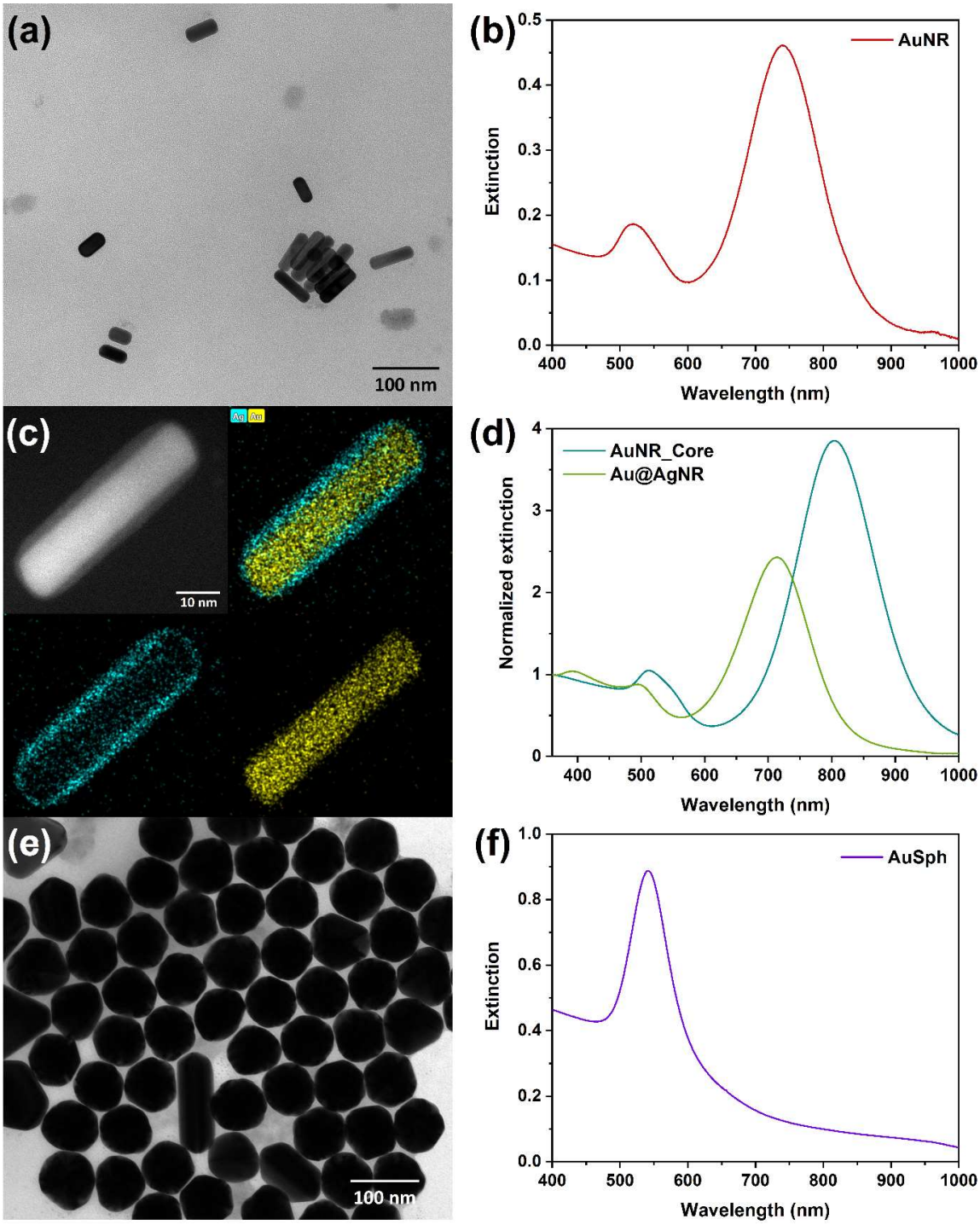

Figure 2.1. (a) TEM image and (b) VIS-NIR extinction spectrum of AuNR. (c) HAADF-STEM image and EDS mapping of Au@AgNR, indicating the presence of silver (blue) and gold (yellow). (d) UV-VIS-NIR extinction spectrum of AuNR_Core and Au@AgNR (normalized at 360 nm for comparison). (e) TEM image and (f) VIS-NIR extinction spectrum of AuSph.

Figure 2.1d presents a comparison between the UV-VIS-NIR extinction spectra of AuNR_Core and Au@AgNR. AuNR_Core shows the characteristic longitudinal and transversal LSPR bands at 804 and 513 nm, respectively. Au@AgNR shows the longitudinal and transversal LSPR bands of the AuNR_Core shifted to 714 and 495 nm, respectively. The blueshift of the LSPR bands (Figure 2.1d) is related to the influence of the optical properties of Ag on the nanoparticle in conjunction with the decrease of the aspect ratio of the nanoparticles by the formation of a thicker Ag shell on the lateral side of the nanorod.[95] Besides, the change in the dielectric constant of the surrounding medium of the AuNR_Core from water to the silver shell also contributes to the blueshift of the LSPR bands.[96] The transversal LSPR shows a smaller blueshift than the longitudinal band since the first one is less sensitive to the aspect ratio.[95] Finally, Au@AgNR shows an additional LSPR band at 392 associated with the longitudinal LSPR from the outer Ag shell surface.[97]

Figure 2.1e shows a representative TEM image of AuSph confirming the formation of the nanoparticles with a relatively high size and shape homogeneity. According to TEM analysis, the Ausph nanoparticles present an average diameter of 76.3 ± 3.5 nm (n=250). Figure 2.1f shows the VIS-NIR extinction spectrum of AuSph, which presents a dipole mode LSPR at 540 nm.

2.3.2 Separation of the Metallic Nanoparticle Fractions

After the synthesis of AuNR, the colloid was separated into three fractions by a centrifugation process, as presented in the Experimental section (section 2.2.3). The acceleration of centrifugation was set at 8100 *g*, and the time of centrifugation was optimized according to the extinction spectrum of the supernatant until it did not present the LSPR bands characteristics of AuNR. The optimization of centrifugation time was studied in the range from 10 up to 60 min, and the time of 60 min originated the best separation result, as shown in Figure 2.2a. The synthesis condition for the AuNR presented in the centrifugation optimization (Figure 2.2a) is described in Appendix A.

Figure 2.2b presents the extinction spectra of all three fractions of AuNR after following the optimized separation process of 8100 *g* for 60 min. As can be seen, the extinction spectrum of AuNR-sup is overlapped with the extinction spectrum of the blank (water), a baseline signal, indicating that a major content of nanorods was settled

and the absence of nanoparticles in the AuNR-sup fraction. Additionally, it is observed no change in the optical properties between the fractions AuNR-total and AuNR-res, which indicates the size and morphology of the nanoparticles were maintained during the separation process.

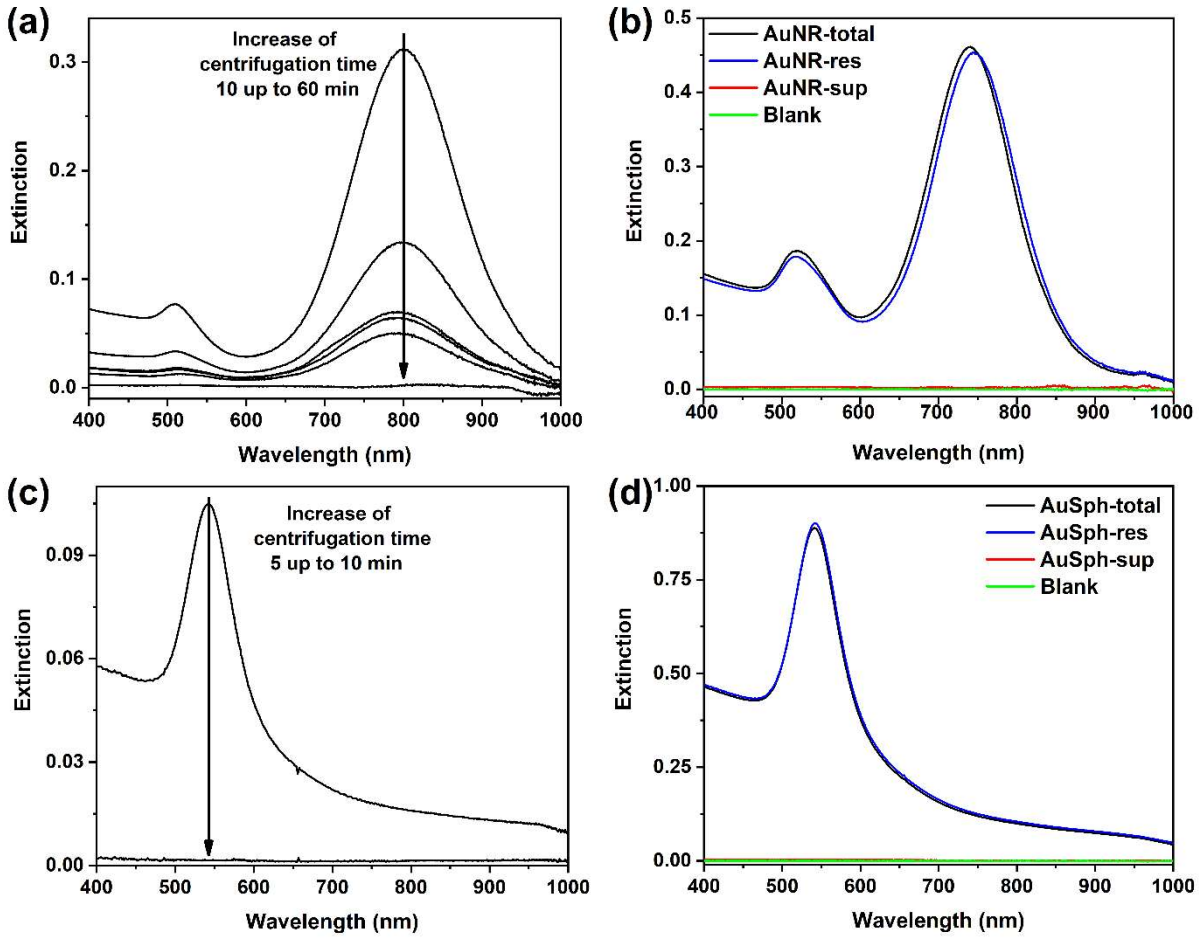

Figure 2.2. (a) Optimization of the centrifugation time for the separation of the AuNR fractions (8100 *g*, step of 10 min). (b) VIS-NIR extinction spectra of the fractions AuNR after the separation by the optimized centrifugation process of 8100 *g* for 60 min. (c) Optimization of the centrifugation time for the separation of the AuSph fractions (1055 *g*, step of 5 min). (d) VIS-NIR extinction spectra of the fractions AuSph after the separation by the optimized centrifugation process of 1055 *g* for 10 min. For (a) and (c), the VIS-NIR extinction spectra correspond to the supernatant fractions derived from each centrifugation process.

The centrifugation process for the separation of AuSph fractions was also optimized. For this, the acceleration of centrifugation was set at 1055 *g*, and the time of centrifugation was optimized. Figure 2.2c shows the VIS-NIR extinction spectra of AuSph-sup derived from the centrifugation process applied for 5 and 10 min, where

the latter was chosen as the optimized condition. The extinction spectra of all three fractions of AuSph after following the optimized separation process (1055 *g* for 10 min) are shown in Figure 2.2d. As previously observed for AuNR, the overlap of the extinction spectra of the blank (water) and AuSph-sup suggests the efficiency of the separation process to settle the major content of AuSph, giving rise to a nanoparticle-free supernatant. Moreover, no change in the size and morphology of the nanoparticles after the separation process is displayed by the similar optical properties observed for AuSph-total and AuSph-res.

2.3.3 Microwave-assisted Decomposition Platform

After the separation and characterization of the samples, distinct microwave-assisted decomposition procedures were considered to quantify the gold content in each fraction of AuNR. Table 2.1 presents all the procedures tested in this work for the AuNR fractions, with the details of sample volume and acidic mixtures, as well as the microwave programs.

The first decomposition method used was the one established by Galazzi et al.[89] for the decomposition of silver nanoparticles stabilized by sodium citrate. The method (procedure 1 in Table 2.1) is based on the acidic mixture of 4 mL nitric acid, 0.5 mL hydrogen peroxide, and 3 mL of the colloid fraction. The microwave program applied consists of four steps: 5 min at 400 W, 8 min at 790 W, 4 min at 320 W, and 3 min at 0 W. Since this method was unsuccessful for decomposing the AuNR fractions, other strategies were tested. In summary, different acidic mixtures of reverse *aqua regia* (1:3 v/v, HCl:HNO_3), sulfuric acid, and hydrogen peroxide were tested as well as various sample volumes (from 3.0–0.2 mL). The microwave program was also adjusted, where it was studied the increase of the program runtime, the application of two consecutive microwave program cycles, and the decomposition of each AuNR fraction separately.

As observed in Table 2.1, several strategies were needed in our study, since those total and supernatant fractions of AuNR contain a significant amount of organic matter by the presence of CTAB in the AuNR synthesis. Then, the high content of CTAB became a challenge to decompose such samples. For almost all evaluated

procedures, it was possible to visualize the presence of residue after the acidic decomposition, which may affect the accuracy of elemental determination results.

Figure 2.3 exhibits some photographs of AuNR-total samples diluted in deionized water after some microwave-assisted decomposition procedures. As previously mentioned, the organic matter of the fractions is constituted by CTAB, a cationic surfactant widely used in the AuNR synthesis as a shape-directing agent and stabilizer.[50,83,98] Distinct reports in the literature have demonstrated that CTAB stabilizes the AuNR by forming a bilayer structure possibly by an interdigitation of the alkyl chain (Figure 2.4), presenting a bilayer thickness of 3.2 ± 0.2 nm.[99–101]

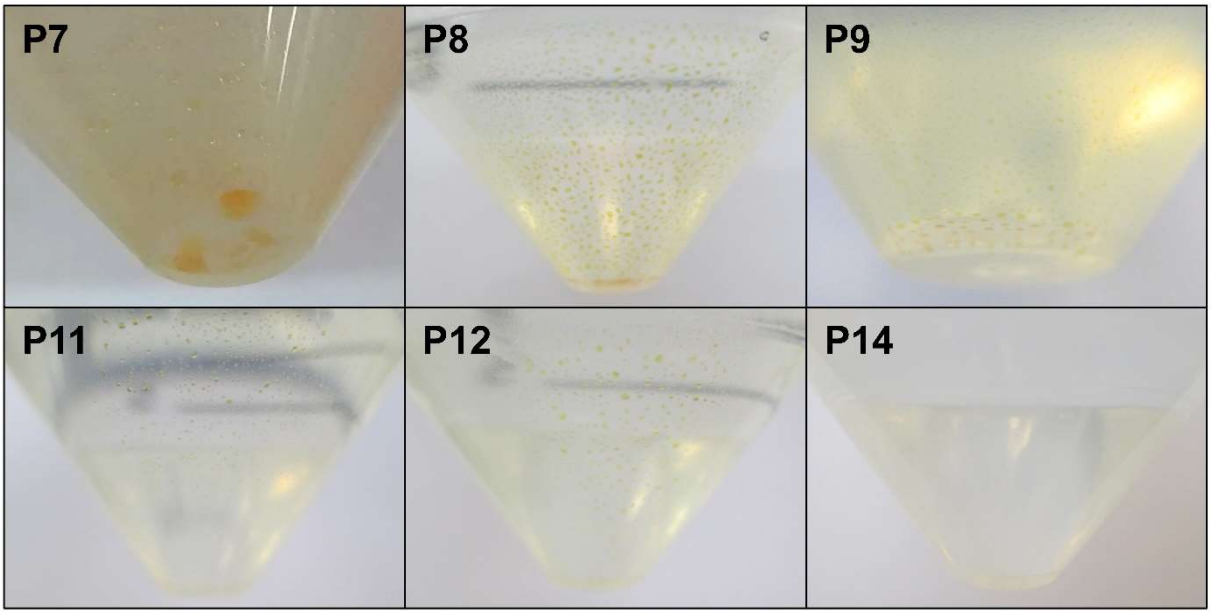

Figure 2.3. Photographs of AuNR-total samples diluted in deionized water after the corresponding microwave-assisted decomposition procedure. The numbers in each photograph correspond to the evaluated procedures shown in Table 2.1.

Therefore, the residue observed by the incomplete decomposition of CTAB probably involves the non-decomposed gold nanoparticles, preventing the release of the Au^{3+} ions to the solution. Although the presence of residue was not noticeable in some samples, poorly reproducibility of Au determination between replicates indicated the incomplete decomposition of the samples. It is possible to observe the efficiency evolution of the tested decomposition procedures by the photographs presented in Figure 2.3. There is a decrease in the amount of residue from P7 (in this case, an opaque solution is also observed) up to P12, and P14 presented a clear solution, which

indicates a complete matrix decomposition with subsequent Au^{3+} ions release after the microwave-assisted procedure.

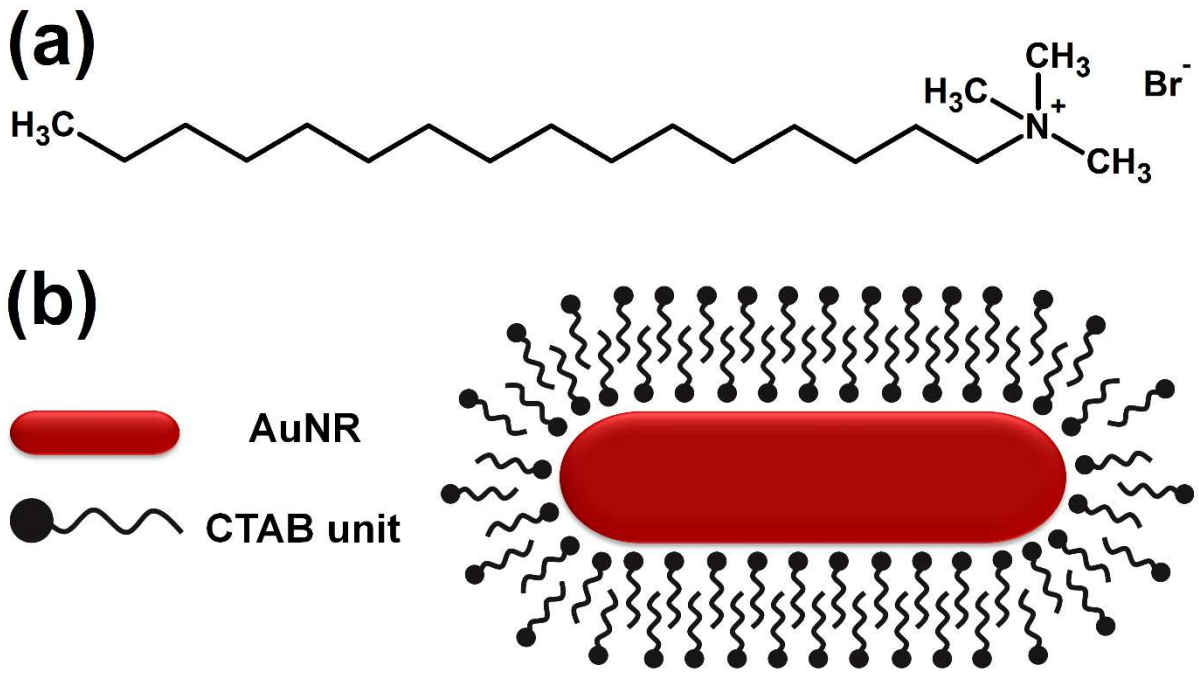

Figure 2.4. (a) Chemical structure of cetyltrimethylammonium bromide (CTAB). (b) Representation of the stabilization of the AuNR by a bilayer structure of the CTAB molecules by an interdigitation of the alkyl chains.

After the optimization of the microwave-assisted decomposition procedure, procedure 14 (Table 2.1) was applied for the determination of gold content in the AuNR fractions. The procedure 14 consist of the decomposition of 200 μL of AuNR fraction with 4 mL of reverse *aqua regia* (1:3 v/v, HCl:HNO_3) and 1 mL of sulfuric acid, and two cycles of the microwave program with the steps of 5 min at 400 W, 40 min at 790 W, 4 min at 320 W, and 3 min at 0 W. Additionally, the AuNR fractions were decomposed separately.

After the microwave-assisted decomposition of the AuNR fractions, the determination of gold content in the samples was performed by both ICP OES and ICP-MS to check the accuracy of the results. Table 2.2 presents the figures of merit of both techniques, and Table 2.3 shows the results for the gold quantification. Additional instrumental and measurement parameters of the techniques are shown in Table A.2 (Appendix A), and the calibration curves for both methods are shown in Figure A.3 (Appendix A). According to the experimental procedure for the AuNR synthesis, a gold

concentration of *ca.* 96 mg L^{-1} is expected for AuNR-total, regardless if gold is resultant from nanoparticles (Au^0) or ionic form derived from unreacted precursors (in this case Au^+, since during the growth of AuNR, the ion Au^{3+} is reduced to Au^+, and then Au^+ is reduced to Au^0).[83,90]

Table 2.2. Figures of merit obtained for the gold quantification by ICP OES and ICP-MS.

	ICP OES	**ICP-MS**
Linear range (μg L^{-1})	50–250	1–10
LOD[a]	3.8 μg L^{-1}	4.3 ng L^{-1}
LOQ[b]	12.8 μg L^{-1}	14.4 ng L^{-1}

[a] LOD: detection limit. Defined as 3 times the standard deviation of 20 measurements of the blank divided by the slope of the calibration curve.
[b] LOQ: quantification limit. Defined as 10 times the standard deviation of 20 measurements of the blank divided by the slope of the calibration curve.

Table 2.3. Gold quantification in AuNR-total, AuNR-res, and AuNR-sup by ICP OES and ICP-MS.

Technique	**Fraction**	**Gold concentration (mg L^{-1})[a]**	**% Au in solution**
ICP OES	AuNR-total	102.5 ± 4.6	100
	AuNR-res	103.4 ± 1.7	101
	AuNR-sup	< LOQ	-
ICP-MS	AuNR-total	93.9 ± 7.4	100
	AuNR-res	98.3 ± 3.8	105
	AuNR-sup	0.49 ± 0.06	1

< LOQ: below the quantification limit.
[a] Results expressed as average value ± standard deviation of triplicates of each fraction (n=3).

Our results are in agreement with the expected Au concentration since the gold concentration determined in AuNR-total was found as 102.5 ± 4.6 and 93.9 ± 7.4 mg L^{-1} by ICP OES and ICP-MS, respectively (Table 2.3). This fact suggests that the optimized microwave-assisted decomposition procedure led to the complete decomposition of the matrix with subsequent Au^{3+} ions release, providing accurate

results for the determination of gold concentration in AuNR. Besides, the gold content of AuNR-sup was found below LOQ for ICP OES and detected as 0.49 ± 0.06 mg L^{-1} in the sample by ICP-MS, considering the proper dilutions (see Table A.1). The low gold concentration found in AuNR-sup possibly derives from unreacted precursor (Au^{+} ions) and/or small gold nanospheres that were not separated from supernatant during the centrifugation process with the bigger nanoparticles.

Additionally, comparing the results of AuNR-total and AuNR-res, and considering the low Au concentrations observed in AuNR-sup, the synthesis of AuNR exhibits high yield in the AuNR growth, presenting *ca.* 100 % of the gold content in the AuNR-res. Test-*t* and Test-F were applied to check the statistical inference between the results of each fraction from both techniques, and the results showed no statistical difference between the determined values.

Once the efficiency and reliability of the microwave-assisted decomposition procedure were proven, the procedure was applied for the gold quantification in Au@AgNR colloid. The gold quantification in the Au@AgNR becomes a new challenge to be overcome since the Au@AgNR colloid contains the polymer PVP (Mm ~ 55000 g mol^{-1}) as a stabilizer in addition to the complex matrix with CTAB. Therefore, the application of the developed microwave-assisted decomposition procedure is of utmost importance for the gold quantification in this sample. To confirm the reliability of the microwave-assisted decomposition procedure for the gold quantification in Au@AgNR, the gold concentration determined in Au@AgNR was compared to the gold concentration verified in AuNR_Core, since the same value is expected for both cases.

Table 2.4 presents the results for the gold concentration by ICP-MS for both samples (the respective calibration curve is shown in Figure A.2c, Appendix A). The results show accordance between the values of the gold concentration for AuNR_Core (104.0 ± 7.9 mg L^{-1}) and Au@AgNR (105.3 ± 14.5 mg L^{-1}). The gold concentration recovery of *ca.* 100 % confirms the complete decomposition of the nanoparticles and the organic matter, releasing the Au^{3+} ions to the solution. Additionally, the gold concentration determined for both samples agrees with the expected gold concentration regarding the results for the sample AuNR shown in Table 2.3.

Table 2.4 also shows the results for the gold quantification of the AuSph fractions by ICP-MS (the respective calibration curve is shown in Figure A.2c, Appendix A). A gold concentration of *ca.* 199 mg L^{-1} is expected for AuSph-total according to the

experimental procedure for the AuSph synthesis, regardless if gold is resultant from nanoparticles (Au^0) or ionic form (Au^+) derived from unreacted precursors (since during the growth step, Au^{3+} is first reduced to Au^+, and then Au^+ is reduced to Au^0, as occurs in the AuNR synthesis).

Table 2.4. Gold quantification in AuNR_Core, Au@AgNR, AuSph-total, AuSph-res, and AuSph-sup by ICP-MS.

Sample	Gold concentration (mg L^{-1})[a]	% Au in solution
AuNR_Core	104.0 ± 7.9	100
Au@AgNR	105.3 ± 14.5	101
AuSph-total	195.9 ± 24.0	100
AuSph-res	223.8 ± 25.8	114
AuSph-sup	1.2 ± 0.1	1

[a] Results expressed as average value ± standard deviation of replicates of each fraction (n=2 and 3 respectively for AuSph fractions and the samples AuNR and Au@AgNR).

Our results agree with the expected gold concentration since it was found a gold concentration of 195.9 ± 24.0 mg L^{-1} in AuSph-total (Table 2.4). This result confirms the complete decomposition of the matrix with subsequent Au^{3+} ions release by the optimized microwave-assisted decomposition procedure. Moreover, the gold content of 1.2 ± 0.1 mg L^{-1} was found for AuSph-sup, which possibly derives from unreacted precursor (Au^+ ions) and/or small gold nanospheres that were not separated from supernatant during the centrifugation process with the bigger nanoparticles. Considering the low gold concentration in AuSph-sup and comparing the results of AuSph-total and AuSph-res, the synthesis of AuSph displays high yield in the AuSph growth, presenting *ca.* 114 % of gold content in the AuSph-res.

Finally, the gold quantification results (Table 2.3 and 2.4) confirm that the UV-VIS method[83] (where the correlation between the gold concentration and the extinction value at 400 nm in the extinction spectra is used) is suitable for the gold quantification of the AuNR and AuSph colloids, however, it is improper for Au@AgNR colloid. According to the UV-VIS method, the AuNR-total, AuSph-total, and Au@AgNR colloids present a gold concentration of *ca*. 102, 229, and 240 mg L^{-1}, respectively.

The accuracy of the UV-VIS method for the AuNR-total and AuSph-total is explained by the absence of any interference in the extinction profile at 400 nm for both colloids (Figure 2.1b and 2.1f). Meanwhile, Au@AgNR presents an LSPR mode at 392 nm (Figure 2.1d) that gives rise to an overestimated gold concentration by *ca*. 240 % for Au@AgNR.

2.4 CONCLUSIONS

The initial purpose of this work was successfully attained. In conclusion, we report a complete platform of strategies for characterization and microwave-assisted decomposition procedure as a tool for the gold quantification in MNPs. AuNR nanoparticles were synthesized in a matrix with a high-content of the surfactant CTAB for the development of the procedure.

Several decomposition procedures were tested due to the high content of organic matter derived from the presence of CTAB in the nanoparticle synthesis. The strategy that resulted in the best reproducibility of the gold determination is an acidic decomposition consisted of a mixture of reverse *aqua regia* (1:3 v/v, HCl:HNO_3) and sulfuric acid and a powerful microwave program. Besides, the proposed decomposition procedure allows a low sample volume consumption, since only 200 µL of sample is needed. The gold quantification of the three fractions of the sample (AuNR-total, AuNR-res, and AuNR-sup) by ICP OES and ICP-MS after the performance of the developed procedure were accurate. The results show a high yield for the AuNR synthesis, demonstrating that both AuNR-total and AuNR-res fractions present *ca.* 100 % of the gold content. The microwave-assisted decomposition platform was also effective in the gold quantification of AuSph by ICP-MS, demonstrating a high yield for the AuSph synthesis with *ca.* 100 and 114 % of gold content for AuSph-total and AuSph-res fractions, respectively.

The microwave-assisted decomposition procedure was also applied for the gold quantification in the core-shell nanoparticle Au@AgNR, which presents PVP as a stabilizer in addition to the matrix with CTAB. The results demonstrated an efficient decomposition of the Au@AgNR matrix and an accurate gold quantification was obtained, presenting a gold concentration recovery of *ca.* 100 %. Moreover, the quantification results confirm that the UV-VIS method is improper for the gold

quantification in the Au@AgNR colloid, leading to an overestimated gold concentration of *ca*. 240 %. In contrast, the UV-VIS method was suitable for the gold quantification in AuNR and AuSph colloids.

Although it was not the goal of our study, the proposed decomposition procedure would allow a bimetallic quantification of gold and silver in the Au@AgNR by improving the separation method of the colloid fractions, resulting in the determination of the yield of both core and shell growth. Moreover, the decomposition procedure, in conjunction with specific methods for the separation of nanoparticles with different morphologies, would allow the determination of the synthesis yield based on the differentiation of the desired morphology and byproducts.

In summary, the results obtained by the microwave-assisted decomposition platform demonstrate robustness, efficiency, and reliability. The proposed procedure demonstrated to be an excellent method in the gold quantification of MNPs, such as AuNR, AuSph, and Au@AgNR colloids with complex matrices and a high content of organic matter without the need for additional separation methods for the elimination of matrix interferences. Finally, the microwave-assisted decomposition procedure proposed in this report overcomes the limitations verified for other quantification methods, such as UV-VIS spectroscopy by the gold quantification in bimetallic MNPs. The method shows a high potential for its application as a characterization tool for types of multi-metallic nanostructures, such as alloy and Janus nanoparticles.

2.5 CRediT Authorship Contribution Statement

This work presents the following individual author contributions:

- **Naiara Vieira Godoy:** methodology, investigation, writing - original draft, and formal analysis.
- **Rodrigo Moretto Galazzi:** methodology, investigation, and writing – review & editing.
- **Katherine Chacón-Madrid:** methodology, and investigation.
- **Marco Aurélio Zezzi Arruda:** conceptualization, supervision, writing – review & editing, project administration, resources, and funding acquisition.

- **Italo Odone Mazali:** conceptualization, supervision, writing – review & editing, project administration, resources, and funding acquisition.

2.6 ACKNOWLEDGMENTS

I would like to thank Professor Dr. Marco Aurélio Zezzi Arruda (GEPAM, Institute of Chemistry, UNICAMP) for the supervision on the development of this work, Dr. Rodrigo M. Galazzi, and M.Sc. Katherine Chacón-Madrid for the collaborative work on the development of this study. I would like to thank Raisa Alves Siqueira, Flávia de Sousa Ferreira, and Douglas Soares da Silva for the acquisition of TEM images. I would like to thank Érico Teixeira Neto for the acquisition of HAADF-STEM images and EDS mapping. I would like to thank Daniel Carneiro Freitas and Pedro dos Santos Moreau for the assistance in the experimental development.

3 PAPER-BASED INKJET-PRINTED SERS SENSOR

The content of this chapter is an adaptation of the article entitled “Ultrasensitive inkjet-printed based SERS sensor combining a high-performance gold nanosphere ink and hydrophobic paper” by N.V. Godoy, D. García-Lojo, F.A. Sigoli, J. Pérez-Juste, I. Pastoriza-Santos, I.O. Mazali, reference 102.

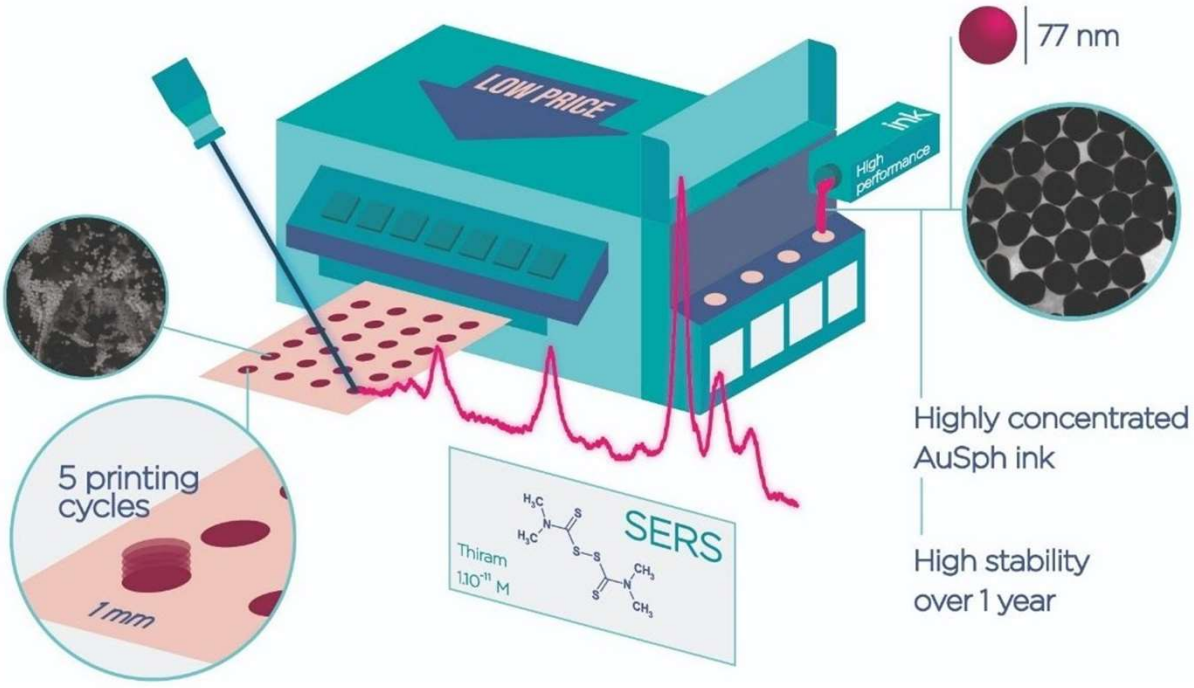

Naiara Vieira Godoy

3.1 INTRODUCTION

Surface-Enhanced Raman Spectroscopy (SERS) is a versatile analytical technique widely used for qualitative and quantitative analysis.[95,103–106] The main advantages that make this technique so versatile are the simple measurement acquisition, shorter time for sample preparation and analysis, low (or non) consumption of solvents, among others. Additionally, Raman scattering exhibits sharply and discernible molecular fingerprint bands with high multiplexing potential in biosensing and bioimaging applications.[35] One of the main features for this technique is the low detection limit (LOD) that can be achieved in the order of 10^{-9}–10^{-12} mol L^{-1} and has a high potential to reach ultralow detection limits as low as 10^{-13} and 10^{-20} mol L^{-1} measured in small amounts of sample (few microliters).[26,27,107–109] Owing to its high sensitivity, SERS is widely applied in several areas that require low LOD, such as food safety,[110,111] drug detection,[112,113] detection of viruses [114] and investigation of bioactive metabolites in microbial communities.[62]

In SERS, the Raman scattering of molecules is greatly enhanced when the molecules are adsorbed onto rough metal surfaces or metal nanoparticles, such as silver or gold nanoparticles. The main responsible factor for the high SERS intensity is the localized surface plasmon resonance (LSPR) of the metallic nanoparticles (MNPs) which leads to an enhancement of the electric field in their vicinity.[115] Although the SERS effect can be obtained from the electric field enhancement at single nanoparticles, a considerable higher enhancement can be reached by placing the molecules within nanometer-sized gaps between two MNPs (so-called hot spots). The electric field enhancement at the hot spot effect is majorly important at low concentrations, particularly at the single-molecule SERS regime (SM-SERS regime), since a molecule adsorbed on a hot spot can lead to a SERS intensity 10^2 up to 10^5 higher than several molecules adsorbed on random nanoparticles.[60,115]

The development of new SERS platforms has been widely explored because of the high demand for analysis with a low LOD in several fields. The ideal SERS substrate should be highly stable and reproducible in terms of SERS activity and also cost-effective. In this way, extensive research is being carried out to improve the SERS efficiency by using versatile shape- and size-controlled plasmonic nanoparticles.[47,48,116,117] From the point of view of the substrate and particularly the

nanoparticle deposition, different methodologies have been explored, such as electrospinning,[118] self-assembly,[116,119] and electro-deposition combined with lithography.[120]

Alternatively, the use of paper as a platform for the fabrication of SERS-active surfaces has been explored since the mid-1980.[121–124] The use of paper as a SERS-active surface is a very attractive strategy that displays many advantages over conventional SERS substrates, such as the low-cost, flexibility, high commercial availability, derived from renewable sources, and compatibility with biomolecules, making such substrates very attractive for its commercialization. The paper-based SERS sensors can be considered as an up-and-coming platform in the application of point-of-care (PoC) devices by combining the ultralow detection limit, non-destructive analysis, and fingerprinting identification to the demand of rapid detection, real-time measurements, sensitive analysis, and portability of such devices.[42,125–127]

A strategy to improve the performance of paper-based SERS substrates is the modification of the paper surface from hydrophilic into hydrophobic.[111,128,129] The hydrophobic modification of the paper surface is a key step in the production of the paper-based SERS substrates since it allows the local concentration of analyte on the plasmonic sensing region. Moreover, it can increase the number of hot spots by the same concentration effect. For instance, Lee et al.[130] proposed a hydrophobic paper-based SERS substrate using silver nanoparticles and an alkyl ketene dimer for the modification of the filter paper surface from hydrophilic to hydrophobic. After the surface modification of the paper, an aqueous solution of silver nanoparticles was dropped onto the hydrophobic paper and dried at room temperature for 1 h. The hydrophobic modification decreased the wettability of the filter paper by increasing the contact angle to 114°. The hydrophobic paper surface prevented the spread and absorption of both silver nanoparticles and analytes aqueous solutions in the filter paper, leading to an approx. 5-fold increase of the SERS spectrum of 4-aminothiophenol.

The paper-based SERS substrate can be obtained by different methods, including *in-situ* growth of nanoparticles on paper,[131] vacuum filtration method,[127] immersion in nanoparticle colloid,[65,132] screen printing,[133] and drop-wise.[130] For instance, Lee et al.[134] reported the fabrication of a paper-based SERS substrate by the dip-coating method using a conventional filter paper and gold nanorods. For this, the

filter paper was used without pretreatment and a silicon substrate modified with poly(2-vinylpyridine) was used for comparison purposes. The paper-based SERS substrate presented higher efficiency for the detection of 1,4-benzenedithiol compared to the traditional silicon substrate, exhibiting a 250-fold increase of the Raman bands. According to the authors, the flexibility of the paper-based substrate is responsible for its greater performance since it allows its friction against the surface of a sample for better adherence of the analyte.

A new deposition method for the production of a paper-based SERS substrate was proposed by Polavarapu et al.[135], where they used a fountain pen filled with plasmonic nanoparticles inks to directly draw SERS arrays on the paper substrate. The proposed substrates achieved low LOD such as 10^{-12} mol L^{-1} of rhodamine 6G and 20 ppb of thiabendazole (approximately 10^{-7} mol L^{-1}) with a sample volume of 10 µL.

In 2008, the inkjet printing method was first applied for the fabrication of SERS substrates by using metallic nanoparticle ink.[136] Thereafter, White and collaborators explored the inkjet printing technique as a highlighted method in the production of paper-based SERS substrates.[128,137–139] Since then, the inkjet printing technique has been explored in the fabrication of SERS-active substrates.[42,140–142] The deposition method has the advantages of low-cost and simplicity by employing a common office printer to print a nanoparticle ink directly on paper, and the substrate can be designed in a simple software. Additionally, piezoelectric inkjet printers present the advantage concerning the mechanism of dropping the ink out the nozzle in the response of an electrical current. In contrast to thermal inkjet printers, it allows low manufacturing temperature, preventing possible destabilization of the colloidal suspension.

In this chapter, we report the fabrication of a hydrophobic paper-based SERS substrate with enhanced SERS capabilities by the inkjet printing method. In order to achieve that, we combined an effective and highly stable gold nanospheres (AuSph) ink with a hydrophobic paper based on surface-modified chromatographic paper. The SERS substrates were designed as circular spots with a diameter of ca. 1 mm and the printing was carried out on a desktop inkjet printer. The SERS performance, using crystal violet as the probe molecule, demonstrated great reproducibility from spot-to-spot between different prints and high sensitivity of the

substrate. Finally, the inkjet-printed SERS substrate was applied for the detection and quantification of thiram, which is a dithiocarbamate fungicide used for the protection of fruits such as apple, peach, and strawberries in the field and also during transport and storage.[143] The fungicide is a neurotoxicant regulated by the Environmental Protection Agency (EPA) of the United States of America due to its neurotoxic effects such as lethargy and reduced motor activity.[143] Interestingly, a SERS analysis based on a recently developed digital protocol[68] allowed the quantification at ultralow concentrations while working at the SM-SERS regime.

3.1 EXPERIMENTAL SECTION

3.1.1 Reagents and Solutions

For the synthesis of AuSph, hydrogen tetrachloroaurate(III) trihydrate ($HAuCl_4.3H_2O$, ≥99.9 %), cetyltrimethylammonium bromide (CTAB, ≥99 %), trisodium citrate dihydrate (≥98 %), and L-ascorbic acid (≥99 %) were purchased from Sigma-Aldrich. For the paper surface modification, cellulose chromatographic paper (with a thickness of 0.18 mm and a linear flow rate of 130 mm/30 min, Whatman™), (2-dodecen-1-yl)-succinic anhydride (DDSA, 95 %), and 1-hexanol (98 %) were purchased from Sigma-Aldrich. For the AuSph ink, glycerol (≥99.5 %) and absolute ethanol (99.5 %) were purchased respectively from Sigma-Aldrich and Anidrol. Thiram (≥98.0 %), 4-nitrothiophenol (4-NBT, 80 %), and crystal violet (CV) were purchased from Sigma-Aldrich. The glassware was cleaned with *aqua regia* solution (3:1 v/v, $HCl:HNO_3$) and washed with water before the synthesis. In all the preparations, it was used deionized water (≥18.2 MΩ cm) from a Milli-Q water purification system (Millipore).

3.1.2 Gold Nanospheres Ink Synthesis

AuSph nanoparticles were synthesized via a seed-mediated growth method. First, ca. 16 nm AuSeed nanoparticles were synthesized according to the Turkevich method[92] in which Au^{3+} ions are reduced by sodium citrate. Briefly, 250 mL of 0.5 mmol L^{-1} $HAuCl_4$ was heated to boiling, and 12.5 mL 1 % (w/v) sodium citrate

was added to it under vigorous stirring. The heating and stirring were stopped after 17 min, and the colloid suspension was cooled to room temperature.

AuSph growth was performed following the procedure described by Rodriguéz-Fernández et al.[93] $HAuCl_4$ and L-ascorbic acid were added to a CTAB solution in a way to obtain the final concentration of 1.0, 2.0, and 15 mmol L^{-1}, respectively, followed by the fast addition of AuSeed (diameter of ca 15 nm and 0.01 mmol L^{-1} as the final concentration in terms of Au^0). The final volume of the synthesis was 400 mL. The reaction was allowed reacting at 35 °C for 1 h in a thermostatic bath. The AuSeed volume used for the AuSph growth is calculated by a theoretical equation that considers the desired diameter of AuSph, $HAuCl_4$, and AuSeed concentration (in terms of Au^0 concentration for AuSeed), and AuSeed diameter.[144,145] The theoretical equation is described in Appendix B.

The final AuSph colloid was washed and concentrated by centrifugation steps. Firstly, a concentration step was carried out at 1055 *g* for 40 min, and 95 % of supernatant was discarded. Next, two wash steps of the concentrated colloid were carried out at 775 *g* for 20 min, which 90 % of the supernatant was discarded in both steps, and the pellet was resuspended in the same volume of water and 0.77 mmol L^{-1} CTAB in the first and second steps, respectively. Finally, a concentration step was carried out at 775 *g* for 20 min, and approx. 80 % of the supernatant was discarded to achieve a final concentration of 46.15 or 174 mmol L^{-1} (in terms of Au^0), for preparing two different AuSph Inks.

The preparation of the AuSph Inks was performed based on a gold nanoparticles ink described by Hoppmann et al.[139] and the viscosity of ink originally manufactured by *Epson*® (which will be discussed later). For this, the AuSph colloid with a concentration of 46.15 mmol L^{-1} (in terms of Au^0), glycerol, and ethanol were mixed in the volume ratio of 65:25:10, respectively. The Au^0 concentration of the final AuSph ink was 30 mmol L^{-1}. The same procedure was performed with the AuSph colloid with the concentration of 174 mmol L^{-1} (in terms of Au^0), and the Au^0 concentration of the final AuSph ink was 113 mmol L^{-1}. The CTAB concentration was maintained at 0.5 mmol L^{-1} in both formulations.

The Au^0 concentration of AuSeed and AuSph Inks suspensions was estimated from the correlation between the extinction value at 400 nm in the VIS-NIR extinction spectra and the Au^0 concentration, as previously discussed in Chapter 2.[82,83]

3.1.3 Paper Surface Modification

For the surface modification of paper, the protocol was adapted from the experimental procedure described by Yu et al.[107] A sheet of chromatographic paper was immersed in solution 0.4 % (w/v) of DDSA in 1-hexanol for 5 min and cured in an oven at 160 °C for at least 6 min. The procedure was carried out between 1 and 5 times for different papers to optimize the surface modification process.

3.1.4 Fabrication of the Inkjet-printed *SERS* Substrate

The printing of AuSph Ink on the surface-modified paper was performed by an Epson Eco Tank L220. The SERS substrate was defined as a circular spot with a diameter around 1 mm and the AuSph Ink was inkjet-printed with the best print quality provided by the printer software.

3.1.5 Characterization

VIS-NIR extinction spectra of AuSph colloid and AuSph Ink were recorded using a Cary 8453 (Agilent) spectrophotometer. UV-VIS-NIR extinction spectra were recorded with path lengths of 1, 5, or 10 mm. Diffuse reflectance VIS-NIR extinction spectrum of the inkjet-printed SERS substrate was recorded using a Shimadzu UV-2450 spectrophotometer.

Transmission electron microscopy (TEM) images were obtained using a JEOL JEM 1010 transmission electron microscope operating at 100 kV. To obtain TEM images, the sample was prepared by drop-drying the colloid on a holey carbon-coated Cu grid. Scanning electronic microscopy (SEM) images of inkjet-printed SERS substrates were obtained using a JEOL JSM-6700F FEG scanning electron microscope operating at 10.0 kV and in backscattered electron imaging mode. To obtain SEM images, the inkjet-printed substrates were prepared by coating them with a thin layer of carbon.

The surface-modified chromatographic paper was characterized by the contact angle (CA) using an optical tensiometer Theta L (Attention). The measurements were realized in triplicate, and for each sample, it was measured the CA of both sides of the drop (n=6).

The viscosity measurements were carried out on a HAAKE MARS III Rheometer, Thermo Fisher Scientific, equipped with a DG41 double gap geometry. The measurements of flow curves were obtained on controlled rate mode with a shear rate from 10 up to 300 s^{-1} at 25°C.

Raman and SERS measurements were conducted with a Renishaw inVia Reflex system. The spectrograph used a high-resolution grating (1800 or 1200 grooves cm^{-1}) with additional band-pass filter optics, a confocal microscope, and a 2D-CCD camera. Laser excitation was carried out at 633, 785, and 830 nm laser lines. For SERS measurements, stock solutions of 10^{-3} mol L^{-1} CV, 10^{-3} mol L^{-1} 4-NBT, and 10^{-2} mol L^{-1} thiram were prepared at deionized water, methanol, and acetone, respectively. The stock solutions of the molecules were appropriately diluted in deionized water before the SERS measurements. Cosmic ray removal, noise filter, baseline, and smooth treatments were carried out using the software WIRE 4.3 (Renishaw, UK). For the quantification of CV and thiram, the digital protocol developed by Brolo and collaborators[68] was applied. More details about the digital protocol will be discussed in the following sections.

3.2 Results and Discussion

3.2.1 AuSph Ink Characterization

The effectiveness synthesis of AuSeed and the growth of AuSph nanoparticles were previously characterized by TEM images and UV-VIS spectroscopy, as shown in Figure 3.1(a-f). The histograms of the diameter of the nanoparticles are shown in Figure B.1 (Appendix B). Note that the AuSph nanoparticles were identified as AuSph-30 and AuSph-113, where the numbers correspond to the AuSph Ink with the gold concentration of 30 and 113 mmol L^{-1} (in terms of Au^0), respectively.

Figure 3.1a shows a representative TEM image of the AuSeed which presents a highly homogeneous morphology and size, presenting an average diameter of 14.5 ± 1.3 nm (n=250) (Figure B.1a, Appendix B). The characteristic LSPR profile of spherical nanoparticles with a dipole mode LSPR localized at 518 nm is observed for AuSeed in Figure 3.1b. Figure 3.1c shows a representative TEM image of AuSph-

30 showing a relatively high size and shape homogeneity. According to the histogram (Figure B.1b, Appendix B), the nanoparticles present an average diameter of 67.1 ± 2.9 nm (n=250). Additionally, AuSph-30 shows a dipole mode LSPR at 540 nm, as shown in Figure 3.1d.

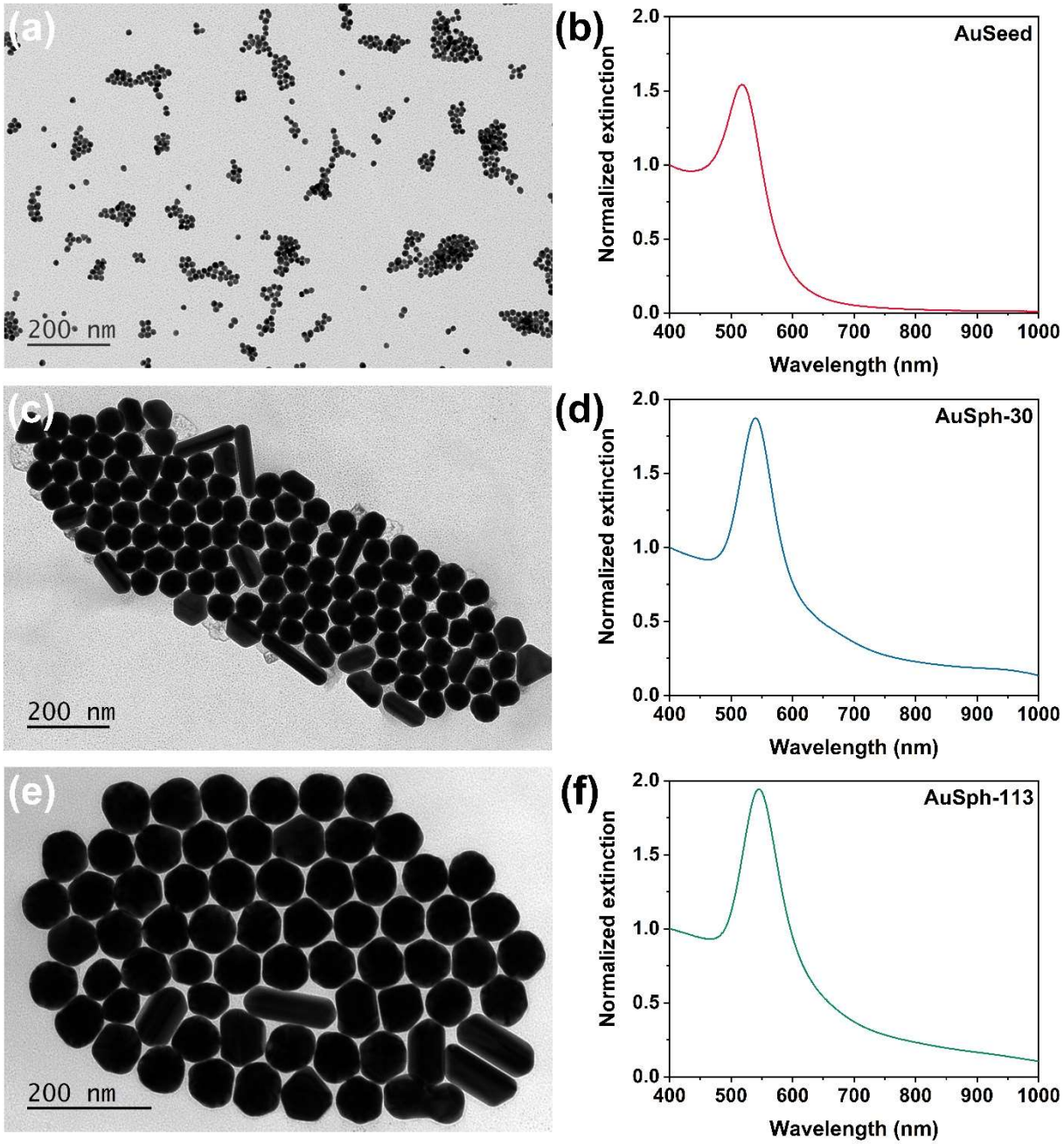

Figure 3.1. TEM image and VIS-NIR extinction spectra of (a,b) AuSeed, (c,d) AuSph-30, and (e,f) AuSph-113. The extinction spectra were normalized at 400 nm for comparison.

A representative TEM image of the second batch of AuSph is shown in Figure 3.1e. As observed for AuSph-30, the AuSph-113 also demonstrates a relatively

high size and shape homogeneity with ca. 24 % of the nanoparticles being nonspherical. The AuSph-113 nanoparticles presented an average diameter of 76.3 ± 3.5 nm (n=250) (Figure B.1c, Appendix B). Figure 3.1f shows the LSPR profile of the AuSph-113, presenting the dipole mode LSPR at 546 nm.

Interesting features are highlighted in the LSPR profiles of AuSeed and AuSph nanoparticles (Figures 3.1b, 3.1d, and 3.1f). Firstly, a red-shift in the LSPR band at 518 (AuSeed) to 540 nm (AuSph-30) or 546 nm (AuSph-113) resulted from the increase of the nanoparticle size during the growth synthesis. Comparing the LSPR bands intensities for AuSeed, AuSph-30, and AuSph-113, an increase in the band intensity is noted as the nanoparticle size increases. This characteristic occurs due to the change in the electric dipole when the nanoparticle size increases. It is also important to mention that the presence of nanorods and other nanoparticle morphologies formed during the growth process promotes a higher extinction above 600 nm for AuSph nanoparticles compared to AuSeed. The previous AuSph characterization is essential to verify the quality of nanoparticles obtained in the synthesis before the AuSph Ink preparation. Subsequently, the AuSph nanoparticles were washed, concentrated, and resuspended in a mixture of water:glycerol:ethanol for the production of the inks.

The ink composition was optimized regarding the optimal ink viscosity for the proper operation of the inkjet-printer. Thus, the viscosity of the original ink manufactured by *Epson*® (black ink, code 664) was measured and an average viscosity of 3.3 ± 0.1 cP was found (n=3). Based on this result, the viscosity of mixtures with different proportions of deionized water, glycerol, and ethanol was evaluated. The composition with 65 % deionized water, 25 % glycerol, and 10 % ethanol resulted in the viscosity value of 3.1 ± 0.1 cP (n=2), being the closest one to the original ink. This mixing ratio was chosen as the optimized ink composition, assuring appropriate viscosity to be used as ink while providing the stability of the nanoparticles.

The influence of changing the surrounding medium on the optical properties of AuSph was evaluated by the comparison of the VIS-NIR extinction spectra of AuSph-30 after synthesis and AuSph-30 ink, as shown in Figure 3.2. A small red-shift of the LSPR is observed when the medium surrounding the nanoparticles is changed from water (λ_{LSPR}= 538 nm) to the ink composition (λ_{LSPR}= 543 nm). This behavior is explained by the increase of the dielectric constant of the medium surrounding the

nanoparticles from 1.77 (water[7]) to 1.91 (ink composition without nanoparticles). The dielectric constant of the ink composition was estimated according to the empirical model based on the refractive index of ternary systems of water, ethanol, and glycerol developed by Moreira et al.[146]

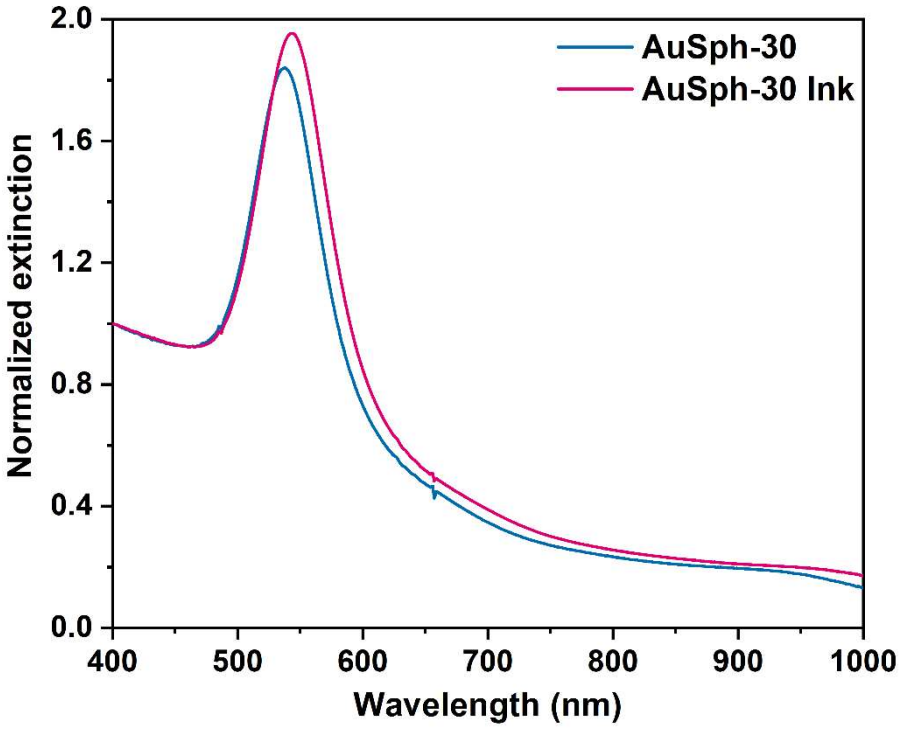

Figure 3.2. VIS-NIR extinction spectra of AuSph-30 colloid after synthesis and AuSph-30 Ink. The spectra were normalized at 400 nm for comparison.

The AuSph Inks were obtained with the final concentration of 30 and 113 mmol L^{-1} in terms of Au^0 (or 2.10^{15} and 5.10^{15} nanoparticles L^{-1}, respectively[§§]). Since the AuSph colloid after synthesis presents an Au^0 concentration of ca. 1 mmol L^{-1}, a 30 and 113-fold concentration is necessary for the production of the inks AuSph-30 and AuSph-113, respectively. In this way, the demand for large volumes of the colloidal suspensions required mixing different batches of reproducible AuSph synthesis.

The seed-mediated approach used for the synthesis of AuSph demonstrated high reproducibility between different synthesis batches for both AuSph-30 and AuSph-113. The high reproducibility of the AuSph synthesis is evidenced by

[§§] The nanoparticle concentration of the AuSph Inks was determined based on the average diameter of each nanoparticle. Detailed information is described in Appendix B.

the overlapping of the VIS-NIR extinction spectra of different colloidal suspension batches, as shown in Figure 3.3.

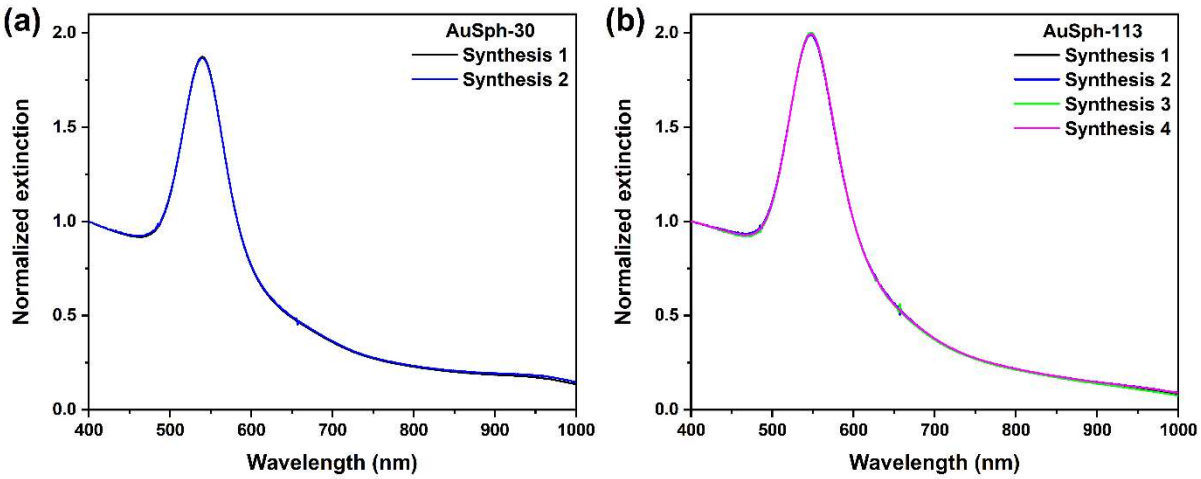

Figure 3.3. VIS-NIR extinction spectra of different batches of (a) AuSph-30 and (b) AuSph-113 synthesis. All spectra were normalized at 400 nm for comparison.

3.2.2 Paper Surface Modification

The chromatographic paper was chosen for the inkjet printing of SERS substrates since it presents a low fluorescence signal and background. Besides, it is composed of pure cellulose, being free from industrial addictive and possible contaminants to the SERS measurements.[128,147] The paper surface modification from hydrophilic to a hydrophobic surface is an essential step in the production of paper-based SERS substrates due to the concentration of analyte on the region of nanoparticles since the solution dries where it is dropped instead of spreading on paper.

The chromatography paper was modified with DDSA, a widely used sizing agent due to its capability of promoting a water resistance surface on paper.[148] The anhydride group of DDSA reacts with hydroxyl groups of cellulose by an esterification reaction. It enables the anchoring of the carbonic chains on the cellulose surface, which forms a hydrophobic barrier and reduces its wettability.[149] Figure 3.4 shows the functionalization reaction of the cellulose surface by DDSA (Figure 3.4a) and a schematic illustration of the hydrophobic barrier on the cellulose surface (Figure 3.4b).

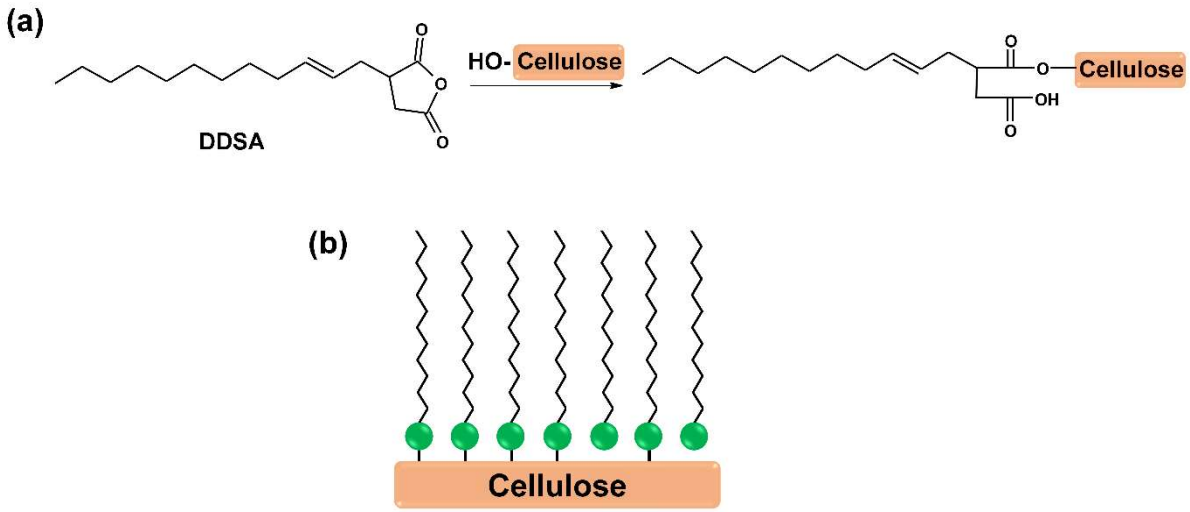

Figure 3.4. Scheme of (a) the reaction of (2-dodecen-1-yl) succinic anhydride (DDSA) with cellulose and (b) the hydrophobic barrier on cellulose surface promoted by the anchoring of the carbonic chains of DDSA.

The surface modification of the chromatography paper was evaluated by the CA measurement. The modification was studied as a function of the functionalization cycles from 1 up to 5, obtaining average CA values (n=6) of 122.1 ± 2.0; 127.1 ± 0.6; 129.9 ± 4.9 and 135.2 ± 0.8° when increasing the number of cycles, respectively. All the analyzed papers can be considered as hydrophobic, presenting CA values higher than 90°. Since no significant differences were observed between the CA values, the functionalization process consisting of two cycles was chosen as the standard procedure based on the smaller standard deviation associated with the shorter production time. Figure 3.5 shows photographs of CV solution (Figure 3.5a) and the CA measurement for surface-modified chromatographic paper after two functionalization cycles with a drop of water (Figure 3.5b).

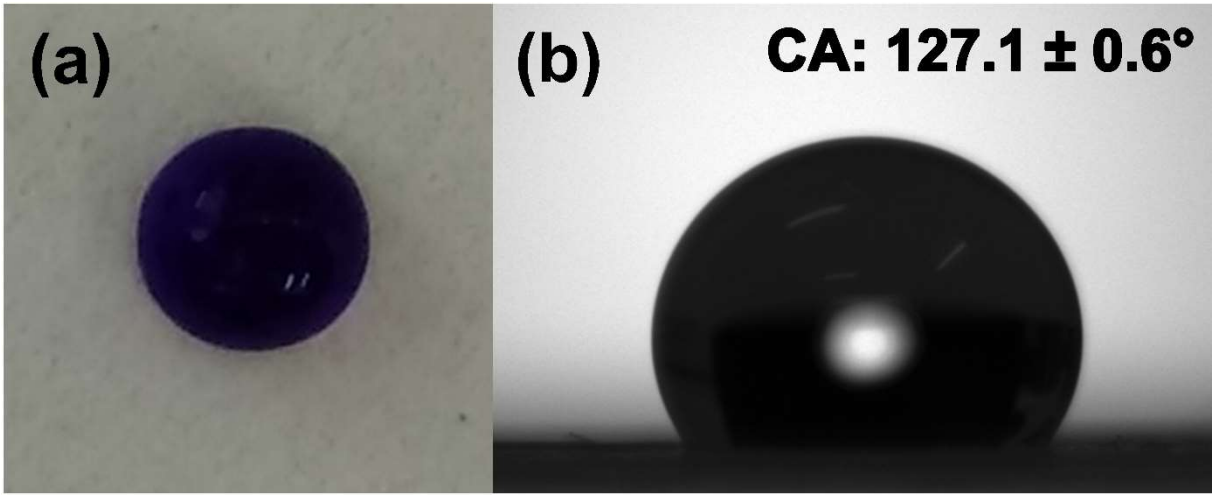

Figure 3.5. Surface-modified chromatographic paper after two cycles of the functionalization process. In (a) photograph of CV solution drop and (b) CA measurement with a drop of water.

3.2.3 Inkjet-printed *SERS* Substrate

3.2.3.1 Optimization of the Inkjet-printed Substrate

Once the AuSph inks were synthesized, the SERS substrates were inkjet-printed on the surface-modified chromatography paper. Firstly, the printing performance of the AuSph-30 Ink together with the printer was evaluated. Figure 3.6 (left panel) shows photographs of the *Colloid Chemistry Group* logo inkjet-printed on a conventional officer paper using the AuSph-30 Ink and 1 up to 4 printing cycles. Comparing to the *Colloid Chemistry Group* logo (right panel, Figure 3.6), the AuSph-30 Ink and the printer demonstrate high performance on the printing process, presenting high definition and an excellent surface coverage as well as high accuracy of the consecutive printing cycles.

Based on this previous characterization, the SERS substrates were optimized following the protocol of the number of printing cycles, which allowed modulating the AuSph concentration to achieve the highest SERS performance from AuSph inks in different concentrations. The optimization and characterization were performed for the inks of the AuSph-30 and AuSph-113, which is discussed in the following.

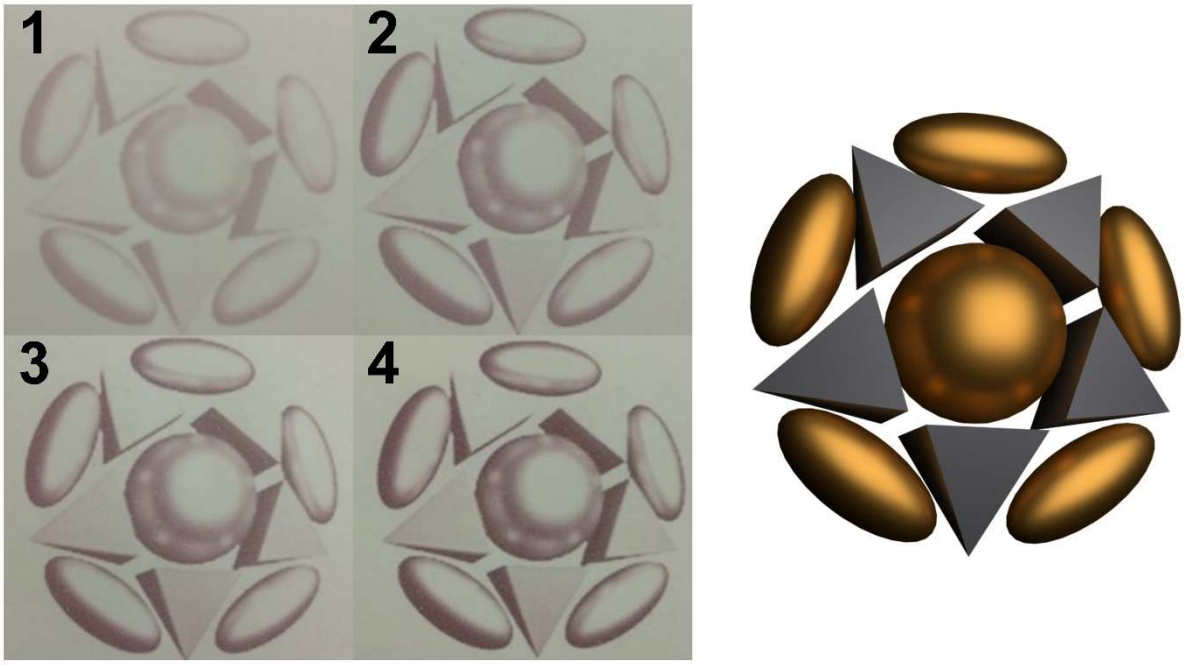

Figure 3.6. Photographs of the *Colloid Chemistry Group* logo inkjet-printed with AuSph-30 Ink and 1 up to 4 printing cycles on a conventional officer paper (left panel) and the logo image (right panel).

The inkjet-printed spots for SERS substrates designed were obtained with ca. 1 mm in diameter, with 1 up to 18 consecutive printing cycles using the AuSph-30 Ink (with a concentration of 30 mmol L^{-1} in terms of Au^0 or 2.10^{15} nanoparticles L^{-1}). Figure 3.7 shows the photographs and SEM images of the inkjet-printed spots. In Figure 3.7a, it should be noted by the naked eye a color evolution from gray to dark brown as the number of printing cycles increases, together with a great definition of spot design, high accuracy of consecutive printing processes, and homogeneous ink coverage on all spot area.

The surface coverage as well as the nanoparticle distribution on the substrates with the different number of printing cycles were characterized by SEM. Figure 3.7b shows representative SEM images at two different magnifications of spots fabricated with 2, 5, and 7 printing cycles, as indicated. An increase in the surface coverage by AuSph nanoparticles is observed as the number of printing cycles increases, as can be observed in Figure 3.7b (left panel). Moreover, the higher magnification SEM images (right panel, Figure 3.7b) suggest that increasing the number of printing cycles leads to regions with a higher density of nanoparticles, indicating the formation of larger nanoparticle aggregates.

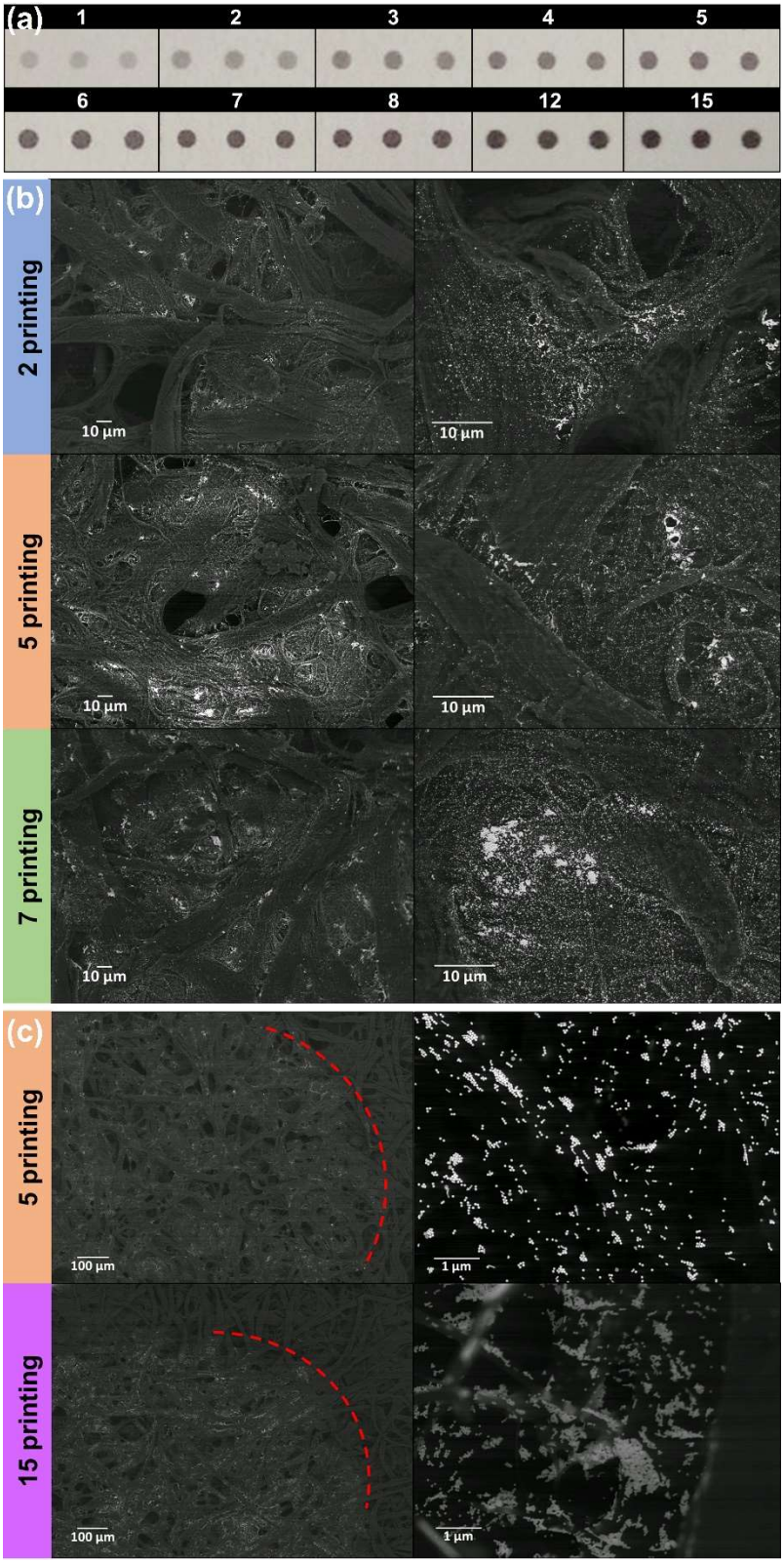

Figure 3.7. Optimization of the spots (ca. 1 mm of diameter) inkjet-printed with AuSph-30 Ink. (a) Photograph of spots printed from 1 up to 15 printing cycles. SEM images of spots obtained with consecutive printing cycles of (b) two, five, and seven, and (c) five and fifteen on the hydrophobic paper. In (c), the red dashed lines indicate the boundary of each spot.

Both findings are better noticed by comparing SEM images of inkjet-printed SERS substrates obtained with five and fifteen printing cycles shown in Figure 3.7c. The lower magnification SEM images (left panel, Figure 3.7c) evidence that the surface coverage increases together with the increase in the number of printing across all the spot area. Moreover, the well-defined boundary of the spots (highlighted with the red dashed line) validates the high accuracy of the inkjet-printing method.

Furthermore, the higher magnification SEM images (right panel, Figure 3.7c) corroborates the formation of larger nanoparticle aggregates as well as a higher number of the aggregates as the number of printing cycles increases. These characteristics of the substrates with a higher number of printing cycles are interesting since the higher number of hot spots as well as the formation of three-dimensional hot spots should improve the SERS activity of the substrate.

In order to confirm the best SERS performed of the inkjet-printed substrates with the different printing cycles, the substrates were evaluated using 4-NBT as a probe molecule. For this, 1 µL of an aqueous solution of 10^{-5} mol L^{-1} 4-NBT was dropped on each spot and allowed drying before the SERS measurement. Figure 3.8a presents the optical image and the corresponding SERS mappings of spots printed with 4 up to 18 printing cycles. The SERS mappings of spots obtained with different numbers of printing cycle (Figure 3.8a) are relatively uniform in intensity across the area of the printed spots. Figure 3.8b exhibits the SERS spectrum of 4-NBT on the spot inkjet-printed with five printing cycles, where the characteristic bands of 4-NBT are assigned to $\nu_{st}(CC_{ring})$ at 1572 cm^{-1}, $\nu_s(NO_2)$ at 1332 cm^{-1}, $\nu_{st}(CS)$ at 1079 cm^{-1}, and $\nu_{st}(CN)$ at 1109 cm^{-1}.[150,151] The SERS performance of the inkjet-printed substrates was evaluated based on the intensity of the most intense band of 4-NBT around 1334 cm^{-1}.

Figure 3.8c shows the average SERS intensity around 1334 cm^{-1} obtained from each SERS mapping in Figure 3.8a. The SERS intensity increases from the fourth to fifth printing cycle as the nanoparticle density increases in the substrate. However, the intensity decreases up to the seventh cycle and subsequently presents an upward trend up to the eighteenth cycle. The decrease in the SERS intensity from five to seven printing cycles is explained by the hydrophobicity loss observed by the naked eye for inkjet-printed spots obtained with more than five printing cycles. Interestingly, the upward trend of the SERS intensity for spots printed 7 up to 18 printing cycles indicates that, under the new condition of higher wettability, the SERS intensity increases as the

nanoparticle density on the paper increases with the number of printing cycles. The loss of hydrophobicity will be further discussed in the following.

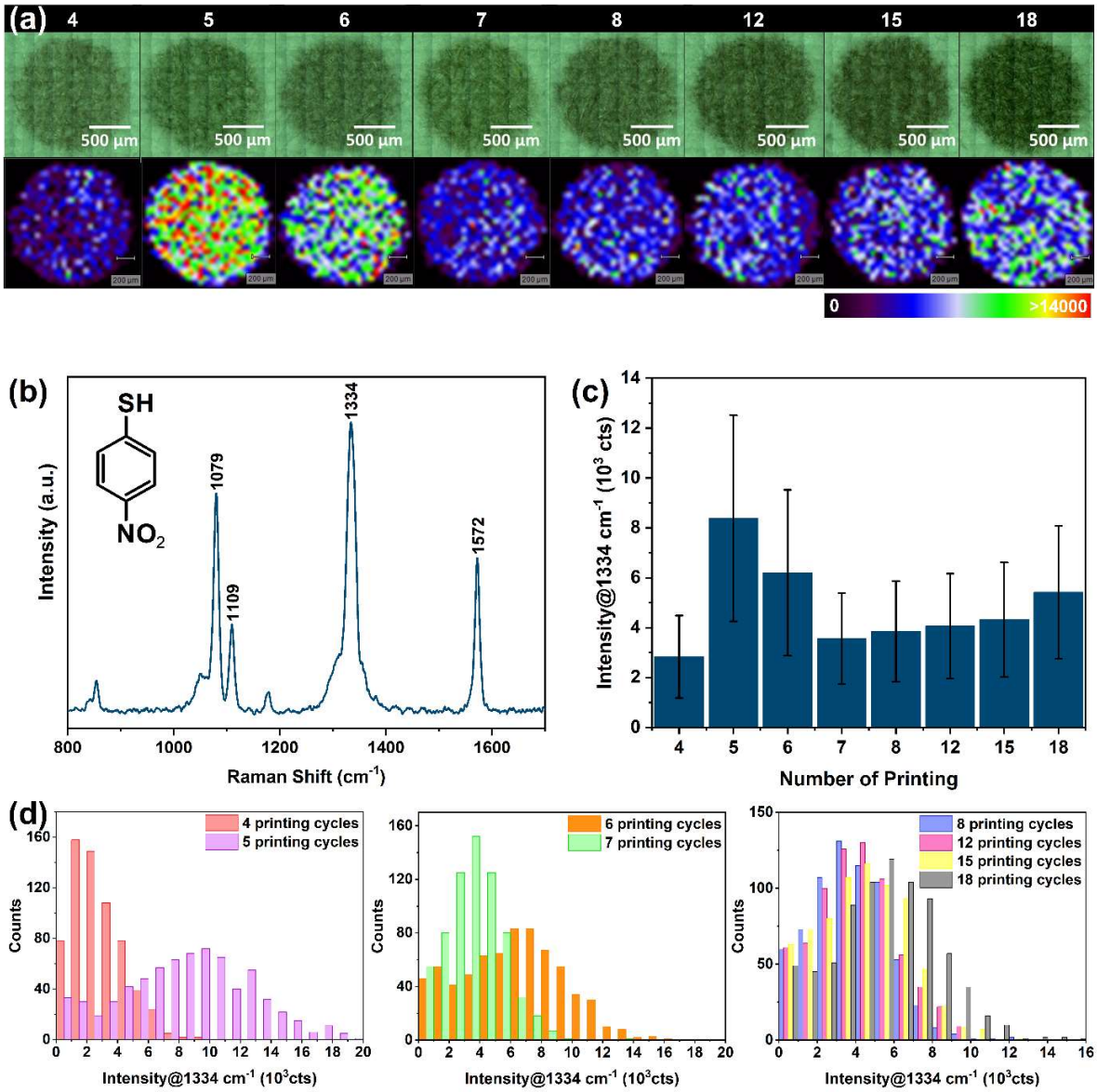

Figure 3.8. Optimization of spots (around 1 mm of diameter) printed 4 up to 18 printing cycles with AuSph-30 Ink. (a) Optical images of each spot and the corresponding SERS mapping recorded for 1 µL of 10^{-5} mol L^{-1} 4-NBT (intensity of the band around 1334 cm^{-1}). (b) SERS spectrum of 1 µL 4-NBT (10^{-5} mol L^{-1}) on the spot printed with 5 printing cycles. (c) Average and (d) histogram of SERS intensity (around 1334 cm^{-1}) derived from the SERS mappings in (a) (n>600, step 50 x 50 µm). All measurements were acquired with an excitation laser line of 785 nm and 20x objective. For the SERS mappings in (a) and SERS spectrum in (b), it was used, respectively, a laser power density of 46.43 kW cm^{-2} for 0.3 s with 1 accumulation and 0.16 kW cm^{-2} for 10 s with 3 accumulations.

The distribution of SERS intensity (around 1334 cm^{-1}) for each SERS mapping is shown in Figure 3.8d. The SERS intensity range observed for the SERS mappings corroborates the heterogeneous nanoparticle distribution (Figure 3.7), indicating the presence of different nanoparticle aggregates. The different profile of nanoparticle aggregates indicates the formation of hotter and colder hot spots, which results in the SERS intensity fluctuation. This feature is associate with the inherent characteristic of the substrate of being a complex three-dimensional matrix with cellulose fibers randomly arranged instead of being a flat surface.

When the number of printing cycles increases, a decrease of the relative standard deviation (RSD) from 58 up to 49 % is observed. It suggests an increase in the homogeneity of the nanoparticle distribution and the subsequent formation of more uniform hot spots. Although the SERS mappings present relatively high RSD values with a small fluctuation between them, the profile of the intensity distribution for each sample is significantly different from each other (Figure 3.8d). It indicates a different SERS performance for each substrate. Moreover, the RSD results suggest that the proposed SERS substrate is not appropriate for punctual analysis.

Finally, resuming the discussion on the loss of hydrophobicity issues, Figure 3.9 shows photographs of inkjet-printed spots obtained with different printing cycles after the deposition of water drops on their surface. It is noticed that spots inkjet-printed with 1 up to 4 printing cycles retain the water drops on the surface, indicating the stability of the hydrophobic barrier on the substrate surface. However, spots obtained with higher printing cycles were not able to retain the water drops on their surface, being observed a water penetration in the paper. The yellow arrows in Figure 3.9 highlight shadows around the spots resulted from the water penetration.

Since the 4-NBT solution drop spread out the inkjet-printed spot region by capillarity, some molecules could be carried out of the spot border, giving rise to a lower SERS intensity for inkjet-printed spots obtained with more than five printing cycles (Figure 3.8c). The increase of the wettability could be explained by the increase of glycerol content with the consecutive printing cycles, which allows the water penetration on the substrate due to the high affinity between the hydroxyl groups of glycerol and water.

This hypothesis was investigated to evaluate the influence of glycerol on the wettability of the paper. For this, drops of glycerol and ethanol were deposited in

different regions of the hydrophobic paper. The ethanol rapidly penetrated the paper sheet, while the penetration of the glycerol drop was slower. After the complete drying of both, a water drop was deposited in the same regions of the paper. The water drop remained on the paper surface where the ethanol drop was deposited, while it penetrated the area with glycerol. These results support the increase of the wettability as the glycerol content increases with the consecutive printing cycles.

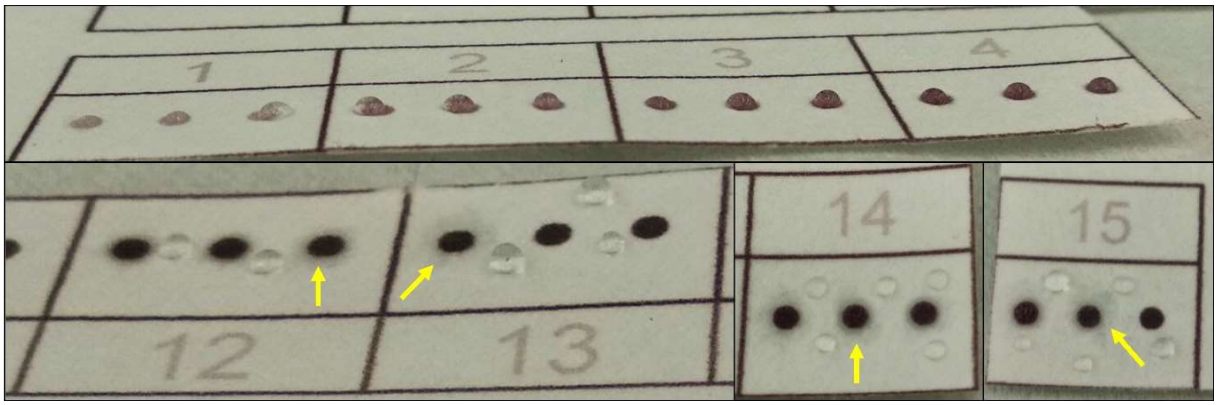

Figure 3.9. Photograph of water drops on spots (ca. 1 mm of diameter) printed from 1 up to 15 times with AuSph-30 Ink. Yellow arrows indicate shadows of water that penetrated the paper around the spots.

Based on the described results, inkjet-printed SERS substrates were fabricated with an AuSph Ink with higher nanoparticle concentration (113 mmol L^{-1} in terms of Au^0 or 5.10^{15} nanoparticles L^{-1}) in order to increase the nanoparticle content on the substrates without employing more than five printing cycles. In this way, the SERS performance of the substrates is improved while preventing the effect of the hydrophobicity loss of the spots.

Therefore, the inkjet-printed SERS substrates obtained with the AuSph-113 Ink were also optimized based on the number of printing cycles following the same protocol of the inkjet-printed SERS substrates using the AuSph-30 Ink. Figure 3.10a shows photographs of the inkjet-printed spots (ca. 1 mm in diameter) obtained from 2 up to 8 consecutive printing cycles. Besides the color evolution from gray to dark brown as the number of printing cycles increases, these spots present a darker color compared to the spots inkjet-printed with AuSph-30 Ink (Figure 3.7a), indicating a higher amount of nanoparticles.

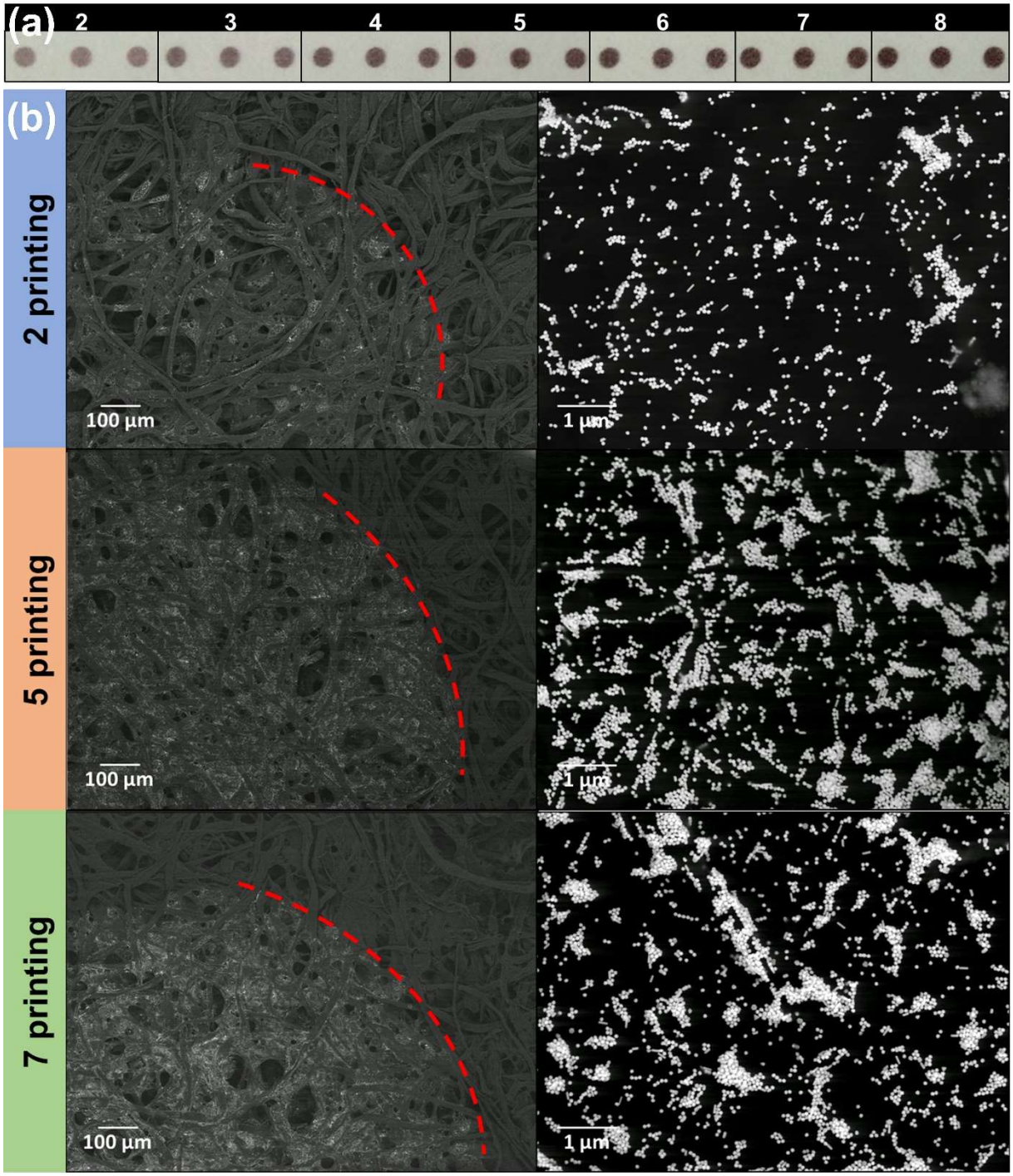

Figure 3.10. Optimization of the spots (ca. 1 mm of diameter) inkjet-printed with AuSph-113 Ink. (a) Photograph of spots inkjet-printed from 2 up to 8 printing cycles. (b) SEM images of spots inkjet-printed 2, 5, and 7 times on the hydrophobic paper. In (b0, the red dashed lines indicate the boundary of each spot.

The surface coverage and the nanoparticle distribution of these substrates were also characterized by SEM. Figure 3.10b shows representative SEM images at two different magnifications of spots fabricated with 2, 5, and 7 printing cycles, as

indicated. The images at lower magnification (left panel, Figure 3.10b) shows the well-defined boundary of the spots (highlighted with the red dashed line), indicating that the high accuracy of the inkjet-printing method is maintained when using the AuSph-113 Ink, which has a higher nanoparticle concentration.

An increase in the surface coverage of the paper is evidenced with the increase of the number of printing cycles (Figure 3.10b, right panel) as well as when comparing to spots inkjet-printed with AuSph-30 Ink (Figure 3.7c, left panel). Furthermore, for two printing cycles, most of the nanoparticles are distributed in small aggregates together with some large nanoparticle aggregates. Meanwhile, the nanoparticle aggregates increase in size as well as in number when the number of printing cycles increases.

Subsequently, the SERS performance of the inkjet-printed paper with the different printing cycles was investigated using CV as the probe molecule. Thus, 1 µL of an aqueous solution of 10^{-7} mol L^{-1} CV was dropped on each spot and allowed drying before the SERS measurement. Figure 3.11a presents the optical images and the corresponding SERS mappings of different spots inkjet-printed with 2 up to 8 printing cycles. Figure 3.11b shows the SERS spectrum of CV recorded in the spot inkjet-printed with five printing cycles, and Figure 3.11c corresponds to the average SERS intensity around 1618 cm^{-1} of each SERS mapping in Figure 3.11a.

In Figure 3.11a, it is observed that the SERS mappings are relatively homogeneous in intensity over all the spot areas likewise observed for substrates inkjet-printed with AuSph-30 Ink (Figure 3.8a). Moreover, comparing the optical images of the inkjet-printed substrates obtained with AuSph-30 (Figure 3.8a) and AuSph-113 (Figure 3.11a) Inks, the higher amount of nanoparticles in the latter is evidenced by their darker color in addition to the comparison of the photographs of both substrates aforementioned (Figures 3.7a and 3.10a).

Figure 3.11b exhibits the SERS spectrum of CV recorded in the spot inkjet-printed with five printing cycles, where the characteristics signals of CV are observed and attributed to $\nu_{st}(C{=}C_{ring})$ (8a benzene mode) at 1618 and 1585 cm^{-1}; $\nu_{st}(C_{ring}N)$, $\delta_s(CH_3)$ and $\nu_{st}(CC)_{ring}$ (8b benzene mode) at 1540 cm^{-1}; δ_s(CH3),δ(CH), $\delta(CCC)_{ring}$ and ν_{st}(ø-N) at 1385 cm^{-1}; $\delta(CCC)_{ring}$, $\nu_{as}(CC_{center}C)$, δ(CH) and ν_{st}(ø-N) at 1365 cm^{-1}; and $\delta(CCC)_{breathing}$, $\nu_s(CC_{center}C)$, $\rho(CH_3)$ and $\delta(CC)_{ring}$ (9a benzene mode) at 1174 cm^{-1}.[152]

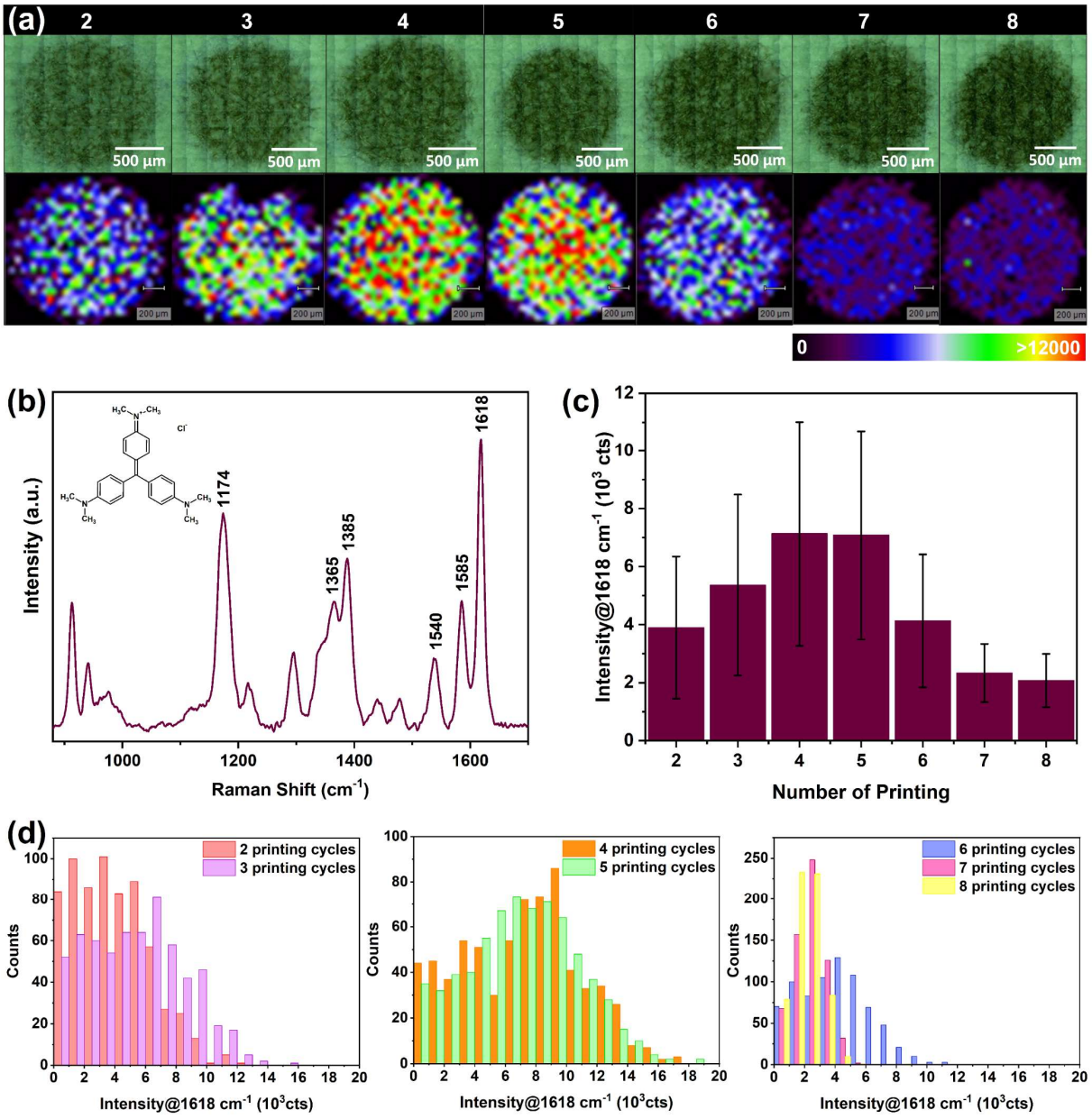

Figure 3.11. Optimization of spots (around 1 mm of diameter) printed 2 up to 8 printing cycles with AuSph-113 Ink. (a) Optical images of each spot and the corresponding SERS mapping recorded for 1 µL of 10^{-7} mol L^{-1} CV (intensity of the band around 1618 cm^{-1}). (b) SERS spectrum of 1 µL CV (10^{-7} mol L^{-1}) on the spot printed with 5 printing cycles. (c) Average and (d) histogram of SERS intensity (around 1618 cm^{-1}) derived from the SERS mappings in (a) (n>600, step 50 x 50 µm). All measurements were acquired with an excitation laser line of 785 nm and 20x objective. For the SERS mappings in (a) and SERS spectrum in (b), it was used, respectively, a laser power density of 46.43 kW cm^{-2} for 0.3 s with 1 accumulation and 0.16 kW cm^{-2} for 10 s with 3 accumulations.

Figure 3.11c shows the average SERS intensity around 1618 cm^{-1} with the number of printing cycles. The SERS intensity increases between the second and the fourth deposition cycle, it remains constant between the fourth and the fifth cycle, and it decreases between the fifth and the eighth cycle. A loss of the hydrophobicity was also observed for the spots obtained with more than five printing cycles, as observed for the spots inkjet-printed using the AuSph-30 Ink (Figure 3.9). The higher wettability caused by the increase in the glycerol content with the consecutive printing cycles can explain the sharp decrease of the SERS intensity of spots inkjet-printed with more than five printing cycles.

The hydrophobicity loss in the substrates inkjet-printed with AuSph-113 Ink was further investigated by CA measurements of water drops on spots obtained with a different number of printing cycles. For this, square substrates of ca. 1 x 1 cm were printed to ensure the interface between the drop of water (ca. 14 µL) and the inkjet-printed area of each spot. From 1 up to 5 printing cycles, the inkjet-printed spots presented CA values between 93.7 and 105.4°, that is, in all cases, the paper can be considered as hydrophobic but they did not present any tendency with the number of printing cycles. Substrates with higher printing cycles were not measured since a water penetration was observed after the deposition of the water drop.

Moreover, similar behavior has been previously reported for Au nanospheres on a paper-based substrate and explained in terms of hot spot deactivation as the electromagnetic enhancement decreases when the size of the aggregates increased.[41] Overall, it has been postulated that the combination of the hot-spot deactivation as the size of nanoparticle aggregates increases, together with the loss in hydrophobicity with the printing cycles, is responsible for the decrease of the SERS intensity after the fifth printing cycle.

The distribution of SERS intensity (around 1618 cm^{-1}) for each SERS mapping is shown in Figure 3.11d. The heterogeneous nanoparticle aggregates distribution (Figure 3.10b) reflects in the SERS intensity fluctuation observed for the SERS mappings, resulting in a large SERS intensity range and consequently relatively high RSD, as previously discussed. A significant decrease of RSD from 63 up to 44 % was observed for spots inkjet-printed with 2 up to 8 printing cycles, which suggests a higher homogeneity in the formation of hot spots when the number of printing cycles increases. Besides, it could also indicate that once the hot spot deactivation is a

prominent effect when the size of the nanoparticle aggregates increases, the heterogeneous hot spots give rise to more similar SERS enhancement. This hypothesis is supported by the similar intensity distribution observed for the pair of spots inkjet-printed with four and five (middle panel, Figure 3.11d) and for seven and eight printing cycles (right panel, Figure 3.11d).

For AuSph-30 and AuSph-113 Inks, spots inkjet-printed with five printing cycles presented the highest SERS intensity for the respective analyte. In this way, spots obtained with both AuSph inks were compared to evaluate the best SERS performance using the same analyte. Figure 3.12 shows the average SERS intensity of 1 µL 10^{-5} mol L^{-1} 4-NBT around 1334 cm^{-1} for spots obtained with both inks and five printing cycles inkjet-printed on different days.

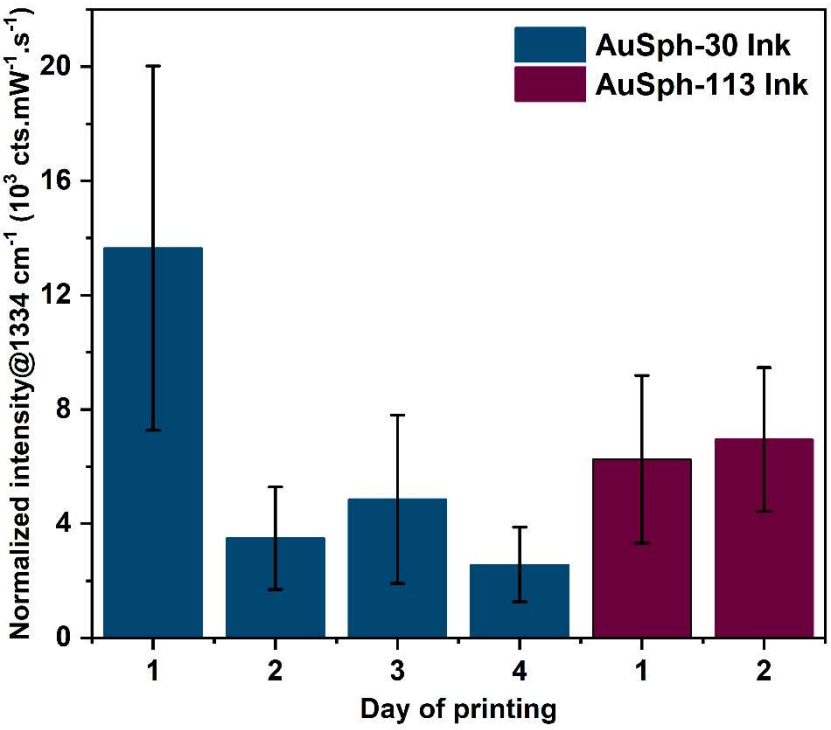

Figure 3.12. Average SERS intensity of 1 µL 4-NBT 10^{-5} mol L^{-1} (around 1334 cm^{-1}) on spots inkjet-printed with the inks AuSph-30 (blue bars) and AuSph-113 (purple bars) with five printing cycles on different days. The SERS mappings (n>400, step 50 x 50 µm) were recorded using a 785 nm laser line and 20x objective. All measurements were normalized based on the laser power, time exposure, and accumulation number.

Firstly, spots inkjet-printed with AuSph-30 Ink on four different days (blue bars, Figure 3.12) presented a significant decrease in the SERS intensity. On the

contrary, spots inkjet-printed with AuSph-113 Ink on two different days (purple bars, Figure 3.12) showed similar SERS intensity. These results seem to indicate higher reproducibility of spots obtained with AuSph-113 Ink. Moreover, considering only the three closest average SERS intensity of spots obtained with AuSph-30 Ink (days 2–4), it seems that the AuSph-113 Ink gives rise to substrates with higher SERS performance.

The spot inkjet-printed with AuSph-30 Ink is possibly less reproducible due to the lower surface coverage derived from the lower nanoparticle concentration of the ink. Once the surface coverage is improved as the nanoparticle concentration of the ink increases (AuSph-113 Ink), a more reproducible substrate should be obtained. Therefore, considering the results obtained up to here, the substrate inkjet-printed using the AuSph-113 Ink and five printing cycles was chosen as the optimized SERS substrate. Chosen the AuSph Ink more promising to SERS substrate fabrication, it follows to the evaluation of performance SERS and the final application of the optimized SERS substrate.

3.2.3.2 Influence of the paper surface modification on the Inkjet-printed SERS substrate performance

The influence of the paper surface modification on the SERS performance of the inkjet-printed SERS substrate after five printing cycles was evaluated by SERS using CV as a model analyte. Thus, 1 µL of 10^{-7} mol L^{-1} CV was dropped on spots inkjet-printed on chromatographic paper with and without surface modification. Figure 3.13 shows a 76-fold increase in the SERS intensity of the most intense band of CV (1618 cm^{-1}) when the hydrophobic chromatographic paper was used to fabricate the SERS sensing platform.

Therefore, this result demonstrates that the paper surface modification played a key role in the fabrication of the inkjet-printed SERS substrate by allowing the local concentration of analyte on the plasmonic sensor. Moreover, it agrees with the decrease of the SERS intensity that arose from the loss of hydrophobicity for inkjet-printed spots obtained with more than five printing cycles using both AuSph-30 and AuSph-113 Inks (Figures 3.8c and 3.11c).

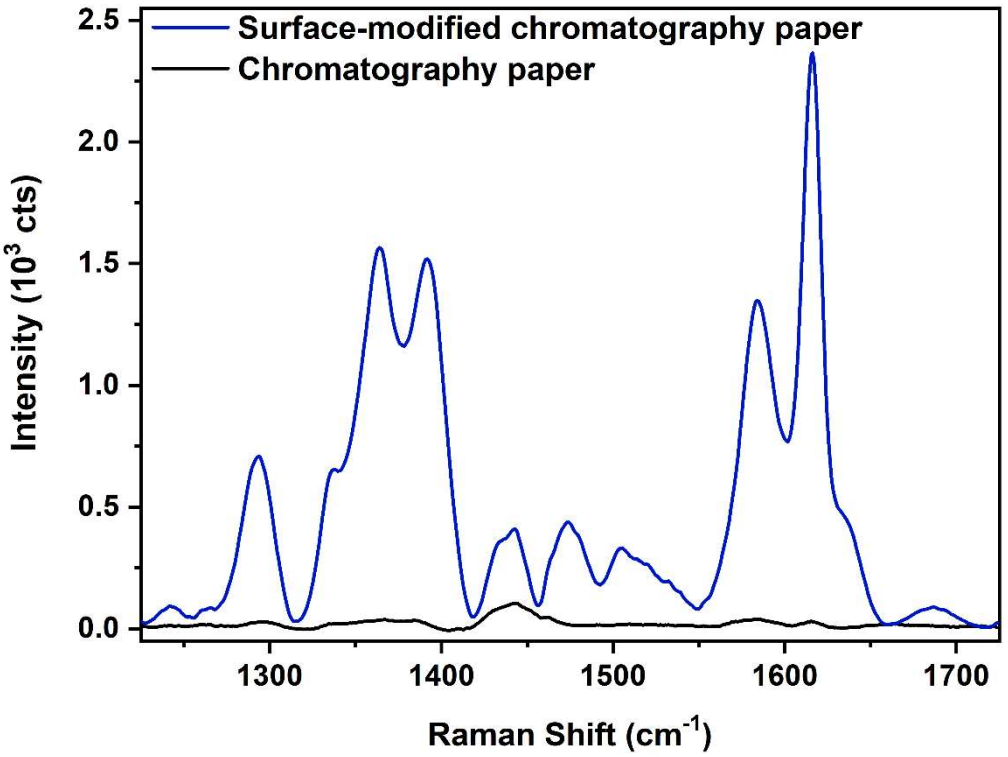

Figure 3.13. Average SERS spectra of 1 µL of 10^{-7} mol L^{-1} CV on the spot printed with AuSph-113 Ink and five printing cycles on hydrophilic chromatographic paper (black line) and hydrophobic chromatographic paper (blue line). SERS mappings (210 points each, step 50 x 50 µm) were recorded using a 785 nm laser line, 20x objective, a maximum power density of 175.79 kW cm^{-2}, an acquisition time of 1 s, and 1 accumulation. Both spectra are the average spectrum of three SERS mappings (630 points in total).

3.2.3.3 Influence of the excitation laser line on the SERS performance

The SERS performance of the inkjet-printed substrate was evaluated for different excitation laser lines to verify the most appropriate laser line to achieve the best SERS performance. This evaluation is essential since studies have already shown that, in contrast to systems with no hot spots, the SERS performance (far-field scattering properties) of systems mainly constituted by hot spots does not follow the LSPR properties (near-field scattering properties) of the substrate.

For instance, Litz et al. [153] demonstrated that a high intense extinction cross-section in the LSPR profile is associated with phase-coherent excitations. However, this condition does not necessarily lead to higher electromagnetic field enhancement. Instead, the strongest electromagnetic field enhancement is related to the highest polarization at the surface between neighboring nanoparticles. Kleinman et al.[154]

demonstrated an electromagnetic field enhancement when minimal scattering properties were observed in the LSPR profile of the substrates by experimental results and computational modeling. The authors also associated this behavior with the coupling of the dipole emitter (probe molecule near or at the neighbor of the nanoparticle junction) with plasmonic modes of the nanoparticles that are not observed at the far-field response (LSPR profile).

In this sense, a previous and straightforward characterization was taken from the diffuse reflectance VIS-NIR spectroscopy for the inkjet-printed SERS substrate. Figure 3.14 shows the comparison of the diffuse reflectance VIS-NIR extinction spectrum of the inkjet-printed SERS substrate and the extinction VIS-NIR spectrum of AuSph Ink. Firstly, differences between the LSPR profile of both samples is noticed mainly related to the extinction intensity of each spectrum. The increase in the extinction at lower energies for the AuSph-doped paper indicates the presence of nanoparticle aggregates as confirmed by SEM characterization (Figure 3.10b).

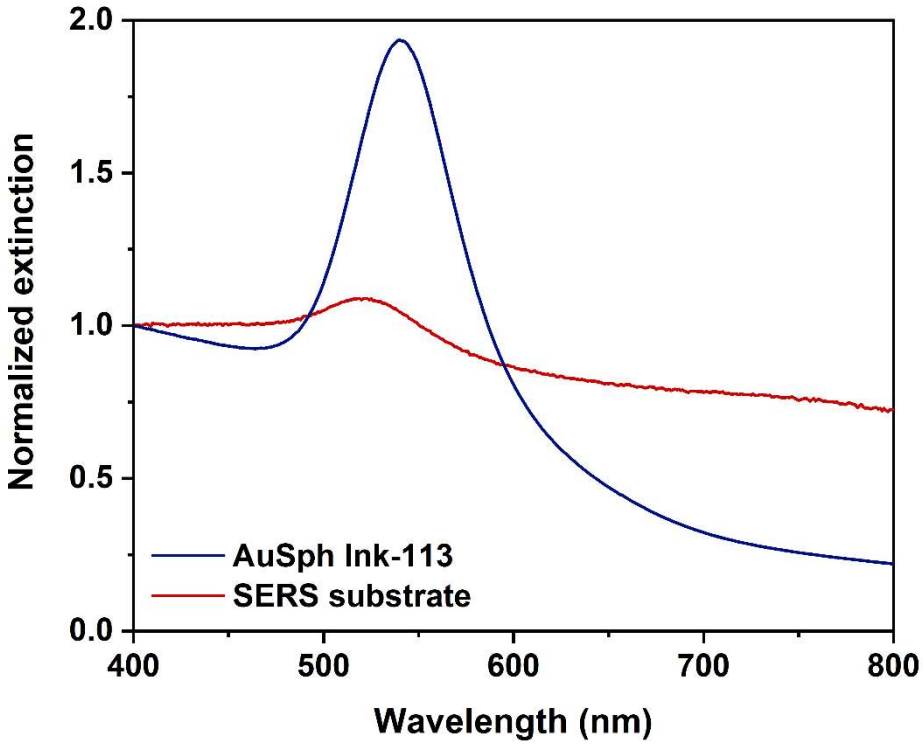

Figure 3.14. VIS-NIR extinction spectrum of AuSph-113 Ink (blue line) and diffuse reflectance VIS-NIR extinction spectrum of the SERS substrate inkjet-printed with AuSph-113 Ink and five printing cycles (red line). Both spectra are normalized at 400 nm for comparison.

This behavior is expected since it is known that the excitation frequency of hot spots is different from the excitation frequency of individual nanoparticles. Additionally, a blue-shift of the LSPR maximum from 540 to 521 nm is observed when the AuSph ink is inkjet-printed on the surface-modified chromatography paper due to the change of the medium surrounding the nanoparticles from the ink composition (ε_0= 1.91) to mostly air (ε_0= 1.00[7]).

According to the LSPR maximum of the SERS substrate, green laser lines (514 and 532 nm) should be in resonance for obtaining the maximum SERS enhancement. However, Rycenga et al.[155] already demonstrated that using these laser lines in SERS experiments with Au nanoparticles leads to a lower or even a non-response for SERS activity due to the plasmon damping derived from the interband transition of gold with the edge around 520 nm.

In this way, the SERS performance of the substrate was evaluated for the excitation laser lines of 633, 785, and 830 nm. For this, 4-NBT was chosen as the model analyte with a high binding affinity for metal surfaces, without absorption in the VIS-NIR region, and with a well-defined SERS spectrum, as shown in Figure 3.8b.[150,151] Thus, SERS mappings were recorded, selecting the most intense band around 1334 cm^{-1}, in the same inkjet-printed spot after the addition of 1 µL of 10^{-5} mol L^{-1} 4-NBT. The procedure was repeated for the three lasers line (633, 785, and 830 nm). Subsequently, the SERS enhancement factor (EF) for the inkjet-printed substrate was determined by comparing signals acquired on paper with and without inkjet-printed Au nanoparticles, according to Eq. (3.1):

$$EF = \frac{I_{SERS}/N_{surf}}{I_{Raman}/N_{vol}} \quad (3.1)$$

where I_{SERS} and I_{Raman} are the selected Raman band intensities of 4-NBT molecules chemisorbed on a SERS substrate and in a reference sample (surface-modified chromatographic paper), respectively. N_{surf} is the number of adsorbed molecules in the scattering volume for the SERS experiments, and N_{vol} is the number of molecules in the scattering volume of the Raman experiments.

Figure 3.15 shows the SERS mapping (Figure 3.15a) and the respective estimated enhancement factors (EF) for the different laser lines (Figure 3.15b). The

SERS signals were normalized based on the laser power, time exposure, and accumulation number applied in the SERS measurements.

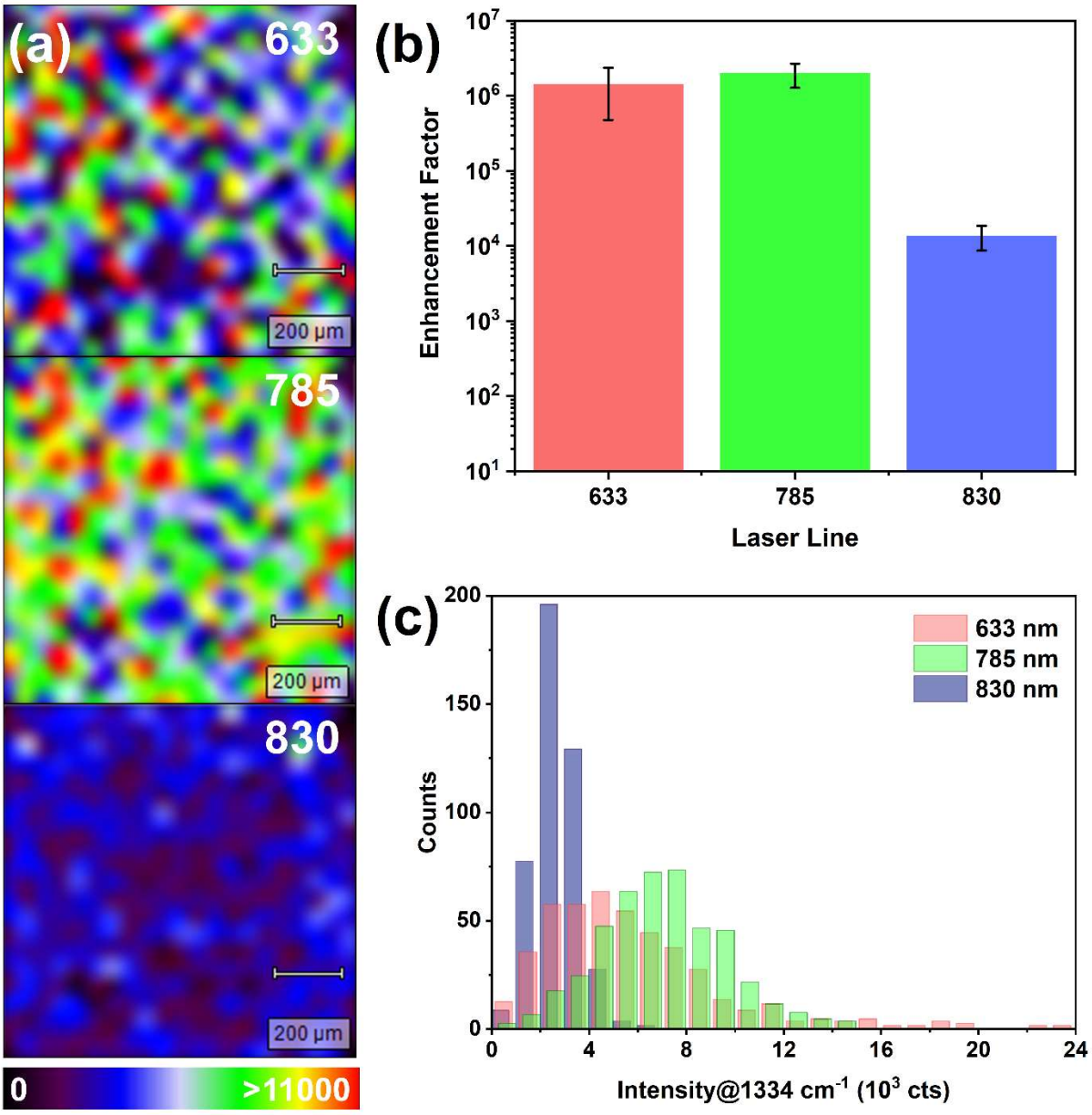

Figure 3.15. (a) SERS mapping of 1 µL NBT 10^{-5} mol L^{-1} (intensity of the band around 1334 cm^{-1}) on the SERS substrate inkjet-printed with AuSph-113 Ink after five printing cycles for the different laser lines. (b) Estimated EF of the SERS substrate for each laser line. (c) Histogram of the intensity of the band of 4-NBT around 1334 cm^{-1} extracted from (a). SERS mappings (441 pts, step 50 x 50 µm) were acquired with 633, 785, and 830 nm laser lines with a maximum power density of 3.65, 89.06, and 1.74 kW cm^{-2}, respectively, 20x objective, acquisition time 1 s and 2 accumulations. EF was estimated averaging SERS spectra extracted from SERS mappings.

The SERS mappings in Figure 3.15a show the highest and more homogeneous SERS signal on the analyzed area when using the 785 nm laser line. The use of the 830 nm laser line results in the lowest SERS activity of the substrate, while the 633 nm laser line results in an intermediate SERS activity. Accordingly, Figure 3.15b shows that the 633 and 785 nm laser lines present the highest EF of 1.4×10^6 and 2.0×10^6, respectively. It confirms that the 785 nm laser line was the most effective to achieve the highest SERS activity of the proposed substrate. It should be pointed out here, the similar EF for the 633 and 785 nm laser lines demonstrates the broadband enhancement of the SERS performance. Moreover, the EF data in conjunction with the diffuse reflectance VIS-NIR extinction spectrum of the SERS substrate (Figure 3.14) displays the divergence between the LSPR and enhancement properties of the SERS substrate previously discussed, indicating the presence of LSPR modes of active hot spots that are not evidenced in the LSPR profile.

It is interesting to notice the profile of the intensity distribution around 1334 cm^{-1} using the different lasers shown in Figure 3.15c. It is highlighted the significant difference between the range of the intensity distribution for each laser line. For the 830 nm laser line, the SERS intensities are limited to a narrow distribution in the range of 0–7,000 cts, with an average intensity of 2,725 cts. For the 633 nm laser line, the intensity distribution is larger, and the intensities higher than 22,000 cts demonstrates that despite the smaller average intensity (5,609 cts), this wavelength excites a few hotter hot spots (i.e., more effective) than the other laser lines. On the other hand, a smaller intensity distribution is observed in the range of 0–15,000 cts when the 785 nm laser line was used, which is associated with the highest average intensity of 6,945 cts.

The difference in the intensity distribution range evidence that each laser line excites different LSPR modes of nanoparticle aggregates (i.e., different hot spots), leading to different SERS enhancements of the substrate. These data agree with previous results that suggest the influence of different LSPR modes on divergent dispersions of the SERS signal when comparing the use of distinct laser lines.[55,156] Additionally, the behavior of the intensity distribution once again corroborates the presence of different nanoparticles aggregates with LSPR modes that are not observed in the LSPR profile of the SERS substrate.

3.2.3.4 Depth Profile Analysis

The inkjet-printed SERS substrate was also evaluated regarding its depth profile to evaluate the influence of the confocal microscope focus fluctuation on the SERS measurement. The fluctuation of the confocal microscope focus can be a result of the complex three-dimensional matrix of cellulose fibers that could lead to a shift of the distance between the sample and the objective lens, giving rise to a SERS intensity fluctuation.

For this, SERS intensity of 1 µL NBT 10^{-5} mol L^{-1} (at 1334 cm^{-1}) was measured as a function of the Z position on the SERS substrate inkjet-printed with AuSph-113 Ink and five printing cycles. The origin of the measurements was set as zero by visual focus and, then, SERS spectra were acquired in the Z position range from -200 up to 200 µm with a step size of 2 µm. Figure 3.16 shows the depth measurements of eight different positions across the spot area. The origin of the Z position (equal to zero) set for point 1 was maintained for all analyzed positions.

In general, the SERS intensity as a function of the Z position is an asymmetric curve due to the sample region that gives rise to the SERS signal. When the Z position presents negative values, the lens is focused inside the sample where high damping of the scattered light occurs due to the light dispersion inside the sample. Therefore, once the sample is moving away from the lens, the SERS signal rapidly increases as the light dispersion decreases. Subsequently, the SERS signal achieves the curve maximum, where the best focus position for the sample is reached. After this point, the SERS signal slowly decreases as the sample continues to move away from the lens since the scattered light is originated from the substrate surface. The decrease of the SERS signal continues until the long distance between the lens and the sample prevents the detection of the SERS signal.

Most of the depth profiles show small SERS intensity fluctuation around the maximum of the curve. Except for the profiles three and seven, the others presented a slight intensity fluctuation up to 500 counts from the maximum intensity in a range of at least 30 µm. In summary, considering the complex topology of the paper-based SERS substrate, the result is excellent since the distance range of 30 µm is large enough to prevent significant errors in the SERS analysis due to the visual focus issue.

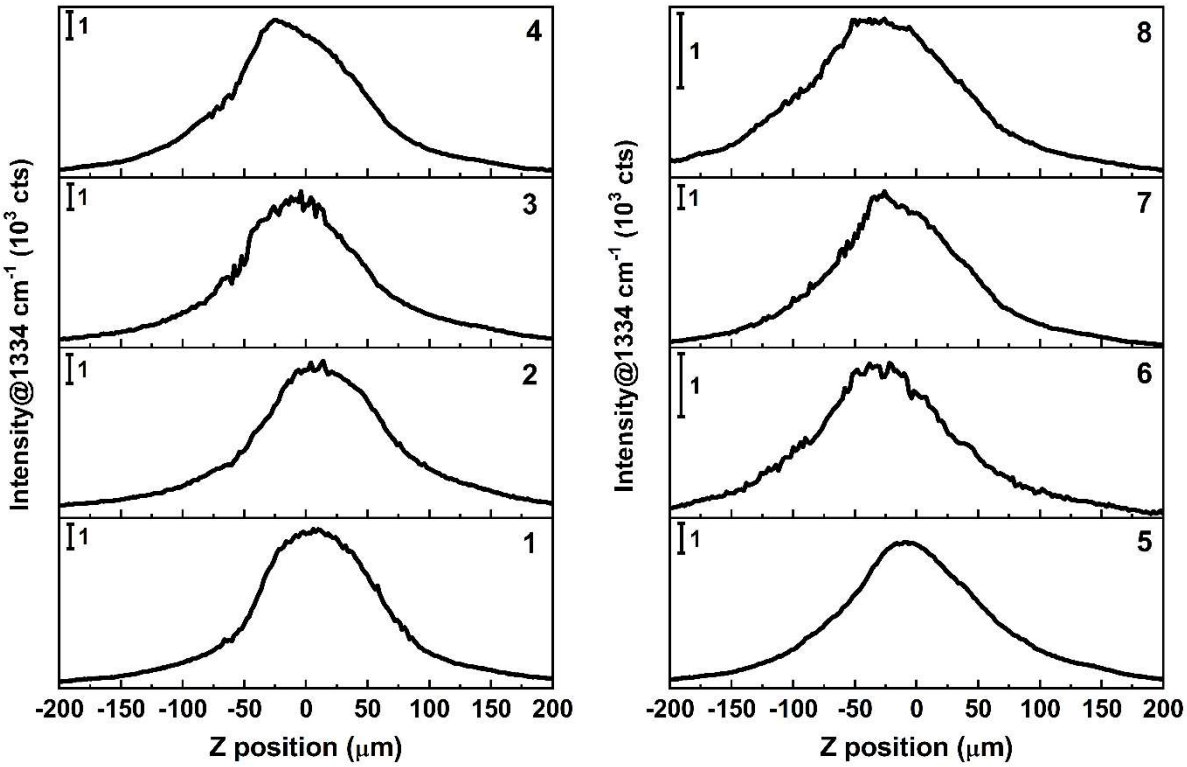

Figure 3.16. Depth profile of SERS intensity of 1 µL NBT 10^{-5} mol L^{-1} (at 1334 cm^{-1}) in eight points of the SERS substrate inkjet-printed with AuSph-113 Ink and five printing cycles. Measurements were acquired with 785 nm laser line, 20x objective, maximum power of 46.43 kW cm^{-2}, acquisition time 0.3 s, and 1 accumulation.

3.2.3.5 Reproducibility and Stability of the Inkjet-printed SERS substrate

Reproducibility is an important criterion to be considered when evaluating the performance of a chemical sensor. Herein, SERS substrates were evaluated from SERS mappings (210 points) measurements. For this, 10 different spots were inkjet-printed on the same surface-modified chromatographic paper sheet and treated with 1 µL of 10^{-7} mol L^{-1} CV. Figure 3.17a shows the average SERS spectra derived from the 10 different spots. The results indicate a great reproducibility of the SERS signal from spot-to-spot, presenting a small range of the intensity between the spectra.

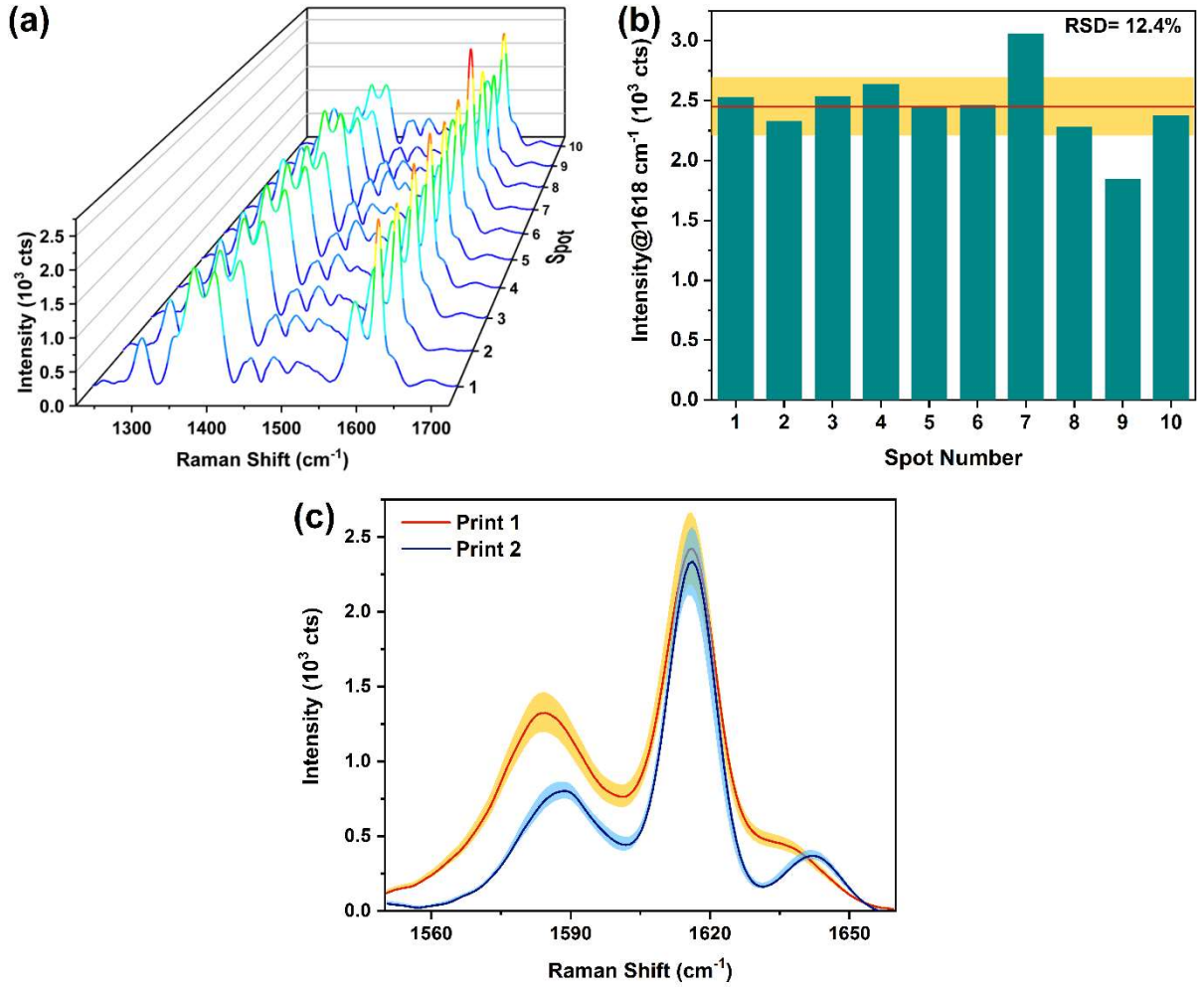

Figure 3.17. (a) Average SERS spectra and (b) average SERS intensity (1618 cm^{-1}) recorded for 1 µL of 10^{-7} mol L^{-1} CV measured on 10 different on the inkjet-printed SERS substrate after five printing cycles and ink-printed on the same hydrophobic chromatographic paper sheet. The region highlighted in orange represents a ± 10 % intensity variation concerning the average value (red line) for the 10 spots. (c) Average SERS spectra of 1 µL CV 10^{-7} mol L^{-1} measured on spots from different printings. "Print 1" is the average SERS spectrum of 10 spots from the reproducibility data in (a), where the orange region represents ± 10 % intensity variation with regards to the average value for the 10 spots. "Print 2" is the average SERS spectrum of CV in 3 spots from a different print, where the blue region is the respective standard deviation of the print. The SERS mappings (210 points, step 20 x 20 µm) were acquired with a 100x objective and 785 nm laser line with a maximum power density of 175.79 kW cm^{-2}, acquisition time 1 s, and 1 accumulation.

To better understanding the reproducibility from spot-to-spot, Figure 3.17b shows the average intensity of the SERS band around 1618 cm^{-1} for each spot. The intensity evaluation demonstrates a low RSD of 12.4 % between the 10 analyzed spots.

Moreover, the intensity data set was also evaluated considering a deviation range of ± 10%, as shown in Figure 3.17b. The results demonstrate that 80 % of the spots present the average intensity in the range of ± 10 %, validating the reproducibility of spot-to-spot results. In summary, this result indicates that the intensity of this SERS band is a reliable choice for the evaluation of the performance of the SERS substrate as well as for quantification purposes.

The reproducibility of the printing process was also analyzed by comparing spots derived from different printings. Figure 3.17c shows the average SERS spectra of 1 µL CV 10^{-7} mol L^{-1} measured on spots from two printing batches, where the average SERS spectra are derived from the reproducibility experiment (n=10) and another printing batch, which was performed in triplicate (n=3). The relatively low standard deviation between both measurements (2.8 %) seems to indicate a good batch-to-batch reproducibility of the printed SERS substrates

Interestingly, the reproducibility data evidence the use of the SERS mapping as a tool to overcome the limitation of the high RSD of the SERS measurements over the spot area resulted from the inherent heterogeneous distribution of nanoparticles in the three-dimensional hot spots substrate (Figure 3.11b). Therefore, the proposed inkjet-printed SERS substrate provides accurate and reproducible results when full SERS mappings are analyzed, although it is not appropriated for punctual analysis.

Besides the reproducibility, it is crucial to investigate the stability of the SERS substrates. The stability of the proposed sensor was evaluated based on two parameters: i) the stability of the ink and, ii) the SERS performance of the inkjet-printed spot with time. The stability of the AuSph-113 Ink was evaluated by VIS-NIR extinction spectra upon 365 days after synthesis, as shown in Figure 3.18a. For this evaluation, the AuSph-113 Ink was kept inside the printer or in a storage closet, protected from the sunlight. The result shows extremely high stability of the nanoparticles after their suspension in the ink composition, observing no changes in optical properties of the ink for at least 365 days after synthesis. This is an outstanding result considering the high ink concentration of 113 mmol L^{-1} in terms of Au^0 (or 5.10^{15} nanoparticles L^{-1}).

For the stability analysis of the inkjet-printed SERS substrate after five printing cycles, the substrates were stored in a storage closet under environmental conditions and protected from light. SERS maps of 1 µL of CV 10^{-7} mol L^{-1} were acquired over the storage time in triplicate (Figure 3.18b). The results indicate high

stability of the substrate up to 12 days of storage, presenting an average SERS signal in the range of ± 10 % of SERS intensity of the reproducibility data and satisfactory RSD up to 13.51 % between triplicate measurements. Although the inkjet-printed SERS substrate shows high stability for short storage time, the fabrication of SERS substrate from the inkjet-printed method is ensured by the high stability of the AuSph Ink, displaying one year of stability after synthesis.

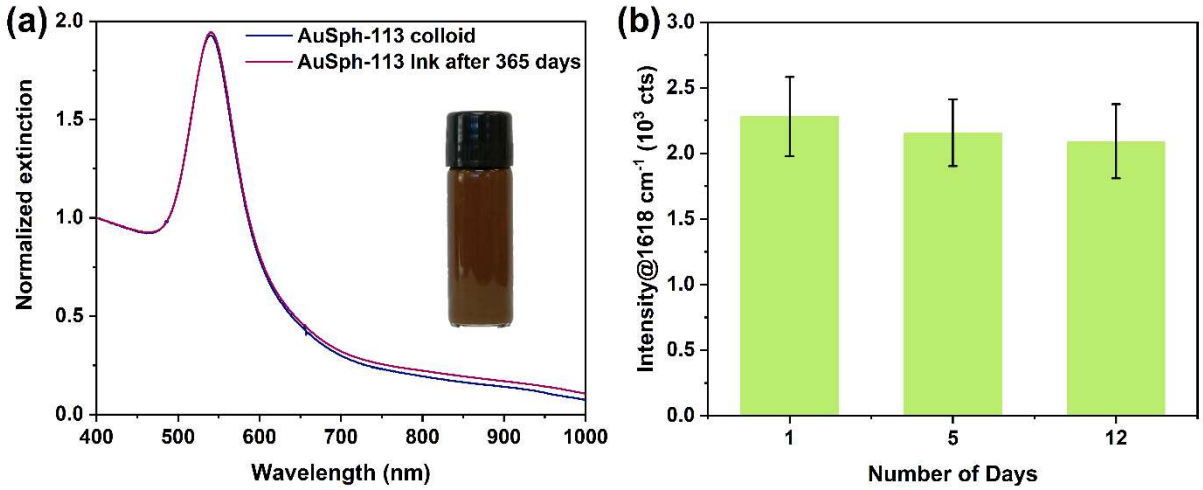

Figure 3.18. (a) VIS-NIR extinction spectra of AuSph-113 colloid after synthesis and AuSph-113 Ink after 365 days of storage. The AuSph-113 Ink was diluted in water to the acquisition of the VIS-NIR spectrum. The spectra in (a) were normalized at 400 nm for comparison. The inset in (a) is a photograph of the AuSph-113 Ink. (b) Stability of the inkjet-printed SERS substrate after five printing cycles over storage time ranging from 1 up to 12 days. Average of SERS intensity around 1618 cm^{-1} from three inkjet-printed spots treated with 1 µL CV 10^{-7} mol L^{-1} (data of 1 day is from the reproducibility analysis, Figure 3.17a). SERS mappings (210 points, step 20 x 20 µm) were acquired with a 100x objective and 785 nm laser line with a maximum power of 175.79 kW cm^{-2}, acquisition time 1 s, and 1 accumulation.

3.2.3.6 Sensitivity and Application of Inkjet-Printed SERS Substrate

First, the inkjet-printed SERS substrate was applied for the detection of CV. To carry out the SERS measurements, two droplets (1 µL each) of the CV solution were added to the spot and let them dry for both additions. For the SERS analysis, three SERS mappings were performed in 24 x 24 $µm^2$ area with 49 measurement points and step 4 x 4 µm, leading to a total of 147 data points each for each concentration.

After the spectral processing described in the experimental section, the digital protocol developed by Brolo and collaborators[68] was applied for the quantification at ultralow concentrations. The method consists of analyzing the relationship between the solution concentration with the number of SERS events, instead of the average SERS intensity, which is the most commonly employed methodology. Therefore, the digital protocol is more interesting than the conventional method since it considers that the SERS phenomenon relies on the probabilities of the molecules being adsorbed on an effective hot spot.

Fang et al.[60] have already demonstrated that less than 1 % of the molecules are located on very effective hot spots, being responsible for approximately 70 % of the overall SERS intensity. Meanwhile, 61 % of the molecules are located on hot spots less efficient, contributing only to 4 % of the overall SERS intensity. These results are particularly important at the SM-SERS regime where these statistics are associated with the lower surface coverage of the substrate by the molecules, leading to high SERS intensity fluctuation and making the sampling process more difficult.

In this way, the digital protocol is employed for the analysis at the SM-SERS regime and it considers that each SERS event is derived from a single molecule adsorbed on a hot spot. Taking this into consideration, it is important to assure the SM-SERS regime. Therefore, the distribution of the SERS intensity over the substrate is evaluated by plotting the frequency (or counts) *versus* the SERS intensity.

The SM-SERS regime is characterized by a long-tail distribution of the counts *vs* SERS intensity histogram, which presents a large number of SERS spectra with lower intensity than the average signal and a pronounced decrease to a small number of SERS spectra with higher intensity than the average.[61,68] The tailed distribution is a consequence of a smaller probability of the molecules to be adsorbed at the effective hot spots. Meanwhile, for higher concentrations than the SM-SERS regime, the molecules should be homogeneously distributed on the substrate surface. Therefore, the probability of observing a SERS signal is higher, leading to a spatial distribution of SERS efficiency similar to that from a random SERS substrate, that is, a Gaussian-like distribution.

For the analysis of CV, the histogram of the distribution of the SERS intensity around 1618 cm^{-1} was evaluated for concentrations ranging from 10^{-7}–10^{-11} mol L^{-1}, shown in Figure 3.19. The SM-SERS regime characterized by a long-tail

distribution of SERS intensity was evidenced for concentrations lower than 10^{-7} mol L^{-1}, while for this concentration a Gaussian-like distribution was observed. Accordingly, the digital protocol was applied for the concentrations of CV lower than 10^{-7} mol L^{-1}.

For the application of the digital protocol, the average noise level was estimated from three SERS mappings (49 points each, step 4 x 4μm) of the inkjet-printed SERS substrate without the addition of the analyte solution (named as *blank*). Then, a threshold of 3 times the standard deviation (99 % of the confidence level) of the average blank measurement was considered (n= 147). Intensities higher than the threshold were attributed as 1 (named as *digital counts*) while intensities equal or lower than the threshold were defined as zero (named as *zero counts*). Figure 3.20a shows the distribution of the SERS intensity around 1618 cm^{-1} for each measured spectrum for the CV concentrations under the SM-SERS regime (10^{-8}–10^{-11} mol L^{-1}).

In Figure 3.20a, a decrease in the number of digital counts (intensities higher than the threshold) together with an increase of the number of zero counts (intensities lower than the threshold) is observed when the CV concentration decreases. For instance, the SERS intensities are almost equally distributed as digital (47 %) and zero counts (53 %) for the CV concentration of 10^{-8} mol L^{-1}. In contrast, the SERS intensities are mostly found as zero counts (92 %) instead of digital counts (8 %) for the CV concentration of 10^{-11} mol L^{-1}.

Based on the data extracted from Figure 3.20a, digital SERS mappings were constructed correlating the digital and zero counts with the SERS mappings of each concentration under the SM-SERS regime, as presented in Figure 3.20b. Note that each digital SERS mapping shown in Figure 3.20b corresponds to a replicate of the SERS mappings for each CV concentration (n=49), presenting a total of three digital SERS mappings for each concentration (n=147). Additionally, white and black squares in the digital SERS mappings (Figure 3.20b) correspond to the zero (assigned as 0) and digital counts (assigned as 1), respectively.

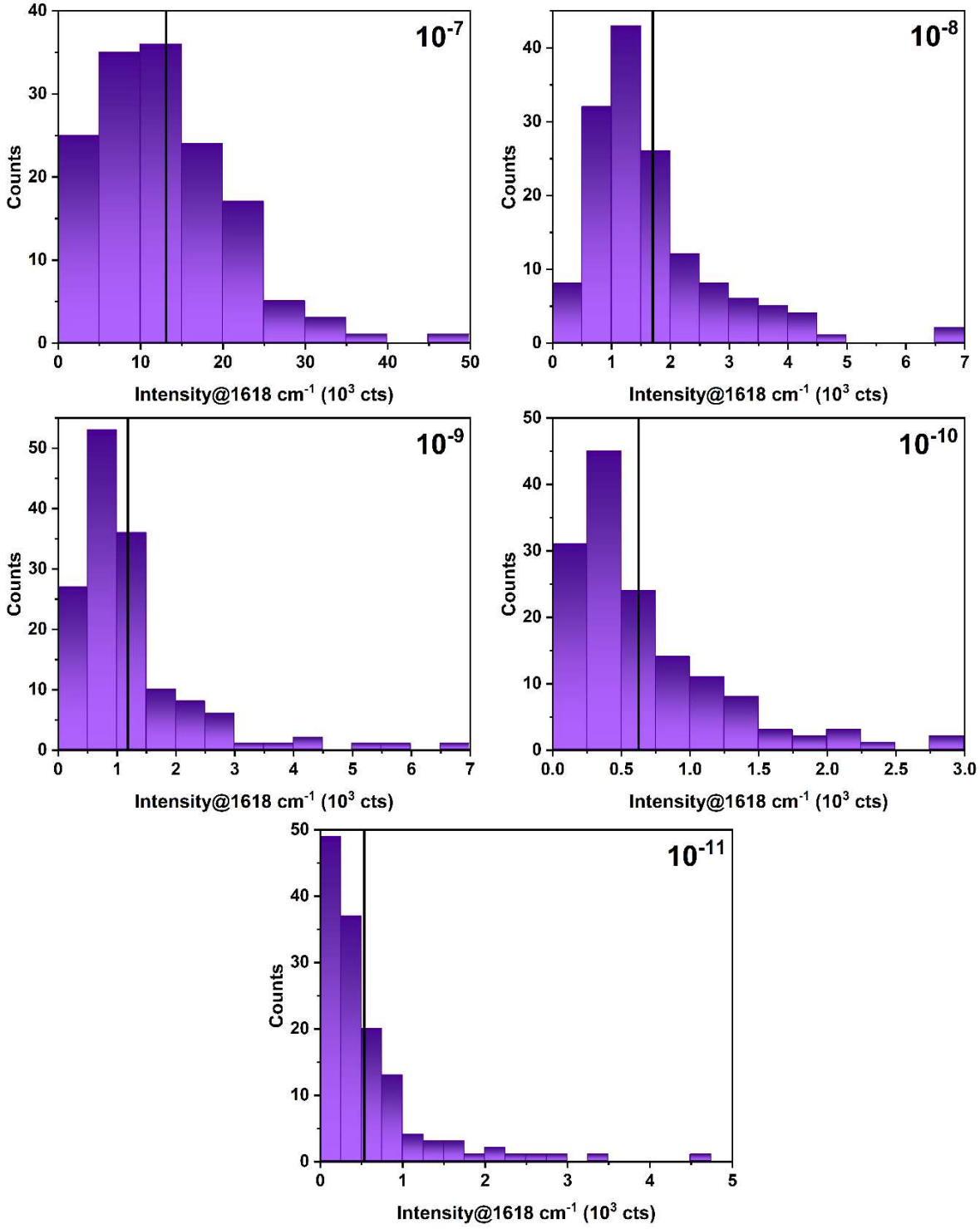

Figure 3.19. Histogram of the intensity of the band of CV around 1618 cm^{-1} for concentrations ranging from 10^{-7}–10^{-11} mol L^{-1} measured on inkjet-printed SERS substrates after five printing cycles (n=147, step 4 x 4 μm). The black line indicates the average intensity of the band. SERS mappings (49 points each and step 4 x 4 μm, with 147 points in total) were acquired for each concentration with a 100x objective and a 785 laser line with a maximum power density of 46.25 kW cm^{-2}, an acquisition time of 1.5 s, and 3 accumulation.

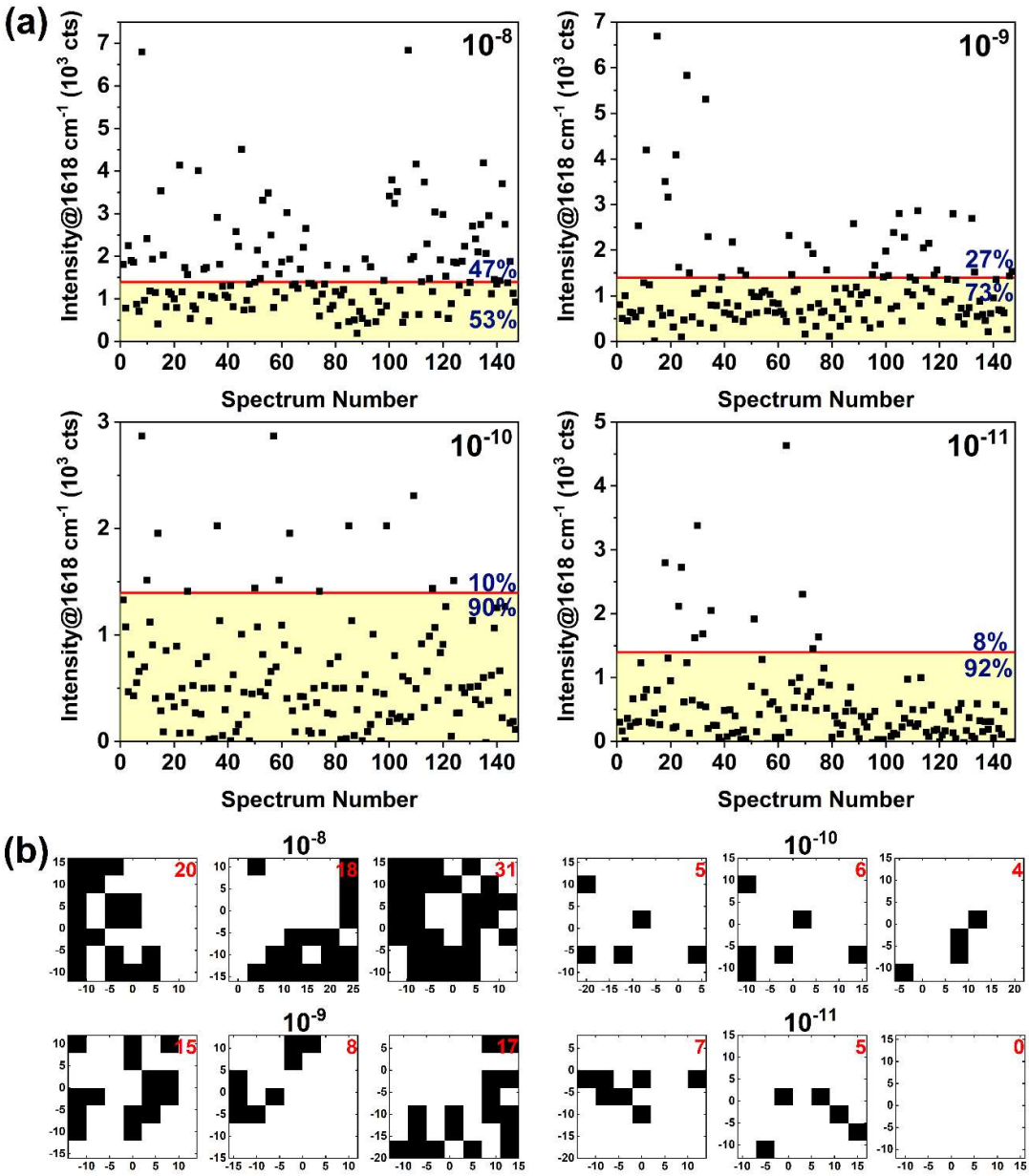

Figure 3.20. (a) Relationship between the intensity of the band of CV around 1618 cm^{-1} and each measurement point of the SERS mapping for the concentration under the SM-SERS regime (10^{-8}–10^{-11} mol L^{-1}). The red line indicates the threshold of 3 times the standard deviation of the blank measurement. The percentage values indicate the relative digital and zero counts respectively above (white zone) and below (yellow zone) the threshold. (b) Digital SERS mappings for the concentration of CV under the SM-SERS regime. The black and white squares correspond to the digital counts and zero counts, respectively. For the digital count analysis, three SERS mappings (49 points each and step 4 x 4 μm, with 147 points in total) were acquired for each concentration and for the blank measurement with a 100x objective and a 785 laser line with a maximum power density of 46.25 kW cm^{-2}, an acquisition time of 1.5 s, and 3 accumulation.

In general, the number of digital counts decreases for the replicates of the digital SERS mappings as the CV concentration decreases, as expected. Moreover, it is noticed that the digital counts are randomly distributed over the mapping area, mainly between the replicates for the lower concentrations. For instance, one replicate of the CV concentration of 10^{-11} mol L^{-1} shows zero digital counts, while the other two presents seven and five digital counts. This behavior exemplifies the low probability of the molecules to be adsorbed at the effective hot spots expected for the SM-SERS regime and the difficulty of the sampling process at low concentrations.

Representative SERS spectra considered as digital counts obtained for different CV concentrations under the SM-SERS regime are shown in Figure 3.21a. For comparison, the blank and a reference spectrum (positive event at CV concentration of 10^{-6} mol L^{-1}) are presented in Figure 3.21a. Firstly, the SERS band around 1618 cm^{-1} can be clearly distinguished from the blank spectrum for all the SERS spectra. Moreover, the SERS band is comparable with the reference spectrum, confirming that the observed SERS spectra under the SM-SERS regime arise from the probe molecule. It is worth to remark that although the blank spectrum (average noise level with n=147) shows a SERS band around 1618 cm^{-1}, it presents an extremely low average intensity of approx. 500 cts. Therefore, since a threshold of 3 times the standard deviation of the blank measurement was considered to attribute the SERS intensities as digital counts, it is guaranteed that noise signals were attributed as zero counts.

After attributing the SERS intensities as digital or zero counts (Figure 3.20), a digital calibration curve was obtained to correlate the total digital counts (i.e., the sum of all positive events) with each CV concentration under the SM-SERS regime. Therefore, a good linear correlation for the digital calibration curve was obtained in the range of 0.01–10 nmol L^{-1}, as shown in Figure 3.21b.

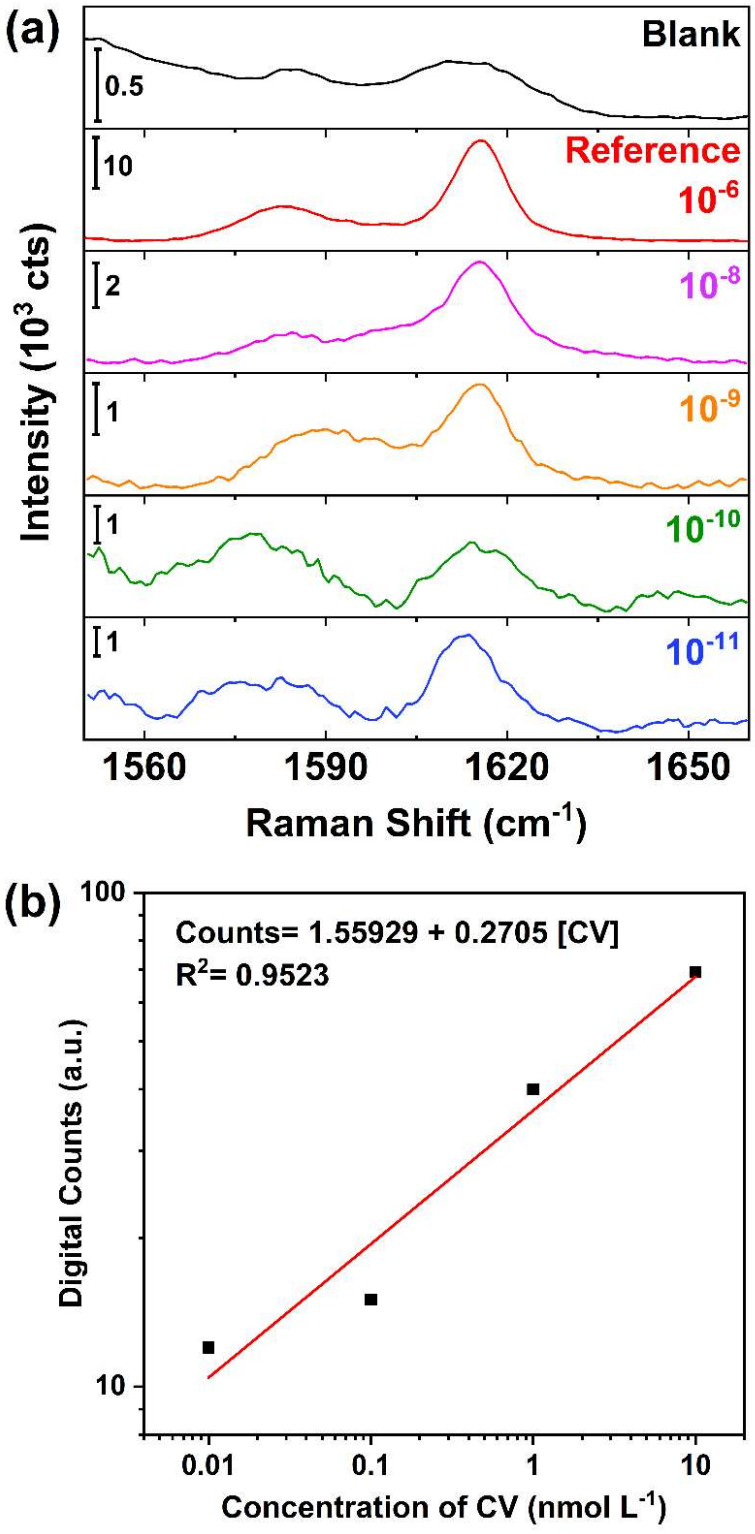

Figure 3.21. (a) Representative SERS spectra of positive events obtained for CV concentrations under the SM-SERS regime. The reference spectrum corresponds to a positive event measured at 10^{-6} mol L^{-1} (above the SM-SERS regime). The blank spectrum is the average of the three SERS mappings (49 points each, with 147 points in total). (b) Calibration curve of digital counts *versus* the CV concentration.

The applicability of the inkjet-printed SERS substrate was also tested towards the detection of the fungicide thiram. The sample preparation, SERS measurements, and methodology applied for the digital protocol analysis for thiram were carried out as previously described for CV. Figure 3.22 shows the SERS spectrum of 2 µL of 10^{-5} mol L^{-1} thiram dried on the SERS substrate, where the characteristics bands of thiram are observed and assigned as ν_{st}(CN), $\delta(CH_3)$, and $\rho(CH_3)$ at 1497 cm^{-1}, $\delta(CH_3)$ at 1440 cm^{-1}, $\delta(CH_3)$ and ν_{st}(CN) at 1374 cm^{-1}, ν_{st}(CN) and $\rho(CH_3)$ at 1141 cm^{-1}, and $\nu_{st}(CH_3N)$ and ν_{st}(C=S) at 939 cm^{-1}.[157,158] For thiram, the most intense SERS band around 1374 cm^{-1} was chosen for the subsequent SERS analysis.

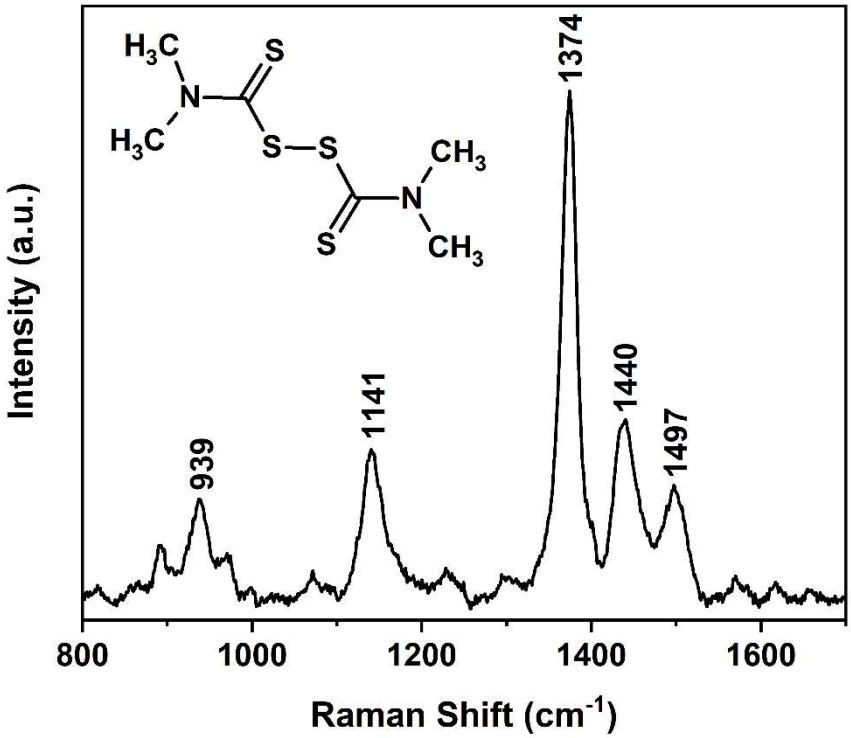

Figure 3.22. Representative SERS spectra of 2 µL of thiram 10^{-5} mol L^{-1} dried on the inkjet-printed SERS substrate. The SERS spectrum was acquired with a 100x objective and 785 laser line with a maximum power density of 21.89 kW cm^{-2}, an acquisition time of 10 s, and 3 accumulation.

The histograms of the SERS intensity around 1374 cm^{-1} for thiram concentration from 10^{-6}–10^{-12} mol L^{-1} are shown in Figure 3.23. It is observed a Gaussian-like distribution for 10^{-6} mol L^{-1} and a long-tailored distribution for the lower

concentrations. Therefore, the SM-SERS regime was defined for concentrations from 10^{-11}–10^{-7} mol L^{-1}, and the digital counts were estimated for this concentration range.

The distribution of the SERS intensity around 1374 cm^{-1} for each spectrum of the SERS mapping for the concentrations under the SM-SERS regime is shown in Figure 3.24a. As for CV, it is observed the clear trend of decreasing digital counts when the thiram concentration is decreased. For instance, the relative digital counts decrease from 86 to 5 % as the thiram concentration from 10^{-8} up to 10^{-11} mol L^{-1}, while the relative zero counts increase from 14 to 95 % in the same concentration range.

Therefore, the corresponding digital SERS mappings were constructed to correlate the digital and zero counts with the SERS mappings of each concentration under the SM-SERS regime, as shown in Figure 3.24b. Besides the decrease of the number of digital counts as the thiram concentration decreases, it is noticed the random distribution of the digital counts mainly of the thiram concentrations of 10^{-10} and 10^{-11} mol L^{-1}, as observed for CV.

Representative SERS spectra of different points considered as digital counts obtained for different thiram concentrations under the SM-SERS regime are shown in Figure 3.25a. Besides the main SERS band around 1374 cm^{-1}, another thiram band is also distinguished around 1497 cm^{-1}, agreeing with the reference SERS spectrum of thiram (positive event at thiram concentration of 10^{-5} mol L^{-1}). Nevertheless, the thiram signal is not so clear at 1440 cm^{-1} since it overlaps with a signal coming from the background, which is also observed in the blank spectrum (average noise level with n=147) (Figure 3.25a). The SERS band around 1444 cm^{-1} in the blank spectrum may be assigned to $\delta(CH_2, CH_3)$ of the CTAB molecules which stabilize the gold nanoparticles.[159,160]

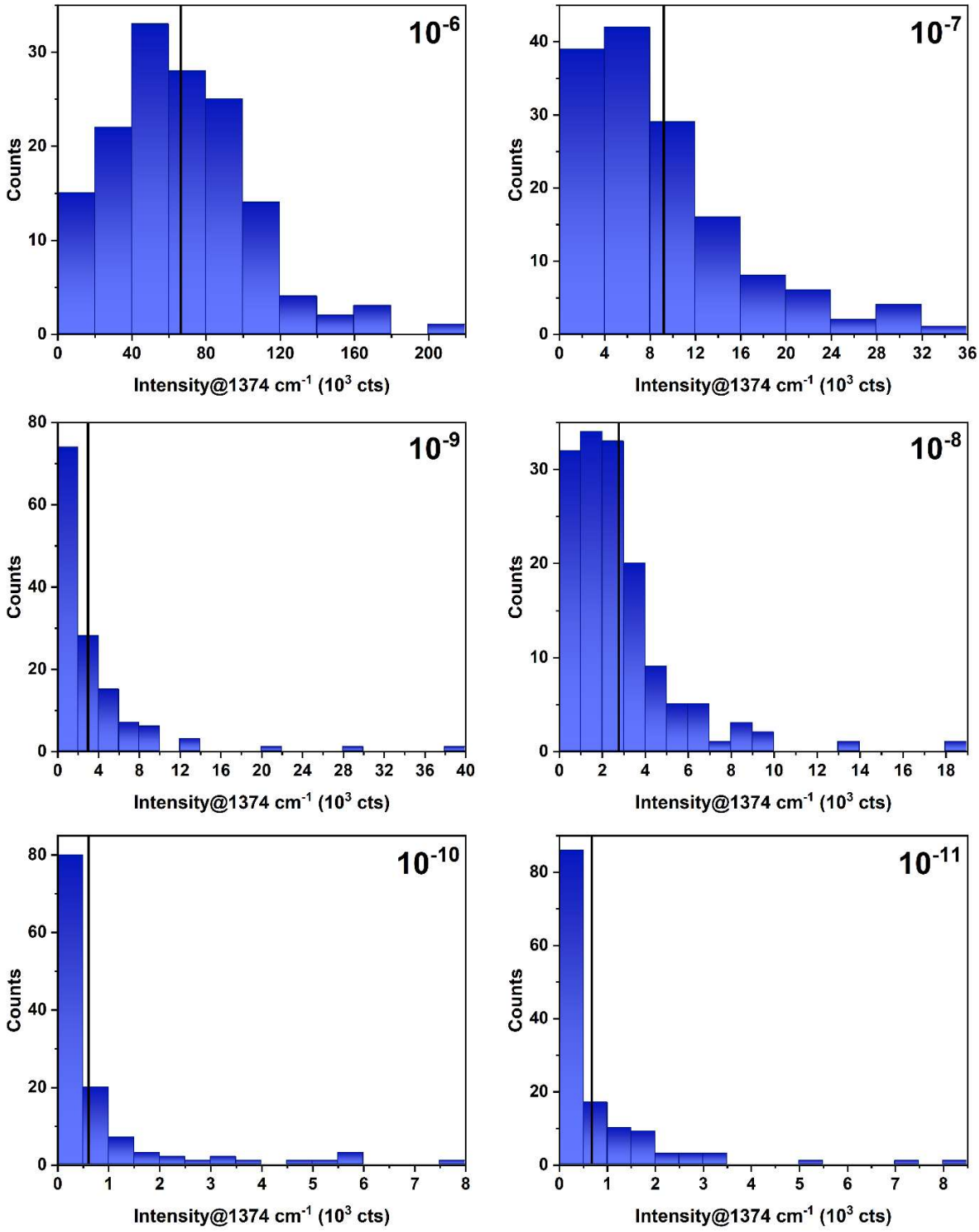

Figure 3.23. Histogram of the intensity of the band of thiram around 1374 cm^{-1} for concentrations ranging from 10^{-6}–10^{-11} mol L^{-1} measured on inkjet-printed SERS substrates after five printing cycles (n=147, step 4 x 4 μm). The black line indicates the average intensity of the band. SERS mappings (49 points each and step 4 x 4 μm, with 147 points in total) were acquired for each concentration with a 100x objective and 785 laser line with a maximum power density of 46.25 kW cm^{-2}, an acquisition time of 3.5 s and 3 accumulation.

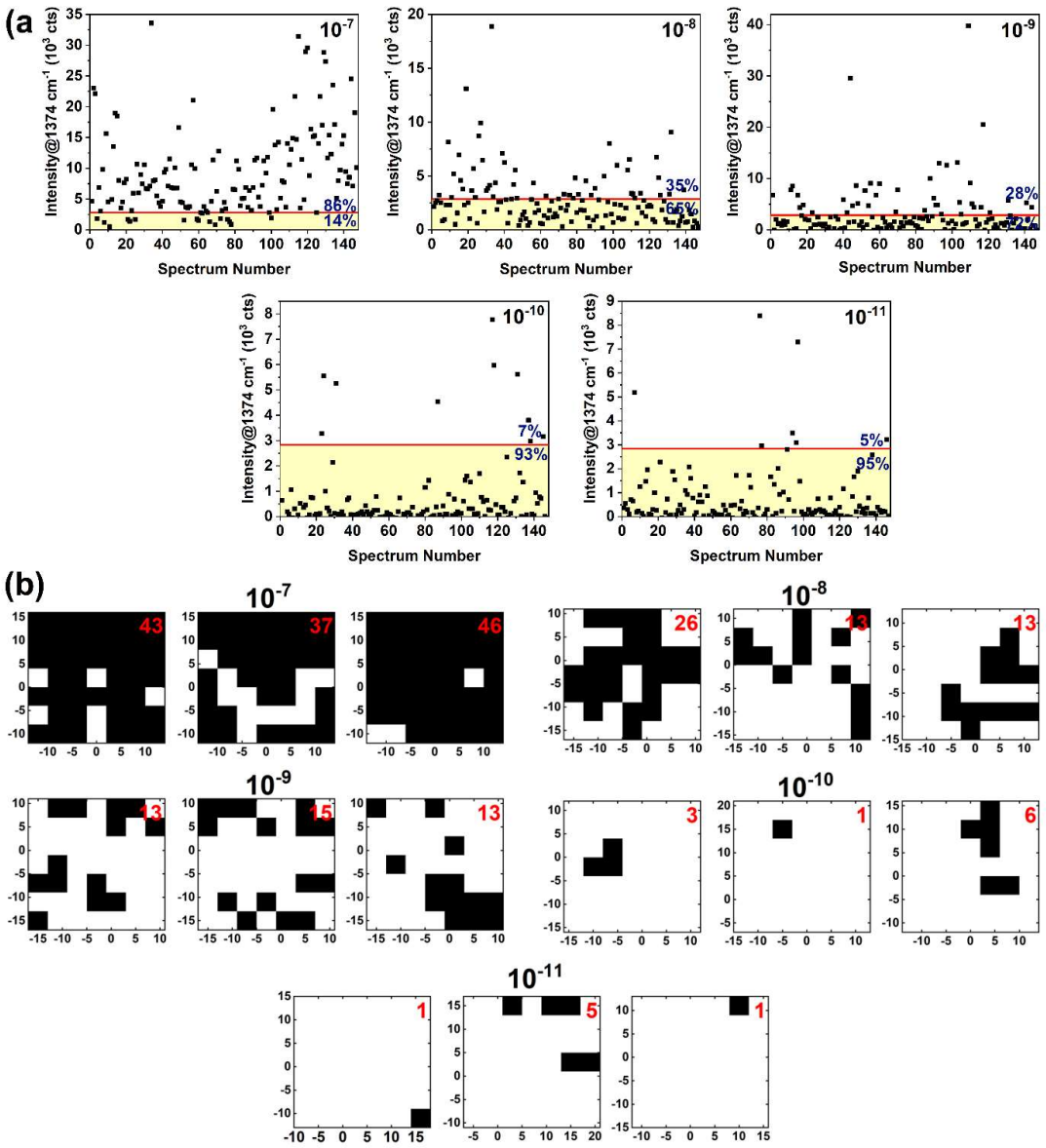

Figure 3.24. (a) Relationship between the intensity of the band of thiram around 1374 cm^{-1} and each measurement point of the SERS mapping for the concentration under the SM-SERS regime. The red line indicates the threshold of 3 times the standard deviation of the blank measurement. The percentage values indicate the relative digital and zero counts respectively above (white zone) and below (yellow zone) the threshold. (b) Digital SERS mappings for the concentration of thiram under the SM-SERS regime. The black and white squares correspond to the digital and zero counts, respectively. For the digital count analysis, three SERS mappings (49 points each and step 4 x 4 μm, with 147 points in total) were acquired for each concentration and for the blank measurement with a 100x objective and 785 laser line with a maximum power density of 46.25 kW cm^{-2}, an acquisition time of 3.5 s and 3 accumulation. The blank spectrum is the average of the three SERS mappings (49 points each and step 4 x 4 μm, with 147 points in total).

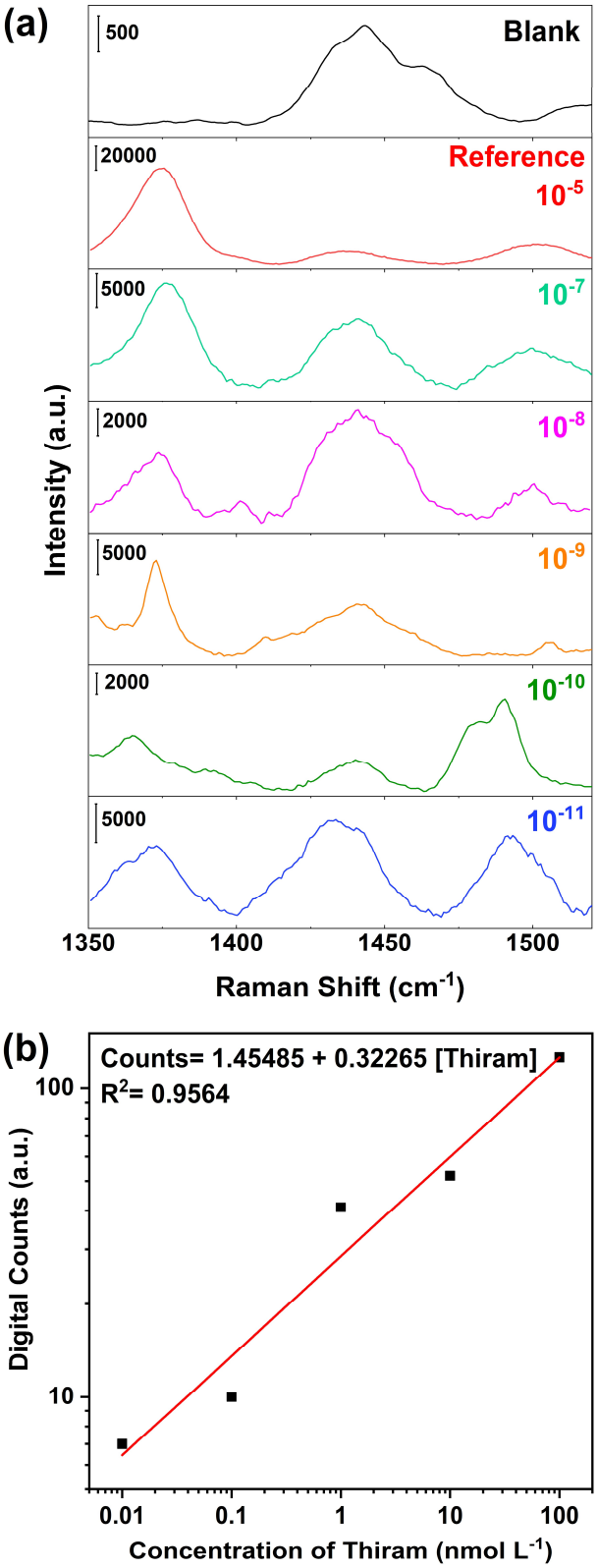

Figure 3.25. (a) Representative SERS spectra of a positive event obtained at the indicated thiram concentration. The reference spectrum corresponds with a positive event measured at 10 μmol L^{-1} (above the SM-SERS regime). (b) Calibration curve of digital counts versus the thiram concentration.

Thus, after plotting the corresponding digital SERS mappings (Figure 3.24b), the digital calibration curve of the total digital counts was achieved with a good linear correlation for concentration from 10^{-11}–10^{-7} mol L^{-1}, as presented in Figure 3.25b. Interestingly, a similar sensitivity*** is noticed for the digital calibration curves of both CV (Figure 3.21b) and thiram (Figure 3.25b). It is suggested that it indicates a similar performance of the sensor on the detection of molecules with distinct properties. Moreover, it seems to indicate the great reproducibility of the inkjet-printed substrate, mainly concerning that the inkjet-printing and the analysis of the substrates were performed on different days.

Although the linear range of the digital calibration curve was achieved for the thiram concentration ranging from 10^{-11}–10^{-7} mol L^{-1}, it was possible to detect the molecule at the concentration of 10^{-12} mol L^{-1}. Figure 3.26 shows the digital SERS mappings (Figure 3.26a) and the corresponding distribution of the SERS intensity around 1374 cm^{-1} for each spectrum of the SERS mappings (Figure 3.26b) obtained at the concentration of 10^{-12} mol L^{-1}.

The digital SERS mappings evidence a total of ten digital counts randomly distributed over the SERS mappings (Figure 3.26a). Moreover, Figure 3.26b shows that the relative digital counts for the concentration of 10^{-12} mol L^{-1} (7 %) are similar to the values found for the concentration of 10^{-10} (7 %) and 10^{-11} mol L^{-1} (5 %) (Figure 3.24a). It demonstrates that although the sensor is able to detect the thiram concentration of 10^{-12} mol L^{-1}, its response does not follow the linearity of the digital calibration curve, not being possible to quantify such concentration.

The distribution of the SERS intensity around 1374 cm^{-1} also demonstrates that the ten digital counts exhibit heterogeneous SERS intensities ranging from 2,857 up to 41,119 cts, where the digital count with the highest SERS intensity is highlighted in green (Figure 3.26b). It is interesting to notice that the highest SERS intensity observed for the concentration of 10^{-12} mol L^{-1} (green point, Figure 3.26b) is also the highest SERS intensity observed among all the thiram concentrations under the SM-SERS regime (Figure 3.24a). The corresponding SERS spectrum of the digital count highlighted in green (Figure 3.26b) is shown in Figure 3.26c, where the SERS bands of thiram are discernible and confirm the detection of the molecule. This data evidences the SERS intensity fluctuation intrinsic to the low probability of the molecules to be

*** The sensitivity is represented by the slope of the calibration curve.

adsorbed at effective hot spots at the SM-SERS regime. Therefore, it emphasizes the demand for using a quantification method approach such as the SERS digital protocol instead of the conventional method.

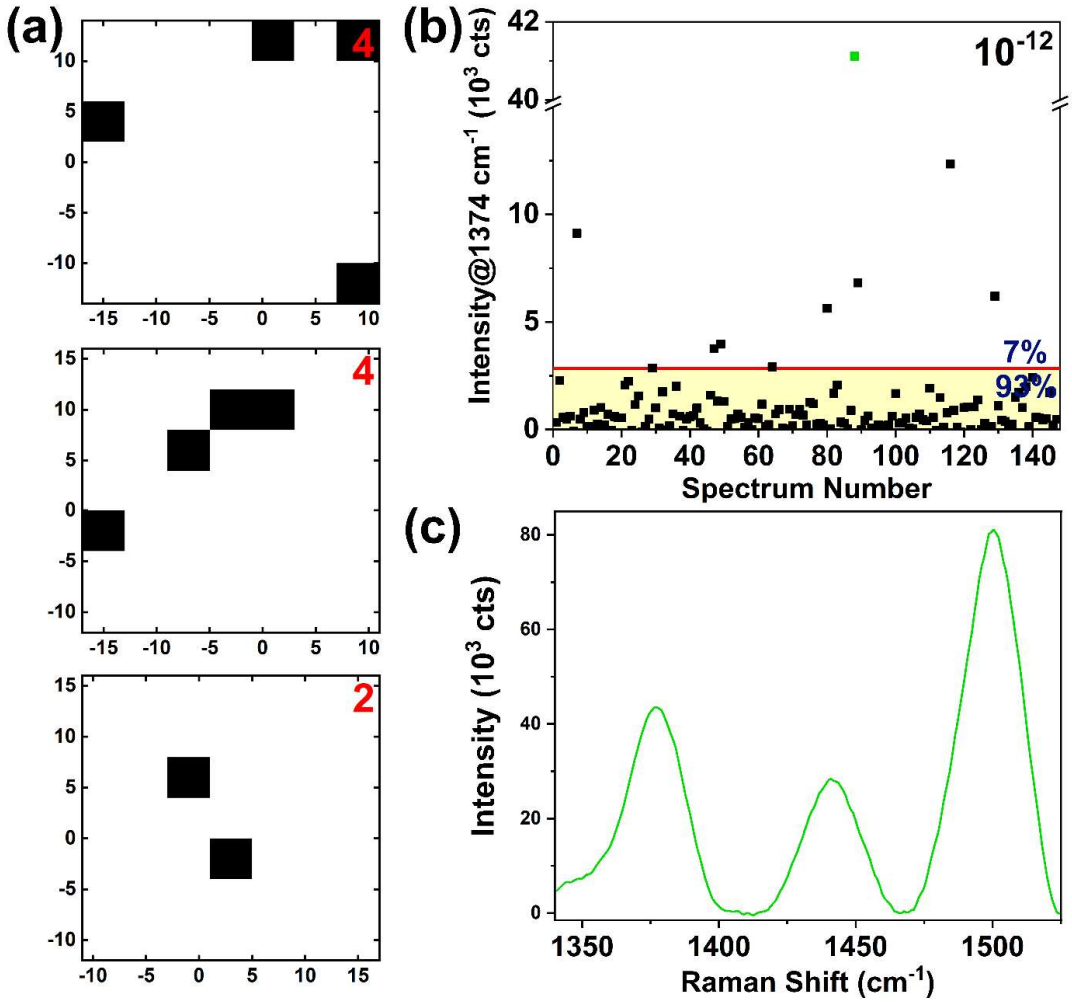

Figure 3.26. SERS data of the application of the digital protocol for the concentration of 10^{-12} mol L^{-1} of thiram. (a) Digital SERS mappings, where the black and white squares correspond to the digital counts and zero counts, respectively. (b) Relationship between the intensity of the band of thiram around 1374 cm^{-1} and each measurement point of the SERS mapping. The red line indicates the threshold of 3 times the standard deviation of the blank measurement. The percentage values indicate the relative digital and zero counts respectively above (white zone) and below (yellow zone) of the threshold. (c) SERS spectrum of the digital count that is highlighted as a green point in (b). For the digital count analysis, three SERS mappings (49 points each and step 4 x 4 μm, with 147 points in total) were acquired with a 100x objective and 785 laser line with a maximum power density of 46.25 kW cm^{-2}, an acquisition time of 3.5 s and 3 accumulation.

The SERS spectrum in Figure 3.26c exhibits an inversion of the relative intensity between the bands around 1374 and 1497 cm^{-1} compared to the SERS spectra in Figures 3.22 and 3.25a. Small fluctuations in the position of SERS band around 1374 cm^{-1} and the appearance of new bands were also observed in some spectra of the molecule. It is believed that these features may arise from the formation of the dimethyl dithiocarbamate residues by the cleavage of the S–S bond when the molecule is adsorbed on the metallic nanoparticle surface.[157,161]

The dimethyl dithiocarbamate residues can be adsorbed on the nanoparticle surface as mono- and bi-thiol forms, as demonstrated in Figure 3.27.[161,162] The adsorption mechanisms of the dimethyl dithiocarbamate residues lead to the different spatial orientation of the residues, which may affect specific vibrational modes and gives rise to the SERS bands fluctuations.

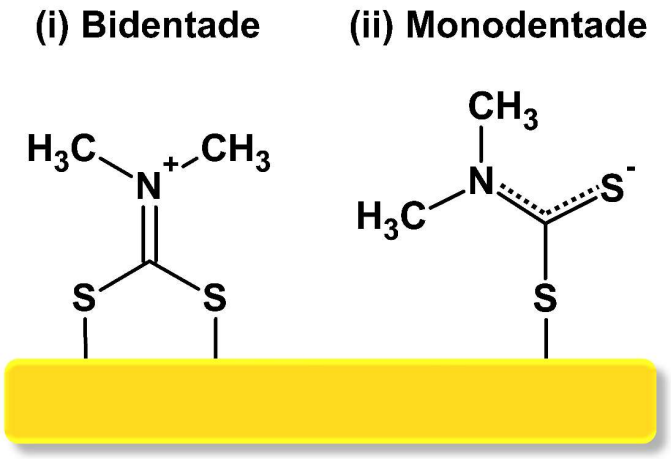

Figure 3.27. Adsorption mechanisms of dimethyl dithiocarbamate residues of thiram on a metallic surface.

The cleavage of thiram into the dimethyl dithiocarbamate residues are mainly characterized by the intensity decrease of the ν_{st}(SS) mode (around 560 cm^{-1}) and the enhancement of the ν_{st}(CN) mode (at 1497 cm^{-1}) that does not appear in the Raman spectrum.[157] Although some authors claim the predominant presence of the bi-thiol form,[157,161,162] the enhancement of the ν_{st}(C=S) mode (at 387 and 428 cm^{-1}) in this work (Figure B.2, Appendix B) seems to indicate the additional presence of the monothiol form or even thiram molecules that did not suffer cleavage. A more detailed Raman and SERS characterizations of thiram are shown in Figure B.2 and Table B.1 (Appendix B).

The SERS bands fluctuations for thiram on this work demands further investigation to better understand the thiram behavior on the metallic surface, concerning its cleavage into the dithiocarbamate residues as well as the influence of the spatial orientation of both molecule and residues on the metallic surface. Meanwhile, such discussion is beyond the scope of this work.

Finally, the results of the quantification for thiram were compared to recently reported data in the literature, as shown in Table 3.1. Comparing the lowest quantified concentration of thiram (defined here as the lowest concentration of the linear range of the digital calibration curve), the as-prepared paper-based inkjet-printed substrate demonstrated excellent performance on the detection of thiram over SERS substrates obtained by different methodologies and using a variety of MNPs. Moreover, it is highlighted that the lowest concentration of thiram quantified of 10^{-11} mol L^{-1} is equivalent to 2.4 ppt and it is much lower than the thiram tolerance defined by EPA for fruits such as apple and peach (7 ppm) and strawberry (20 ppm).[163]

Table 3.1. Comparison of the lowest quantified concentration of thiram achieved in this work and other works in literature.

SERS Substrate	The lowest quantified concentration of Thiram (mol L^{-1})	Reference
AuNP/paper strips	1.10^{-9}	164
Au@Ag NP/paper-based microfluidic substrate	1.10^{-9}	165
AgNP/hydrophobic paper-based substrate	1.10^{-9}	130
AgNP@Ag nanowire on polydimethylsiloxane substrate	1.10^{-10}	166
AgNP/Cu foam	1.10^{-9}	167
Au nanorod-coated capillary	1.10^{-7}	168
AuSph/paper-based Inkjet-printed substrate	1.10^{-11}	This work

3.2.3.7 Design and Costs of the Inkjet-printed SERS substrate

In summary, the inkjet-printed SERS substrate was designed with 253 sensing spots in a surface-modified chromatographic paper sheet of 10 x 10 cm for the experiments reported in this work, as shown in Figure 3.28. Moreover, the proposed fabrication of the inkjet-printed SERS substrate proved to be a low-cost method for this purpose. Considering only the consumables, the AuSph-113 Ink has a cost of less than U$ 10.00 (or R$ 40.99) per 1 mL, which yields the printing of approx. 6,605 spots of the inkjet-printed SERS substrate. Regarding the production of the inkjet-printed SERS substrate, it costs less than U$ 2.00 (or R$ 7.87) per printed-modified paper sheet with 253 spots, which leads to spots costing less than $ 0.01 (or R$ 0.03).

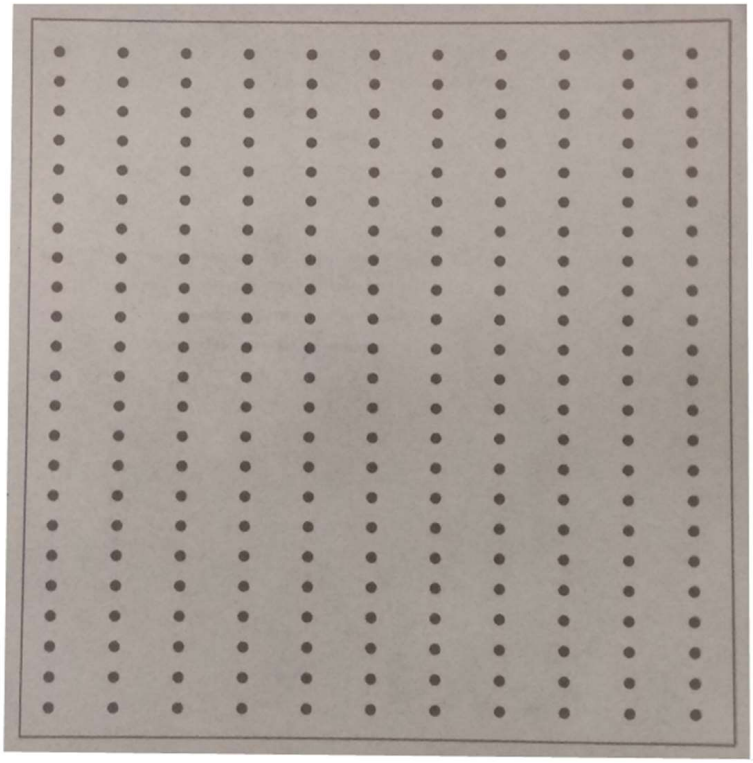

Figure 3.28. Photograph of the SERS substrate inkjet-printed with AuSph-113 Ink and five printing cycles, and designed with 253 spots distributed in a surface-modified chromatographic paper sheet of 10 x 10 cm.

3.3 CONCLUSIONS

In conclusion, the fabrication of a low-cost and facile inkjet-printed plasmonic paper-based SERS platform with high SERS efficiency is reported. The high SERS performance of the substrates relies on the great stability of a highly concentrated AuSph ink (over 1 year of storage) and the surface modification of the paper to render it hydrophobic allowing the concentration of the analyte upon evaporation. The great reproducibility of the SERS intensity between spots demonstrates the efficiency and robustness of the fabrication process.

Moreover, the reproducibility data evidence the key role of the SERS mapping tool to achieve accurate and reproducible results, especially for inherent heterogeneous substrates such as the proposed inkjet-printed SERS substrate. The SERS mapping tool is particularly important for quantification purposes at the SM-SERS regime, where the low probability of the molecules to be adsorbed at the effective hot spots difficulties the sampling process.

The paper-based SERS platform was tested towards the detection of CV and the fungicide thiram. Applying a digital protocol for SERS analysis, an excellent linear correlation between the digital counts and the analyte concentration was obtained at the single-molecule SERS regime, and for both molecules, the lowest quantified level of 10^{-11} mol L^{-1} was reached. Moreover, a thiram concentration of 10^{-12} mol L^{-1} was detected by the inkjet-printed SERS substrate. The excellent sensitivity performance of the inkjet-printed SERS substrate is reflected by the low sample volume needed (only 2 µL) concentrated in a small spot area (ca. 1.5 mm^2).

All the methodology employed in this work provided the fabrication of an ultralow-cost SERS substrate with a cost of less than U$ 2.00 per printed-modified paper sheet with 253 spots, which leads to spots costing less than $ 0.01 (considering only consumables). Considering these results, the inkjet-printed-SERS substrate proposed here demonstrates high potential for practical applications as well as for its use as a sensor for other analytes.

3.4 CRediT Authorship Contribution Statement

This work presents the following individual author contributions:

- **Naiara Vieira Godoy:** methodology, investigation, writing - original draft, formal analysis.
- **Daniel García-Lojo:** methodology, and formal analysis.
- **Fernando Aparecido Sigoli:** supervision, and resources.
- **Jorge Pérez-Juste:** supervision, resources, and writing – review & editing.
- **Isabel Pastoriza-Santos:** supervision, resources, and writing – review & editing.
- **Italo Odone Mazali:** conceptualization, supervision, writing – review & editing, project administration, resources, and funding acquisition.

3.5 Acknowledgments

I would like to thank Professor Dr. Hudson Giovani Zanin and Eng. Lenon Henrique da Costa from the Department of Semiconductors, Instruments, and Photonics (DSIF, UNICAMP) for the availability of the laboratory and Raman spectrometer. I would like to thank Professors Dr. Isabel Pastoriza Santos and Dr. Jorge Pérez Juste for the supervision on the development of this work in the Colloid Chemistry Group (University of Vigo, Spain), and M.Sc. Daniel García Lojo for helping with the development of the work. I also thank Anerise de Barros for CA measurements and Professor Dr. Edvaldo Sabadini for the CA and viscosity measurements. I also thank Flávia de Sousa Ferreira, Raisa Siqueira Alves, and Douglas Soares da Silva for TEM analysis.

4 CONCLUDING REMARKS AND FUTURE PERSPECTIVES

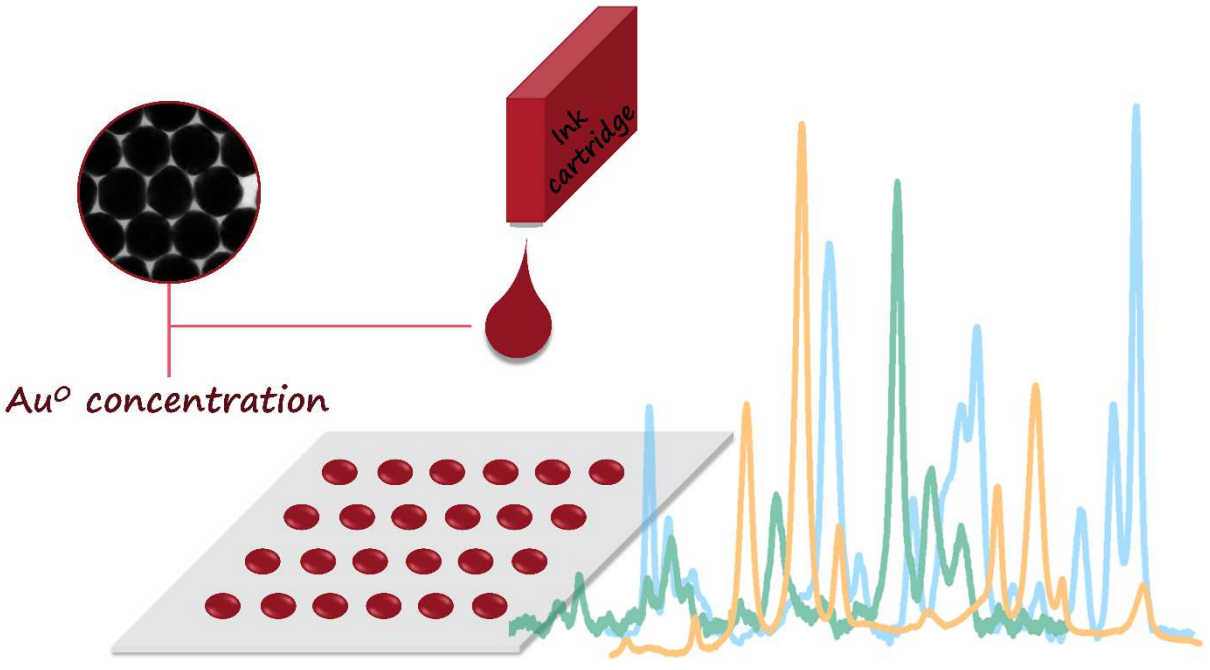

Naiara Vieira Godoy

This thesis aimed to meet the demand for developing high throughput, facile, and cost-effective SERS platforms with high sensitivity, reproducibility, and accurate analysis. For this, a complete set of strategies for the characterization of metallic nanoparticles (MNPs) and fabrication of a low-cost paper-based SERS platform was reported. The following, it is summarized the most relevant conclusions from the results in Chapter 2 and 3.

In Chapter 2, the development of a microwave-assisted decomposition procedure coupled with plasma-based spectrometric techniques was reported for the gold quantification in gold and gold-silver core-shell nanoparticles with complex matrices and a high content of organic matter. This work emerged to fulfill the lack of research concerning the metal concentration characterization of MNP colloid in more complex systems.

The microwave-assisted decomposition platform was initially developed for gold nanorod (AuNR) colloid. The high content of the surfactant CTAB showed itself to be a key challenge in the complete decomposition of the colloid by preventing the release of the Au^{3+} ions into the acidic solution, and the subsequent accurate gold quantification. To overcome this issue, several methodologies were tested and the parameters of sample volume, acidic mixture composition, and microwave program were extensively evaluated. The combination of a low sample volume (200 µL) with an acidic mixture of reverse aqua regia (1:3 v/v, $HCl:HNO_3$), and sulfuric acid, and a powerful microwave program provided an accurate gold quantification in AuNR colloid by ICP OES and ICP-MS. The results showed that both AuNR-total and AuNR-res fractions present *ca.* 100 % of gold content, indicating a high yield for the AuNR synthesis.

The application of the decomposition procedure was extended for gold nanospheres (AuSph) and gold-silver core-shell nanorods (Au@AgNR). The first also presents a high content of CTAB, while the latter presents high content of PVP in addition to the matrix with CTAB. The accurate gold quantification was successfully achieved by ICP-MS for both nanoparticle colloids, presenting a gold concentration recovery of *ca.* 100 % for both samples. The microwave-assisted decomposition platform demonstrated to be an effective and robust method for determinate the gold concentration in metallic nanoparticle colloid, presenting no interference of the high content of organic matter.

The proposed decomposition platform is an interesting strategy to be used as a characterization tool for both single- and multi-elemental nanoparticle colloids. Then, it opens the perspective of future works on different fronts. First, other essential parameters besides synthesis yield can be investigated using the platform, for example, stability over storage time and steps of separation and sampling of MNPs. Another perspective of future work is evaluating the applicability of the decomposition platform in metal quantification in MNP colloids with different stabilizers and matrices, for example, silver nanocubes stabilized in ethyleneglycol and the gold nanoparticle inks produced in this work.

It was demonstrated that the proposed decomposition procedure is a powerful characterization tool to investigate multi-elemental nanoparticle colloids such as silver-gold core-shell nanoparticles. In this sense, the simultaneous quantification of the multi-elemental components of the nanoparticles can be achieved by improving the separation method of the colloid fractions. Therefore, the accurate composition of a multi-elemental nanoparticle can be provided, which is useful for synthesis optimization and evaluation of the synthesis yield for each step of the reaction. For instance, the yield of both core and shell growth can be estimated, or even the yield of a galvanic substitution for a silver-gold alloy nanoparticle, for example. In conjunction with specific separation methods to separate different nanoparticle morphologies, the strategy can also be used to evaluate the synthesis yield regarding the formation of the morphology desired and byproducts.

In Chapter 3, the fabrication of an ultrasensitive plasmonic hydrophobic paper-based SERS platform by the inkjet printing method was reported. For this, AuSph inks consist of highly concentrated glycerol/ethanol dispersion of AuSph nanoparticles were synthesized. The AuSph inks exhibited excellent performance in the inkjet-printer, resulting in inkjet-printed spots with excellent definition, accuracy, and surface coverage. Moreover, the use of a hydrophobic chromatographic paper improved the sensing capabilities of the sensor by confining the analyte solution in the AuSph sensing platform as well as decreased the sample volume to just a few µl.

The combination of the highest concentrated AuSph ink (113 mmol L^{-1} in terms of Au^0) and five printing cycles gave rise to a SERS sensor with the greatest performance, overcoming the limitation of the hydrophobicity loss observed when more than five printing cycles were employed. Several parameters of the optimized SERS

sensor were evaluated. Among them, excellent spot-to-spot reproducibility was achieved even for AuSph spots from different inkjet-printed papers. The excellent reproducibility of the inkjet-printed SERS substrate was ensured by the high stability of the AuSph Ink over one year of storage and by using the SERS mapping tool.

The SERS sensor showed high sensitivity in the detection of the probe molecule crystal violet and the fungicide thiram. By applying a digital protocol for SERS analysis, a good linear correlation between the digital counts (or positive events) and the analyte concentration was obtained at the single-molecule SERS regime. In both cases, the quantification region threshold was 10^{-11} M. The great sensitivity performance of the inkjet-printed SERS substrate is reflected by the low sample volume needed (only 2 µL).

The great performance of the AuSph Ink and the inkjet-printed SERS substrates opens the perspective of future works. The application of the inkjet-printed SERS substrates could be explored in the detection of other analytes as well as exploring the simultaneous detection of several analytes. Regarding the fabrication of the sensor, other metallic nanoparticles with different morphologies and/or composition may be explored to obtain more efficient sensors. In this sense, an AuNR Ink could be evaluated since nanorods should provide higher SERS efficiency than AuSph, although their orientation on the substrate should be carefully studied. Another interesting strategy is exploring the use of highly size-controlled silver nanospheres and gold-silver core-shell nanospheres, to improve the SERS efficiency of the substrates.

In summary, the initial purpose of fabricating a highly sensitive and low-cost plasmonic paper-based SERS platform by the inkjet printing method was successfully attained. Furthermore, a strategy as a characterization tool of metallic nanoparticles was presented by the development of a microwave-assisted platform. In this context, it is expected that the results reported in this thesis contribute to the development of new strategies for the SERS substrates platforms as well as new strategies for the characterization of metallic nanoparticles.

REFERENCES

(1) Freestone, I.; Meeks, N.; Sax, M.; Higgitt, C. The Lycurgus Cup – A Roman Nanotechnology. *Gold Bull. Vol.* **2007**, *40*, 270–277. https://doi.org/10.1007/BF03215599.

(2) Barber, D.; Freestone, I. An Investigation of the Origin of the Colour of The Lycurgus Cup by Analytical Transmission Electron Microscopy. *Archaeometry* **1990**, *32* (1), 33–45. https://doi.org/10.1111/j.1475-4754.1990.tb01079.x.

(3) Daniel, M.-C.; Astruc, D. Gold Nanoparticles: Assembly, Supramolecular Chemistry, Quantum-Size-Related Properties, and Applications toward Biology, Catalysis and Nanotechnology. *Chem. Rev.* **2004**, *104* (1), 293–346. https://doi.org/10.1021/cr030698.

(4) Faraday, M. The Bakerian Lecture: Experimental Relations of Gold (and Other Metals) to Light. *Philos. Trans. R. Soc. London* **1857**, *147*, 145–181.

(5) Willets, K. A.; Van Duyne, R. P. Localized Surface Plasmon Resonance Spectroscopy and Sensing. *Annu. Rev. Phys. Chem.* **2007**, *58*, 267–297. https://doi.org/10.1146/annurev.physchem.58.032806.104607.

(6) Kosuda, K. M.; Bingham, J. M.; Wustholz, K. L.; Van Duyne, R. P. Nanostructures and Surface-Enhanced Raman Spectroscopy. In *Handbook of Nanoscale Optics and Electronics*; Wiederrecht, G. P., Ed.; Elsevier B.V., 2010; p 560.

(7) Le Ru, E. C.; Etchegoin, P. G. *Principles of Surface-Enhanced Raman Spectroscopy and Related Plasmonic Effects*, 1st ed.; Elsevier, 2009.

(8) Johnson, P. B.; Christy, R. W. Optical Constants of the Noble Metals. *Phys. Rev. B* **1972**, *6* (12–15), 4370–4379. https://doi.org/10.1103/PhysRevB.6.4370.

(9) Etchegoin, P. G.; Le Ru, E. C. Basic Electromagnetic Theory of SERS. In *Surface Enhanced Raman Spectroscopy: Analytical, Biophysical and Life Science Applications*; Schlücker, S., Ed.; Wiley-VCH Verlag GmbH & Co. KGaA, 2011; p 354. https://doi.org/10.1002/9783527632756.

(10) Mie, G. Beiträge Zur Optik Trüber Medien, Speziell Kolloidaler Metallösungen. *Ann. Phys.* **1908**, *330* (3), 377–445. https://doi.org/10.1002/andp.19083300302.

(11) Kelly, K. L.; Coronado, E.; Zhao, L. L.; Schatz, G. C. The Optical Properties of Metal Nanoparticles: The Influence of Size, Shape, and Dieletric Environment. *J. Phys. Chem. B* **2003**, *107* (3), 668–677. https://doi.org/10.1021/jp026731y.

(12) dos Santos, D. P.; Temperini, M. L. A.; Brolo, A. G. Surface Enhanced Raman Scattering (SERS): Principles and Applications for Single-Molecule Detection. In *Introduction to Plasmonics: advances and applications*; Szunerits, S., Boukherroub, R., Eds.; CRC Press, 2015; p 378.

(13) Garcia, M. A. Surface Plasmons in Metallic Nanoparticles : Fundamentals and Applications. *J. Phys. D. Appl. Phys.* **2011**, *44* (28), 283001. https://doi.org/10.1088/0022-3727/45/38/389501.

(14) Bastús, N. G.; Piella, J.; Puntes, V. Quantifying the Sensitivity of Multipolar (Dipolar, Quadrupolar, and Octapolar) Surface Plasmon Resonances in Silver Nanoparticles: The Effect of Size, Composition, and Surface Coating. *Langmuir* **2016**, *32* (1), 290–300. https://doi.org/10.1021/acs.langmuir.5b03859.

(15) Wiley, B. J.; Im, S. H.; Li, Z.-Y.; McLellan, J.; Siekkinen, A.; Xia, Y. Maneuvering the Surface Plasmon Resonance of Silver Nanostructures through Shape-Controlled Synthesis. *J. Phys. Chem. B* **2006**, *110* (32), 15666–15675. https://doi.org/10.1021/jp0608628.

(16) Bastús, N. G.; Comenge, J.; Puntes, V. Kinetically Controlled Seeded Growth Synthesis of Citrate-Stabilized Gold Nanoparticles of up to 200 Nm : Size Focusing versus Ostwald Ripening. *Langmuir* **2011**, *27* (17), 11098–11105. https://doi.org/10.1021/la201938u.

(17) Raman, C. V.; Krishnan, K. S. A New Type of Secondary Radiation. *Nature* **1928**, *121*, 501–502. https://doi.org/10.1038/121501c0.

(18) Landsberg, G.; Mandelstam, L. Eine Neue Erscheinung Bei Der Lichtzerstreuung in Krystallen. *Naturwissenschaften Vol.* **1928**, *16*, 557–558. https://doi.org/10.1007/BF01506807.

(19) Smekal, A. Zur Quantentheorie Der Dispersion. *Naturwissenschaften* **1923**, *11*, 873–875. https://doi.org/10.1007/BF01576902.

(20) Mitsutake, H.; Poppi, R. J.; Breitkreitz, M. C. Raman Imaging Spectroscopy: History, Fundamentals and Current Scenario of the Technique. *J. Braz. Chem. Soc.* **2019**, *30* (11), 2243–2258. https://doi.org/10.21577/0103-5053.20190116.

(21) American Chemical Society Historic Chemical Landmarks. The Raman Effect. http://www.acs.org/content/acs/en/education/whatischemistry/landmarks/ramaneffect.html (accessed August 05th, 2020).

(22) Silva, I. D. C.; Reinaldo, A. C.; Sigoli, F. A.; Mazali, I. O. Raman Spectroscopy-in Situ Characterization of Reversibly Intercalated Oxygen Vacancies in α-MoO3. *RSC Adv.* **2020**, *10* (31), 18512–18518. https://doi.org/10.1039/d0ra01207f.

(23) Godoy, N. V.; Pereira, J. L.; Duarte, E. H.; Tarley, C. R. T.; Segatelli, M. G. Influence of Activated Charcoal on the Structural and Morphological Characteristics of Ceramic Based on Silicon Oxycarbide (SiOC): A Promising Approach to Obtain a New Electrochemical Sensing Platform. *Mater. Chem. Phys.* **2016**, *175*, 33–45. https://doi.org/10.1016/j.matchemphys.2016.02.031.

(24) Alvarez-Puebla, R. A.; Dos Santos Jr, D. S.; Aroca, R. F. Surface-Enhanced Raman Scattering for Ultrasensitive Chemical Analysis of 1 and 2-Naphthalenethiols. *Analyst* **2004**, *129* (12), 1251–1256. https://doi.org/10.1039/b410488a.

(25) Santos, I. F. S.; Puglieri, T. S.; Barbosa, M. S.; Cardoso, A.; Rosado, T.; Gil, M.; Candeias, A.; Faria, D. L. A. De. Aspectos Químicos Na Investigação de Alguns Tipos de Eflorescência Em Bens Culturais. *Quim. Nova* **2019**, *42* (9), 1056–1065. https://doi.org/10.21577/0100-4042.20170422.

(26) Guo, J.; Liu, Y.; Yang, Y.; Li, Y.; Wang, R.; Ju, H. A Filter Supported Surface-Enhanced Raman Scattering “Nose” for Point-of-Care Monitoring of Gaseous Metabolites of Bacteria. *Anal. Chem.* **2020**, *92* (7), 5055–5063. https://doi.org/10.1021/acs.analchem.9b05400.

(27) Xu, Y.; Man, P.; Huo, Y.; Ning, T.; Li, C.; Man, B.; Yang, C. Synthesis of the 3D AgNF/AgNP Arrays for the Paper-Based Surface Enhancement Raman Scattering Application. *Sensors Actuators B Chem.* **2018**, *265*, 302–309. https://doi.org/10.1016/j.snb.2018.03.035.

(28) Fleischmann, M.; Hendra, P. J.; McQuillan, A. J. Raman Spectra of Pyridine Adsorbed at a Silver Electrode. *Chem. Phys. Lett.* **1974**, *26* (2), 163–166. https://doi.org/10.1016/0009-2614(74)85388-1.

(29) Jeanmaire, D. L.; Van Duyne, R. P. Surface Raman Spectroelectrochemistry Part I. Heterocyclic, Aromatic, and Aliphatic Amines Adsorbed on the Anodized Silver Electrode. *J. Electroanal. Chem. INTERFACIAL Electrochem.* **1977**, *84* (1), 1–20.

(30) Albrecht, M. G.; Creighton, J. A. Anomalously Intense Raman Spectra of Pyridine at a Silver Electrode. *J. Am. Chem. Soc.* **1977**, *99* (15), 5215–5217. https://doi.org/10.1021/ja00457a071.

(31) Philpott, M. R. Effect of Surface Plasmons on Transitions in Molecules. *J. Chem. Phys.* **1975**, *62* (5), 1812–1817.

(32) Moskovits, M. Surface Roughness and the Enhanced Intensity of Raman Scattering by Molecules Adsorbed on Metals. *J. Chem. Phys.* **1978**, *69* (9), 4159–4161. https://doi.org/10.1063/1.437095.

(33) Haynes, C. L.; Yonzon, C. R.; Zhang, X.; Duyne, R. P. Van. Surface-Enhanced Raman Sensors : Early History and the Development of Sensors for Quantitative Biowarfare Agent and Glucose Detection. *J. Raman Spectrosc.* **2005**, *36* (6–7), 471–484. https://doi.org/10.1002/jrs.1376.

(34) Aroca, R. *Surface-Enhanced Vibrational Spectroscopy*, 1st ed.; John Wiley & Sons, Ltd., 2006. https://doi.org/10.1002/9780470035641.

(35) Langer, J.; Jimenez de Aberasturi, D.; Aizpurua, J.; Alvarez-Puebla, R. A.; Auguié, B.; Baumberg, J. J.; Bazan, G. C.; Bell, S. E. J.; Boisen, A.; Brolo, A. G.; et al. Present and Future of Surface-Enhanced Raman Scattering. *ACS Nano* **2020**, *14*, 28–117. https://doi.org/10.1021/acsnano.9b04224.

(36) Vandenabeele, P. *Practical Raman Spectroscopy: An Introduction*, 1st ed.; John Wiley & Sons, Ltd.: Belgium, 2013.

(37) Guerrini, L.; Graham, D. Molecularly-Mediated Assemblies of Plasmonic Nanoparticles for Surface-Enhanced Raman Spectroscopy Pplications. *Chem. Soc. Rev.* **2012**, *41* (21), 7085–7107. https://doi.org/10.1039/c2cs35118h.

(38) Grasseschi, D.; Toma, H. E. The SERS Effect in Coordination Chemistry. *Coord.*

Chem. Rev. **2017**, *333*, 108–131. https://doi.org/10.1016/j.ccr.2016.11.019.

(39) Sant'Ana, A. C.; Corio, P.; Temperini, M. L. A. O Efeito SERS Na Análise de Traços: O Papel Das Superfícies Nanoestruturadas. *Quim. Nova* **2006**, *29* (4), 805–810. https://doi.org/10.1590/S0100-40422006000400030.

(40) Santos, E. D. B.; Sigoli, F. A.; Mazali, I. O. Surface-Enhanced Raman Scattering of 4-Aminobenzenethiol on Silver Nanoparticles Substrate. *Vib. Spectrosc.* **2013**, *68*, 246–250. https://doi.org/10.1016/j.vibspec.2013.08.003.

(41) Villa, J. E. L.; dos Santos, D. P.; Poppi, R. J. Fabrication of Gold Nanoparticle-Coated Paper and Its Use as a Sensitive Substrate for Quantitative SERS Analysis. *Microchim. Acta* **2016**, *183* (10), 2745–2752. https://doi.org/10.1007/s00604-016-1918-0.

(42) Berger, A. G.; Restaino, S. M.; White, I. M. Vertical-Flow Paper SERS System for Therapeutic Drug Monitoring of Flucytosine in Serum. *Anal. Chim. Acta* **2017**, *949*, 59–66. https://doi.org/10.1016/j.aca.2016.10.035.

(43) Djafari, J.; Fernández-Lodeiro, A.; García-Lojo, D.; Fernández-Lodeiro, J.; Rodríguez-González, B.; Pastoriza-Santos, I.; Pérez-Juste, J.; Capelo, J. L.; Lodeiro, C. Iron(II) as a Green Reducing Agent in Gold Nanoparticle Synthesis. *ACS Sustain. Chem. Eng.* **2019**, *7* (9), 8295–8302. https://doi.org/10.1021/acssuschemeng.8b06690.

(44) Indrasekara, A. S. D. S.; Meyers, S.; Shubeita, S.; Feldman, L. C.; Gustafsson, T.; Fabris, L. Gold Nanostar Substrates for SERS-Based Chemical Sensing in the Femtomolar Regime. *Nanoscale* **2014**, *6* (15), 8891–8899. https://doi.org/10.1039/c4nr02513j.

(45) Wang, B.; Zhang, L.; Zhou, X. Synthesis of Silver Nanocubes as a SERS Substrate for the Determination of Pesticide Paraoxon and Thiram. *Spectrochim. Acta - Part A Mol. Biomol. Spectrosc.* **2014**, *121*, 63–69. https://doi.org/10.1016/j.saa.2013.10.013.

(46) Bodelón, G.; Montes-García, V.; Fernández-lópez, C.; Pastoriza-Santos, I.; Pérez-juste, J.; Liz-marzán, L. M. Au@pNIPAM SERRS Tags for Multiplex Immunophenotyping Cellular Receptors and Imaging Tumor Cells. *Small* **2015**, *11* (33), 4149–4157. https://doi.org/10.1002/smll.201500269.

(47) Li, J.-M.; Yang, Y.; Qin, D. Hollow Nanocubes Made of Ag–Au Alloys for SERS Detection with Sensitivity of 10−8 M for Melamine. *J. Mater. Chem. C* **2014**, *2* (46), 9934–9940. https://doi.org/10.1039/C4TC02004A.

(48) Garcia-Leis, A.; Garcia-Ramos, J. V.; Sanchez-Cortes, S. Silver Nanostars with High SERS Performance. *J. Phys. Chem. C* **2013**, *117* (15), 7791–7795. https://doi.org/10.1021/jp401737y.

(49) Samal, A. K.; Polavarapu, L.; Rodal-Cedeira, S.; Liz-Marzán, L. M.; Pérez-Juste, J.; Pastoriza-Santos, I. Size Tunable Au@Ag Core–Shell Nanoparticles: Synthesis and Surface-Enhanced Raman Scattering Properties. *Langmuir* **2013**, *29* (48), 15076–15082. https://doi.org/10.1021/la403707j.

(50) Nikoobakht, B.; El-Sayed, M. A. Preparation and Growth Mechanism of Gold Nanorods (NRs) Using Seed-Mediated Growth Method. *Chem. Mater.* **2003**, *15* (10), 1957–1962. https://doi.org/10.1021/cm020732l.

(51) Etchegoin, P. G.; Le Ru, E. C. A Perspective on Single Molecule SERS: Current Status and Future Challenges. *Phys. Chem. Chem. Phys.* **2008**, *10* (40), 6079–6089. https://doi.org/10.1039/b809196j.

(52) Jones, S. T.; Taylor, R. W.; Esteban, R.; Abo-Hamed, E. K.; Bomans, P. H. H.; Sommerdijk, N. A. J. M.; Aizpurua, J.; Baumberg, J. J.; Scherman, O. A. Gold Nanorods with Sub-Nanometer Separation Using Cucurbit[n]Uril for SERS Applications. *Small* **2014**, *10* (21), 4298–4303. https://doi.org/10.1002/smll.201401063.

(53) Pazos-Perez, N.; Wagner, C. S.; Romo-Herrera, J. M.; Liz-Marzán, L. M.; García De Abajo, F. J.; Wittemann, A.; Fery, A.; Alvarez-Puebla, R. A. Organized Plasmonic Clusters with High Coordination Number and Extraordinary Enhancement in Surface-Enhanced Raman Scattering (SERS). *Angew. Chemie - Int. Ed.* **2012**, *51* (51), 12688–12693. https://doi.org/10.1002/anie.201207019.

(54) Taylor, R. W.; Esteban, R.; Mahajan, S.; Aizpurua, J.; Baumberg, J. J. Optimizing SERS from Gold Nanoparticle Clusters: Addressing the Near Field by an Embedded Chain Plasmon Model. *J. Phys. Chem. C* **2016**, *120* (19), 10512–10522. https://doi.org/10.1021/acs.jpcc.6b00506.

(55) Rodrigues, D. C.; Souza, M. L. De; Souza, K. S.; dos Santos, D. P.; Andrade, G.

F. S.; Temperini, M. L. A. Critical Assessment of Enhancement Factor Measurements in Surface-Enhanced Raman Scattering on Different Substrates. *Phys. Chem. Chem. Phys.* **2015**, *17* (33), 21294–21301. https://doi.org/10.1039/C4CP05080K.

(56) Fan, M.; Andrade, G. F. S.; Brolo, A. G. A Review on the Fabrication of Substrates for Surface Enhanced Raman Spectroscopy and Their Applications in Analytical Chemistry. *Anal. Chim. Acta* **2011**, *693* (1–2), 7–25. https://doi.org/10.1016/j.aca.2011.03.002.

(57) Solís, D. M.; Taboada, J. M.; Obelleiro, F.; Liz-Marzán, L. M.; de Abajo, F. J. G. Optimization of Nanoparticle-Based SERS Substrates through Large-Scale Realistic Simulations. *ACS Photonics* **2017**, *4* (2), 329–337.

(58) Shimada, T.; Imura, K.; Hossain, M. K.; Okamoto, H.; Kitajima, M. Near-Field Study on Correlation of Localized Electric Field and Nanostructures in Monolayer Assembly of Gold Nanoparticles. *J. Phys. Chem. C* **2008**, *112* (11), 4033–4035. https://doi.org/10.1021/jp8004508.

(59) Lee, A.; Ahmed, A.; dos Santos, D. P.; Coombs, N.; Park, J. Il; Gordon, R.; Brolo, A. G.; Kumacheva, E. Side-by-Side Assembly of Gold Nanorods Reduces Ensemble- Averaged SERS Intensity. *J. Phys. Chem. C* **2012**, *116* (9), 5538–5545.

(60) Fang, Y.; Seong, N.-H.; Dlott, D. D. Measurement of the Distribution of Site Enhancements in Surface-Enhanced Raman Scattering. *Science (80-.).* **2008**, *321* (5887), 388–392. https://doi.org/10.1126/science.1159499.

(61) Etchegoin, P. G.; Meyer, M.; Le Ru, E. C. Statistics of Single Molecule SERS Signals: Is There a Poisson Distribution of Intensities? *Phys. Chem. Chem. Phys.* **2007**, *9* (23), 3006–3010. https://doi.org/10.1039/b704013j.

(62) De Marchi, S.; Bodelón, G.; Vázquez-Iglesias, L.; Liz-Marzán, L. M.; Pérez-Juste, J.; Pastoriza-Santos, I. Surface-Enhanced Raman Scattering (SERS) Imaging of Bioactive Metabolites in Mixed Bacterial Populations. *Appl. Mater. Today* **2019**, *14*, 207–215. https://doi.org/10.1016/j.apmt.2018.12.005.

(63) Liu, X.; Wang, J.; Wang, J.; Tang, L.; Ying, Y. Flexible and Transparent Surface-Enhanced Raman Scattering (SERS)-Active Metafilm for Visualizing Trace

Molecules via Raman Spectral Mapping. *Anal. Chem.* **2016**, *88* (12), 6166–6173. https://doi.org/10.1021/acs.analchem.6b00858.

(64) Albuquerque, C. D. L.; Poppi, R. J. Detection of Malathion in Food Peels by Surface-Enhanced Raman Imaging Spectroscopy and Multivariate Curve Resolution. *Anal. Chim. Acta* **2015**, *879*, 24–33. https://doi.org/10.1016/j.aca.2015.04.019.

(65) Reokrungruang, P.; Chatnuntawech, I.; Dharakul, T.; Bamrungsap, S. A Simple Paper-Based Surface Enhanced Raman Scattering (SERS) Platform and Magnetic Separation for Cancer Screening. *Sensors Actuators B Chem.* **2019**, *285*, 462–469. https://doi.org/10.1016/j.snb.2019.01.090.

(66) Villa, J. E. L.; Afonso, M. A. S.; dos Santos, D. P.; Mercadal, P. A.; Coronado, E. A.; Poppi, R. J. Colloidal Gold Clusters Formation and Chemometrics for Direct SERS Determination of Bioanalytes in Complex Media. *Spectrochim. Acta Part A Mol. Biomol. Spectrosc.* **2020**, *224*, 117380. https://doi.org/10.1016/j.saa.2019.117380.

(67) IUPAC. *Compendium of Chemical Terminology*, 2nd ed. (the "Gold Book"). Complied by A.D. McNaught and A. Wilkinson. Blackwell Scientific Publications: Oxford (1997). Online version (2019-) created by S.J. Chalk. ISBN 0-9678550-9-8 https://doi.org/10.1351/goldbook.

(68) de Albuquerque, C. D. L.; Sobral-Filho, R. G.; Poppi, R. J.; Brolo, A. G. Digital Protocol for Chemical Analysis at Ultralow Concentrations by Surface-Enhanced Raman Scattering. *Anal. Chem.* **2018**, *90* (2), 1248–1254. https://doi.org/10.1021/acs.analchem.7b03968.

(69) Godoy, N. V.; Galazzi, R. M.; Chacón-Madrid, K.; Arruda, M. A. Z.; Mazali, I. O. Evaluating the Total Gold Concentration in Metallic Nanoparticles with a High Content of Organic Matter through Microwave-Assisted Decomposition Platform and Plasma-Based Spectrometric Techniques (ICP-MS and ICP OES). *Talanta* **2020**. https://doi.org/10.1016/j.talanta.2020.121808.

(70) Jana, N. R.; Gearheart, L.; Murphy, C. J. Wet Chemical Synthesis of High Aspect Ratio Cylindrical Gold Nanorods. *J. Phys. Chem. B* **2001**, *105* (19), 4065–4067. https://doi.org/10.1021/jp0107964.

(71) Métraux, G. S.; Mirkin, C. A. Rapid Thermal Synthesis of Silver Nanoprisms with Chemically Tailorable Thickness. *Adv. Mater.* **2005**, *17* (4), 412–415. https://doi.org/10.1002/adma.200401086.

(72) Sánchez-Iglesias, A.; Pastoriza-Santos, I.; Pérez-Juste, J.; Rodríguez-González, B.; de Abajo, F. J. G.; Liz-Marzán, L. M. Synthesis and Optical Properties of Gold Nanodecahedra with Size Control. *Adv. Mater.* **2006**, *18* (19), 2529–2534. https://doi.org/10.1002/adma.200600475.

(73) Chen, T. W.; Huang, W. F.; Kang, J. X.; Zhang, D. F.; Guo, L. Cycling Potential Engineering Surface Configuration of Sandwich Au@Ni@PtNiAu for Superior Catalytic Durability. *Nano Energy* **2018**, *52* (July), 22–28. https://doi.org/10.1016/j.nanoen.2018.07.029.

(74) Sui, N.; Wang, T.; Bai, Q.; Yue, R.; Jiang, H.; Xiao, H.; Liu, M.; Wang, L.; Zhu, Z.; Yu, W. W. Facile Synthesis of Ternary Au@PdNi Core-Shell Nanoparticles with Enhanced Electrocatalytic Performance for Ethanol Oxidation Reaction. *J. Alloys Compd.* **2020**, *817*, 153335. https://doi.org/10.1016/j.jallcom.2019.153335.

(75) Thota, S.; Zhou, Y.; Chen, S.; Zou, S.; Zhao, J. Formation of Bimetallic Dumbbell Shaped Particles with a Hollow Junction during Galvanic Replacement Reaction. *Nanoscale* **2017**, *9* (18), 6128–6135. https://doi.org/10.1039/C7NR00917H.

(76) Leopold, K.; Philippe, A.; Wörle, K.; Schaumann, G. E. Analytical Strategies to the Determination of Metal-Containing Nanoparticles in Environmental Waters. *Trends Anal. Chem.* **2016**, *84*, 107–120. https://doi.org/10.1016/j.trac.2016.03.026.

(77) Ramos, K.; Gómez-Gómez, M. M.; Cámara, C.; Ramos, L. Silver Speciation and Characterization of Nanoparticles Released from Plastic Food Containers by Single Particle ICPMS. *Talanta* **2016**, *151*, 83–90. https://doi.org/10.1016/j.talanta.2015.12.071.

(78) Merrifield, R. C.; Stephan, C.; Lead, J. R. Quantification of Au Nanoparticle Biouptake and Distribution to Freshwater Algae Using Single Cell – ICP-MS. *Environ. Sci. Technol.* **2018**, *52* (4), 2271–2277. https://doi.org/10.1021/acs.est.7b04968.

(79) Navarro, E.; Piccapietra, F.; Wagner, B.; Marconi, F.; Kaegi, R.; Odzak, N.; Sigg, L.; Behra, R. Toxicity of Silver Nanoparticles to Chlamydomonas Reinhardtii. *Environ. Sci. Technol.* **2008**, *42* (23), 8959–8964. https://doi.org/10.1021/es801785m.

(80) Doremus, R. H. Optical Properties of Small Gold Particles. *J. Chem. Phys.* **1964**, *40* (8), 2389–2396. https://doi.org/10.1063/1.1725519.

(81) Rao, P.; Doremus, R. Kinetics of Growth of Nanosized Gold Clusters in Glass. *J. Non. Cryst. Solids* **1996**, *203*, 202–205. https://doi.org/10.1016/0022-3093(96)00483-8.

(82) Scarabelli, L.; Grzelczak, M.; Liz-Marzán, L. M. Tuning Gold Nanorod Synthesis through Prereduction with Salicylic Acid. *Chem. Mater.* **2013**, *25* (21), 4232–4238. https://doi.org/10.1021/cm402177b.

(83) Scarabelli, L.; Sánchez-Iglesias, A.; Pérez-Juste, J.; Liz-Marzán, L. M. A "Tips and Tricks" Practical Guide to the Synthesis of Gold Nanorods. *J. Phys. Chem. Lett.* **2015**, *6* (21), 4270–4279. https://doi.org/10.1021/acs.jpclett.5b02123.

(84) Hendel, T.; Wuithschick, M.; Kettemann, F.; Birnbaum, A.; Rademann, K.; Polte, J. In Situ Determination of Colloidal Gold Concentrations with UV–Vis Spectroscopy: Limitations and Perspectives. *Anal. Chem.* **2014**, *86* (22), 11115–11124. https://doi.org/10.1021/ac502053s.

(85) Galazzi, R. M.; Chacón-Madrid, K.; Freitas, D. C.; da Costa, L. F.; Arruda, M. A. Z. Inductively Coupled Plasma Mass Spectrometry Based Platforms for Studies Involving Nanoparticle Effects in Biological Samples. *Rapid Commun. Mass Spectrom.* **2020**, *34*, e8726. https://doi.org/10.1002/rcm.8726.

(86) Faucher, S.; Soulé, S.; Bulteau, A.-L.; Allouche, J.; Lespes, G. Gold and Silver Quantification from Gold-Silver Nanoshells in HaCaT Cells. *J. Trace Elem. Med. Biol.* **2018**, *47*, 70–78. https://doi.org/10.1016/j.jtemb.2018.01.017.

(87) Chao, J.; Liu, J.; Yu, S.; Feng, Y.; Tan, Z.; Liu, R.; Yin, Y. Speciation Analysis of Silver Nanoparticles and Silver Ions in Antibacterial Products and Environmental Waters via Cloud Point Extraction-Based Separation. *Anal. Chem.* **2011**, *83* (17), 6875–6882. https://doi.org/10.1021/ac201086a.

(88) Fabricius, A.-L.; Duester, L.; Meermann, B.; Ternes, T. A. ICP-MS-Based

Characterization of Inorganic Nanoparticles—Sample Preparation and off-Line Fractionation Strategies. *Anal. Bioanal. Chem.* **2014**, *406* (2), 467–479. https://doi.org/10.1007/s00216-013-7480-2.

(89) Galazzi, R. M.; Santos, E. de B.; Caurin, T.; Pessôa, G. de S.; Mazali, I. O.; Arruda, M. A. Z. The Importance of Evaluating the Real Metal Concentration in Nanoparticles Post-Synthesis for Their Applications: A Case-Study Using Silver Nanoparticles. *Talanta* **2016**, *146*, 795–800. https://doi.org/10.1016/j.talanta.2015.06.016.

(90) Xu, D.; Mao, J.; He, Y.; Yeung, E. S. Size-Tunable Synthesis of High-Quality Gold Nanorods under Basic Conditions by Using H2O2 as the Reducing Agent. *J. Mater. Chem. C* **2014**, *2* (25), 4989–4996. https://doi.org/10.1039/c4tc00483c.

(91) Fu, Q.; Zhang, D. G.; Yi, M. F.; Wang, X. X.; Chen, Y. K.; Wang, P.; Ming, H. Effect of Shell Thickness on a Au–Ag Core–Shell Nanorods-Based Plasmonic Nano-Sensor. *J. Opt.* **2012**, *14* (8), 085001. https://doi.org/10.1088/2040-8978/14/8/085001.

(92) Turkevich, J.; Stevenson, P. C.; Hillier, J. A Study of the Nucleation and Growth Processes in the Synthesis of Colloidal Gold. *Discuss. Faraday Soc.* **1951**, *11*, 55–75. https://doi.org/10.1039/df9511100055.

(93) Rodríguez-Fernández, J.; Pérez-Juste, J.; García de Abajo, F. J.; Liz-Marzán, L. M. Seeded Growth of Submicron Au Colloids with Quadrupole Plasmon Resonance Modes. *Langmuir* **2006**, *22* (16), 7007–7010. https://doi.org/10.1021/la060990n.

(94) Jiang, X. C.; Brioude, A.; Pileni, M. P. Gold Nanorods: Limitations on Their Synthesis and Optical Properties. *Colloids Surfaces A Physicochem. Eng. Asp.* **2006**, *277* (1–3), 201–206. https://doi.org/10.1016/j.colsurfa.2005.11.062.

(95) Pastorello, M.; Sigoli, F. A.; dos Santos, D. P.; Mazali, I. O. On the Use of Au@Ag Core-Shell Nanorods for SERS Detection of Thiram Diluted Solutions. *Spectrochim. Acta Part A Mol. Biomol. Spectrosc.* **2020**, *231*, 118113. https://doi.org/10.1016/j.saa.2020.118113.

(96) Pérez-Juste, J.; Pastoriza-Santos, I.; Liz-Marzán, L. M.; Mulvaney, P. Gold Nanorods: Synthesis, Characterization and Applications. *Coord. Chem. Rev.*

2005, *249* (17–18), 1870–1901. https://doi.org/10.1016/j.ccr.2005.01.030.

(97) Zhu, J.; Zhang, F.; Li, J.-J.; Zhao, J.-W. The Effect of Nonhomogeneous Silver Coating on the Plasmonic Absorption of Au–Ag Core–Shell Nanorod. *Gold Bull.* **2014**, *47*, 47–55. https://doi.org/10.1007/s13404-013-0111-z.

(98) Jana, N. R.; Gearheart, L.; Murphy, C. J. Seed-Mediated Growth Approach for Shape-Controlled Synthesis of Spheroidal and Rod-like Gold Nanoparticles Using a Surfactant Template. *Adv. Mater.* **2001**, *13* (18), 1389–1393. https://doi.org/10.1002/1521-4095(200109)13:18<1389::AID-ADMA1389>3.0.CO;2-F.

(99) Nikoobakht, B.; El-sayed, M. A. Evidence for Bilayer Assembly of Cationic Surfactants on the Surface of Gold Nanorods. *Langmuir* **2001**, *17* (20), 6368–6374. https://doi.org/10.1021/la010530o.

(100) Sau, T. K.; Murphy, C. J. Self-Assembly Patterns Formed upon Solvent Evaporation of Aqueous Cetyltrimethylammonium Bromide-Coated Gold Nanoparticles of Various Shapes. *Langmuir* **2005**, *21* (7), 2923–2929. https://doi.org/10.1021/la047488s.

(101) Gómez-Graña, S.; Hubert, F.; Testard, F.; Guerrero-Martínez, A.; Grillo, I.; Liz-Marzán, L. M.; Spalla, O. Surfactant (Bi) Layers on Gold Nanorods. *Langmuir* **2012**, *28* (2), 1453–1459. https://doi.org/10.1021/la203451p.

(102) Godoy, N. V.; García-Lojo, D.; Sigoli, F. A.; Pérez-Juste, J.; Pastoriza-Santos, I.; Mazali, I. O. Ultrasensitive Inkjet-Printed Based SERS Sensor Combining a High-Performance Gold Nanosphere Ink and Hydrophobic Paper. *Sensors Actuators B. Chem.* **2020**, *320*, 128412. https://doi.org/10.1016/j.snb.2020.128412.

(103) Gómez-Graña, S.; Fernández-López, C.; Polavarapu, L.; Salmon, J.-B.; Leng, J.; Pastoriza-santos, I.; Pérez-Juste, J. Gold Nanooctahedra with Tunable Size and Microfluidic-Induced 3D Assembly for Highly Uniform SERS-Active Supercrystals. *Chem. Mater.* **2015**, *27* (24), 8310–8317. https://doi.org/10.1021/acs.chemmater.5b03620.

(104) Plou, J.; García, I.; Charconnet, M.; Astobiza, I.; García-Astrain, C.; Matricardi, C.; Mihi, A.; Carracedo, A.; Liz-marzán, L. M. Multiplex SERS Detection of

Metabolic Alterations in Tumor Extracellular Media. *Adv. Funct. Mater.* **2020**, *30* (17), 1910335. https://doi.org/10.1002/adfm.201910335.

(105) D'Apuzzo, F.; Sengupta, R. N.; Overbay, M.; Aronoff, J. S.; Rogacs, A.; Barcelo, S. J. A Generalizable Single-Chip Calibration Method for Highly Quantitative SERS via Inkjet Dispense. *Anal. Chem.* **2020**, *92* (1), 1372–1378. https://doi.org/10.1021/acs.analchem.9b04535.

(106) Liu, S.; Kannegulla, A.; Kong, X.; Sun, R.; Liu, Y.; Wang, R.; Yu, Q.; Wang, A. X. Simultaneous Colorimetric and Surface-Enhanced Raman Scattering Detection of Melamine from Milk. *Spectrochim. Acta - Part A Mol. Biomol. Spectrosc.* **2020**, *231*, 118130. https://doi.org/10.1016/j.saa.2020.118130.

(107) Lee, J.-H.; You, M.-H.; Kim, G.-H.; Nam, J.-M. Plasmonic Nanosnowmen with a Conductive Junction as Highly Tunable Nanoantenna Structures and Sensitive, Quantitative and Multiplexable Surface-Enhanced Raman Scattering Probes. *Nano Lett.* **2014**, *14* (11), 6217–6225. https://doi.org/10.1021/nl502541u.

(108) Zhang, Y.; Yu, W.; Pei, L.; Lai, K.; Rasco, B. A.; Huang, Y. Rapid Analysis of Malachite Green and Leucomalachite Green in Fish Muscles with Surface-Enhanced Resonance Raman Scattering. *Food Chem.* **2015**, *169*, 80–84. https://doi.org/10.1016/j.foodchem.2014.07.129.

(109) Qu, L.; Geng, Y.; Bao, Z.; Riaz, S.; Li, H. Silver Nanoparticles on Cotton Swabs for Improved Surface-Enhanced Raman Scattering, and Its Application to the Detection of Carbaryl. *Microchim. Acta* **2016**, *183* (4), 1307–1313. https://doi.org/10.1007/s00604-016-1760-4.

(110) Jahn, M.; Patze, S.; Bocklitz, T.; Weber, K.; Cialla-May, D.; Popp, J. Towards SERS Based Applications in Food Analytics: Lipophilic Sensor Layers for the Detection of Sudan III in Food Matrices. *Anal. Chim. Acta* **2015**, *860*, 43–50. https://doi.org/10.1016/j.aca.2015.01.005.

(111) Zhang, C.; You, T.; Yang, N.; Gao, Y.; Jiang, L.; Yin, P. Hydrophobic Paper-Based SERS Platform for Direct-Droplet Quantitative Determination of Melamine. *Food Chem.* **2019**, *287*, 363–368. https://doi.org/10.1016/j.foodchem.2019.02.094.

(112) Haddad, A.; Comanescu, M. A.; Green, O.; Kubic, T. A.; Lombardi, J. R.

Detection and Quantitation of Trace Fentanyl in Heroin by Surface-Enhanced Raman Spectroscopy. *Anal. Chem.* **2018**, *90* (21), 12678–12685. https://doi.org/10.1021/acs.analchem.8b02909.

(113) Meng, J.; Tang, X.; Zhou, B.; Xie, Q.; Yang, L. Designing of Ordered Two-Dimensional Gold Nanoparticles Film for Cocaine Detection in Human Urine Using Surface-Enhanced Raman Spectroscopy. *Talanta* **2017**, *164* (October 2016), 693–699. https://doi.org/10.1016/j.talanta.2016.10.101.

(114) Sun, Y.; Xu, L.; Zhang, F.; Song, Z.; Hu, Y.; Ji, Y.; Shen, J.; Li, B.; Lu, H.; Yang, H. A Promising Magnetic SERS Immunosensor for Sensitive Detection of Avian Influenza Virus. *Biosens. Bioelectron.* **2017**, *89*, 906–912. https://doi.org/10.1016/j.bios.2016.09.100.

(115) Le Ru, E. C.; Etchegoin, P. G. Quantifying SERS Enhancements. *MRS Bull.* **2013**, *38* (8), 631–640. https://doi.org/10.1557/mrs.2013.158.

(116) Lin, S.; Lin, X.; Shang, Y.; Han, S.; Hasi, W.; Wang, L. Self-Assembly of Faceted Gold Nanocrystals for Surface-Enhanced Raman Scattering Application. *J. Phys. Chem. C* **2019**, *123* (40), 24714–24722. https://doi.org/10.1021/acs.jpcc.9b06686.

(117) Zhang, C.-H.; Zhu, J.; Li, J.-J.; Zhao, J.-W. Small and Sharp Triangular Silver Nanoplates Synthesized Utilizing Tiny Triangular Nuclei and Their Excellent SERS Activity for Selective Detection of Thiram Residue in Soil. *ACS Appl. Mater. Interfaces* **2017**, *9* (20), 17387–17398. https://doi.org/10.1021/acsami.7b04365.

(118) Zhang, C.-L.; Lv, K.-P.; Cong, H.-P.; Yu, S.-H. Controlled Assemblies of Gold Nanorods in PVA Nanofiber Matrix as Flexible Free-Standing SERS Substrates by Electrospinning. *Small* **2012**, *8* (5), 648–653. https://doi.org/10.1002/smll.201102230.

(119) García-Lojo, D.; Núñez-Sánchez, S.; Gómez-Graña, S.; Grzelczak, M.; Pastoriza-Santos, I.; Pérez-Juste, J.; Liz-Marzán, L. M. Plasmonic Supercrystals. *Acc. Chem. Res.* **2019**, *52* (7), 1855–1864. https://doi.org/10.1021/acs.accounts.9b00213.

(120) Lee, T.; Kwon, S.; Jung, S.; Lim, H.; Lee, J.-J. Macroscopic Ag Nanostructure

Array Patterns with High-Density Hotspots for Reliable and Ultra-Sensitive SERS Substrates. *Nano Res.* **2019**, *12* (10), 2554–2558. https://doi.org/10.1007/s12274-019-2484-7.

(121) Vo-Dinh, T.; Hiromoto, M. Y. K.; Begun, G. M.; Moody, R. L. Surface-Enhanced Raman Spectrometry for Trace Organic Analysis. *Anal. Chem.* **1984**, *56* (9), 1667–1670. https://doi.org/10.1021/ac00273a029.

(122) Tran, C. D. Subnanogram Detection of Dyes on Filter Paper by Surface-Enhanced Raman Scattering Spectrometry. *Anal. Chem.* **1984**, *56* (4), 824–826. https://doi.org/10.1021/ac00268a057.

(123) Tran, C. D. In Situ Identification of Paper Chromatogram Spots by Surface Enhanced Raman Scattering. *J. Chromatogr. A* **1984**, *292* (2), 432–438. https://doi.org/10.1016/S0021-9673(01)83624-4.

(124) Vo-Dinh, T.; Uziel, M.; Morrison, A. L. Surface-Enhanced Raman Analysis of Benzo[A]Pyrene-DNA Adducts on Silver-Coated Cellulose Substrates. *Appl. Spectrosc.* **1987**, *41* (4), 605–610. https://doi.org/10.1366/0003702874448616.

(125) Sun, M.; Li, B.; Liu, X.; Chen, J.; Mu, T.; Zhu, L.; Guo, J.; Ma, X. Performance Enhancement of Paper-Based SERS Chips by Shell-Isolated Nanoparticle-Enhanced Raman Spectroscopy. *J. Mater. Sci. Technol.* **2019**, *35* (10), 2207–2212. https://doi.org/10.1016/j.jmst.2019.05.055.

(126) Zeng, F.; Mou, T.; Zhang, C.; Huang, X.; Wang, B.; Ma, X.; Guo, J. Paper-Based SERS Analysis with Smartphones as Raman Spectral Analyzers. *Analyst* **2019**, *144* (1), 137–142. https://doi.org/10.1039/C8AN01901K.

(127) Zeng, F.; Duan, W.; Zhu, B.; Mu, T.; Zhu, L.; Guo, J.; Ma, X. Paper-Based Versatile Surface-Enhanced Raman Spectroscopy Chip with Smartphone-Based Raman Analyzer for Point-of-Care Application. *Anal. Chem.* **2019**, *91* (1), 1064–1070. https://doi.org/10.1021/acs.analchem.8b04441.

(128) Yu, W. W.; White, I. M. Inkjet Printed Surface Enhanced Raman Spectroscopy Array on Cellulose Paper. *Anal. Chem.* **2010**, *82* (23), 9626–9630. https://doi.org/10.1021/ac102475k.

(129) Teixeira, C. A.; Poppi, R. J. Paper-Based SERS Substrate and One-Class Classifier to Monitor Thiabendazole Residual Levels in Extracts of Mango Peels.

Spectrochim. Acta Part A Mol. Biomol. Spectrosc. **2020**, *229*, 117913. https://doi.org/10.1016/j.saa.2019.117913.

(130) Lee, M.; Oh, K.; Choi, H.-K.; Lee, S. G.; Youn, H. J.; Lee, H. L.; Jeong, D. H. Subnanomolar Sensitivity of Filter Paper-Based SERS Sensor for Pesticide Detection by Hydrophobicity Change of Paper Surface. *ACS Sensors* **2018**, *3* (1), 151–159. https://doi.org/10.1021/acssensors.7b00782.

(131) Das, D.; Senapati, S.; Nanda, K. K. "Rinse, Repeat": An Efficient and Reusable SERS and Catalytic Platform Fabricated by Controlled Deposition of Silver Nanoparticles on Cellulose Paper. *ACS Sustain. Chem. Eng.* **2019**, *7* (16), 14089–14101. https://doi.org/10.1021/acssuschemeng.9b02651.

(132) Zheng, G.; Polavarapu, L.; Liz-Marzán, L. M.; Pastoriza-Santos, I.; Pérez-Juste, J. Gold Nanoparticle-Loaded Filter Paper: A Recyclable Dip-Catalyst for Real-Time Reaction Monitoring by Surface Enhanced Raman Scattering. *Chem. Commun.* **2015**, *51* (22), 4572–4575. https://doi.org/10.1039/C4CC09466B.

(133) Qu, L.; Li, D.; Xue, J.; Zhai, W.; Fossey, J. S. Batch Fabrication of Disposable Screen Printed SERS Arrays. **2012**, No. Table 1, 2–7.

(134) Lee, C. H.; Tian, L.; Singamaneni, S. Paper-Based SERS Swab for Rapid Trace Detection on Real-World Surfaces. *ACS Appl. Mater. Interfaces* **2010**, *2* (12), 3429–3435. https://doi.org/10.1021/am1009875.

(135) Polavarapu, L.; Porta, A. La; Novikov, S. M.; Coronado-Puchau, M.; Liz-Marzán, L. M. Pen-on-Paper Approach Toward the Design of Universal Surface Enhanced Raman Scattering Substrates. *Small* **2014**, *10* (15), 3065–3071. https://doi.org/10.1002/smll.201400438.

(136) Engish, L.; Rintoul, L.; Fredericks, P. Digital Printing of SERS Active Texture via Inkjet Technology. In *24th Internationational Conference on Digital Printing Technologies/Digital Fabrication*; SchulzeHagenest, D., Ed.; Society for Imaging Science and Technology: Pittsburgh, PA, 2008; p 265.

(137) Yu, W. W.; White, I. M. Inkjet-Printed Paper-Based SERS Dipsticks and Swabs for Trace Chemical Detection. *Analyst* **2013**, *138* (4), 1020–1025. https://doi.org/10.1039/C2AN36116G.

(138) Yu, W. W.; White, I. M. Chromatographic Separation and Detection of Target

Analytes from Complex Samples Using Inkjet Printed SERS Substrates. *Analyst* **2013**, *138* (13), 3679–3686. https://doi.org/10.1039/c3an00673e.

(139) Hoppmann, E. P.; Yu, W. W.; White, I. M. Highly Sensitive and Flexible Inkjet Printed SERS Sensors on Paper. *Methods* **2013**, *63* (3), 219–224. https://doi.org/10.1016/j.ymeth.2013.07.010.

(140) Eshkeiti, A.; Narakathu, B. B.; Reddy, A. S. G.; Moorthi, A.; Atashbar, M. Z.; Rebrosova, E.; Rebros, M.; Joyce, M. Detection of Heavy Metal Compounds Using a Novel Inkjet Printed Surface Enhanced Raman Spectroscopy (SERS) Substrate. *Sensors Actuators B Chem.* **2012**, *171–172*, 705–711. https://doi.org/10.1016/j.snb.2012.05.060.

(141) Wang, J.; Yang, L.; Liu, B.; Jiang, H.; Liu, R.; Yang, J.; Han, G.; Mei, Q.; Zhang, Z. Inkjet-Printed Silver Nanoparticle Paper Detects Airborne Species from Crystalline Explosives and Their Ultratrace Residues in Open Environment. *Anal. Chem.* **2014**, *86* (7), 3338–3345. https://doi.org/10.1021/ac403409q.

(142) Yorov, K. E.; Grigorieva, A. V; Sidorov, A. V; Polyakov, A. Y.; Sukhorukova, I. V; Shtansky, D. V.; Grünert, W.; Goodilin, E. A. Inkjet Printing of Silver Rainbow Colloids for SERS Chips with Polychromatic Sensitivity. *RSC Adv.* **2016**, *6* (19), 15535–15540. https://doi.org/10.1039/C5RA25907J.

(143) Environmental Protection Agengy (USA). EPA R.E.D. FACTS. Prevention, Pesticides and Toxic Substances (7508C). EPA 738-F-04-010. 2004.

(144) Turkevich, J.; Hillier, J. Electron Microscopy of Colloidal Systems. *Anal. Chem.* **1949**, *21* (4), 475–485. https://doi.org/10.1021/ac60028a009.

(145) Jana, N. R.; Gearheart, L.; Murphy, C. J. Seeding Growth for Size Control of 5−40 Nm Diameter Gold Nanoparticles. *Langmuir* **2001**, *17* (22), 6782–6786. https://doi.org/10.1021/la0104323.

(146) Moreira, R.; Chenlo, F.; Legall, D. Kinematic Viscosity and Refractive Index of Aqueous Solutions of Ethanol and Glycerol. *Ind. Eng. Chem. Res.* **2009**, *48* (4), 2157–2161. https://doi.org/10.1021/ie801410d.

(147) Joshi, P.; Santhanam, V. Paper-Based SERS Active Substrates on Demand. *RSC Adv.* **2016**, *6* (72), 68545–68552. https://doi.org/10.1039/C6RA07280A.

(148) Bajpai, P. *Pulp and Paper Industry: Chemicals*, 1st ed.; Elsevier, 2015.

(149) *Paper Chemistry*, 1st ed.; Roberts, J. C., Ed.; Springer: Dordrecht, 1991. https://doi.org/10.1007/978-94-011-6474-0.

(150) Zhao, L.-B.; Chen, J.-L.; Zhang, M.; Wu, D.-Y.; Tian, Z.-Q. Theoretical Study on Electroreduction of p -Nitrothiophenol on Silver and Gold Electrode Surfaces. *J. Phys. Chem. C* **2015**, *119* (9), 4949–4958. https://doi.org/10.1021/jp512957c.

(151) Skadtchenko, B. O.; Aroca, R. Surface-Enhanced Raman Scattering of p-Nitrothiophenol: Molecular Vibrations of Its Silver Salt and the Surface Complex Formed on Silver Islands and Colloids. *Spectrochim. Acta Part A Mol. Biomol. Spectrosc.* **2001**, *57* (5), 1009–1016. https://doi.org/10.1016/S1386-1425(00)00415-7.

(152) Cañamares, M. V.; Chenal, C.; Birke, R. L.; Lombardi, J. R. DFT, SERS, and Single-Molecule SERS of Crystal Violet. *J. Phys. Chem. C* **2008**, *112* (51), 20295–20300. https://doi.org/10.1021/jp807807j.

(153) Litz, J. P.; Camden, J. P.; Masiello, D. J. Spatial, Spectral, and Coherence Mapping of Single-Molecule SERS Active Hot Spots via the Discrete-Dipole Approximation. *J. Phys. Chem. Lett.* **2011**, *2* (14), 1695–1700. https://doi.org/10.1021/jz200743t.

(154) Kleinman, S. L.; Sharma, B.; Blaber, M. G.; Henry, A.-I.; Valley, N.; Freeman, R. G.; Natan, M. J.; Schatz, G. C.; Van Duyne, R. P. Structure Enhancement Factor Relationships in Single Gold Nanoantennas by Surface-Enhanced Raman Excitation Spectroscopy. *J. Am. Chem. Soc.* **2013**, *135* (1), 301–308. https://doi.org/10.1021/ja309300d.

(155) Rycenga, M.; Hou, K. K.; Cobley, C. M.; Schwartz, A. G.; Camargo, P. H. C.; Xia, Y. Probing the Surface-Enhanced Raman Scattering Properties of Au–Ag Nanocages at Two Different Excitation Wavelengths. *Phys. Chem. Chem. Phys.* **2009**, *11* (28), 5903–5908. https://doi.org/10.1039/b903533h.

(156) Fan, M.; Brolo, A. G. Silver Nanoparticles Self Assembly as SERS Substrates with near Single Molecule Detection Limit. *Phys. Chem. Chem. Phys.* **2009**, *11*, 7381–7389. https://doi.org/10.1039/b904744a.

(157) Kang, J. S.; Hwang, S. Y.; Lee, C. J.; Lee, M. S. SERS of Dithiocarbamate Pesticides Adsorbed on Silver Surface; Thiram. *Bull. Korean Chem. Soc.* **2002**,

23 (11), 1604–1610. https://doi.org/10.5012/bkcs.2002.23.11.1604.

(158) Ouyang, L.; Dai, P.; Yao, L.; Zhou, Q.; Tang, H.; Zhu, L. A Functional Au Array SERS Chip for the Fast Inspection of Pesticides in Conjunction with Surface Extraction and Coordination Transferring. *Analyst* **2019**, *144* (18), 5528–5537. https://doi.org/10.1039/C9AN01123D.

(159) Dendramis, A. L.; Schwinn, E. W.; Sperline, R. P. A Surface-Enhanced Raman Scattering Study of CTAB Adsorption on Copper. *Surf. Sci.* **1983**, *134* (3), 675–688. https://doi.org/10.1016/0039-6028(83)90065-1.

(160) Milliken, S.; Fraser, J.; Poirier, S.; Hulse, J.; Tay, L.-L. Self-Assembled Vertically Aligned Au Nanorod Arrays for Surface-Enhanced Raman Scattering (SERS) Detection of Cannabinol. *Spectrochim. Acta Part A Mol. Biomol. Spectrosc.* **2018**, *196*, 222–228. https://doi.org/10.1016/j.saa.2018.01.030.

(161) Sánchez-Cortés, S.; Domingo, C.; García-Ramos, J. V.; Aznárez, J. A. Surface-Enhanced Vibrational Study (SEIR and SERS) of Dithiocarbamate Pesticides on Gold Films. *Langmuir* **2001**, *17* (4), 1157–1162. https://doi.org/10.1021/la001269z.

(162) Li, P.; Liu, H.; Yang, L.; Liu, J. The Time-Resolved D-SERS Vibrational Spectra of Pesticide Thiram. *Talanta* **2013**, *117*, 39–44. https://doi.org/10.1016/j.talanta.2013.08.050.

(163) Environmental Protection Agengy (USA). Code of Federal Regulations. Part 180 - Tolerances and Exemptions for Pesticide Chemical Residues in Food. 2014.

(164) Weng, G.; Yang, Y.; Zhao, J.; Zhu, J.; Li, J.; Zhao, J. Preparation and SERS Performance of Au NP/Paper Strips Based on Inkjet Printing and Seed Mediated Growth: The Effect of Silver Ions. *Solid State Commun.* **2018**, *272*, 67–73. https://doi.org/10.1016/j.ssc.2018.01.014.

(165) Zhu, J.; Chen, Q.; Kutsanedzie, F. Y. H.; Yang, M.; Ouyang, Q.; Jiang, H. Highly Sensitive and Label-Free Determination of Thiram Residue Using Surface-Enhanced Raman Spectroscopy (SERS) Coupled with Paper-Based Microfluidics. *Anal. Methods* **2017**, *9* (43), 6186–6193. https://doi.org/10.1039/C7AY01637A.

(166) Wei, W.; Du, Y.; Zhang, L.; Yang, Y.; Gao, Y. Improving SERS Hot Spots for On-

Site Pesticide Detection by Combining Silver Nanoparticles with Nanowires. *J. Mater. Chem. C* **2018**, *6* (32), 8793–8803. https://doi.org/10.1039/C8TC01741G.

(167) Zhang, M.; Yang, J.; Wang, Y.; Sun, H.; Zhou, H.; Liu, X.; Ye, C.; Bao, Z.; Liu, J.; Wu, Y. Plasmon-Coupled 3D Porous Hotspot Architecture for Super-Sensitive Quantitative SERS Sensing of Toxic Substances on Real Sample Surfaces. *Phys. Chem. Chem. Phys.* **2019**, *21* (35), 19288–19297. https://doi.org/10.1039/C9CP03058A.

(168) Yu, Y.; Zeng, P.; Yang, C.; Gong, J.; Liang, R.; Ou, Q.; Zhang, S. Gold-Nanorod-Coated Capillaries for the SERS-Based Detection of Thiram. *ACS Appl. Nano Mater.* **2019**, *2* (1), 598–606. https://doi.org/10.1021/acsanm.8b02075.

APPENDIX A

SUPPLEMENTARY MATERIAL OF CHAPTER 2

Table A.1. Volume of the digested samples used for the preparation of the final solution (10 mL in deionized water) for the gold quantification by ICP OES and ICP-MS.

Sample	Technique	Volume of sample for 10 mL of solution in deionized water[a]
AuNR-total/AuNR-res	ICP OES	2.0 mL
	ICP-MS	60.0 µL
AuNR-sup	ICP OES/ICP-MS	4.0 mL
AuNR_Core	ICP-MS	50.0 µL
Au@AgNR	ICP-MS	350.0 µL

[a] Note that all digested samples were previously diluted up to 25 mL with ultrapure water after the microwave-assisted decomposition procedure.

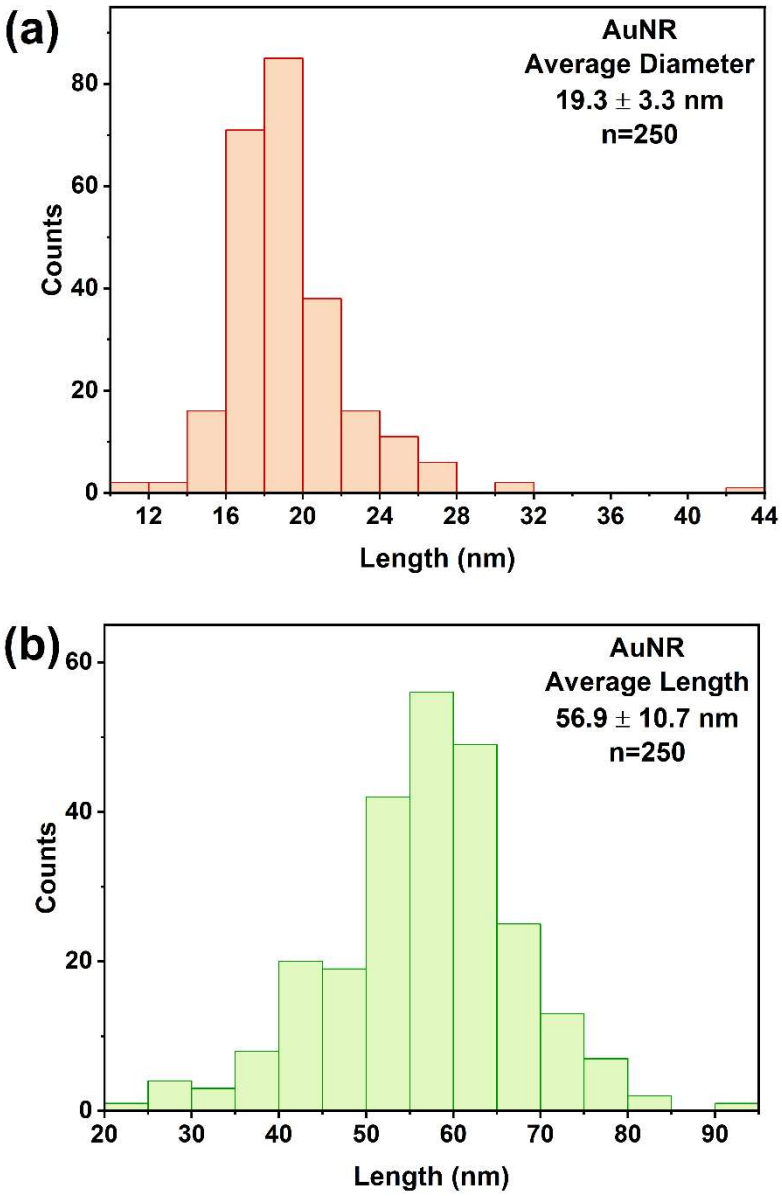

Figure A.1. Histogram of the (a) diameter and (b) length of the AuNR.

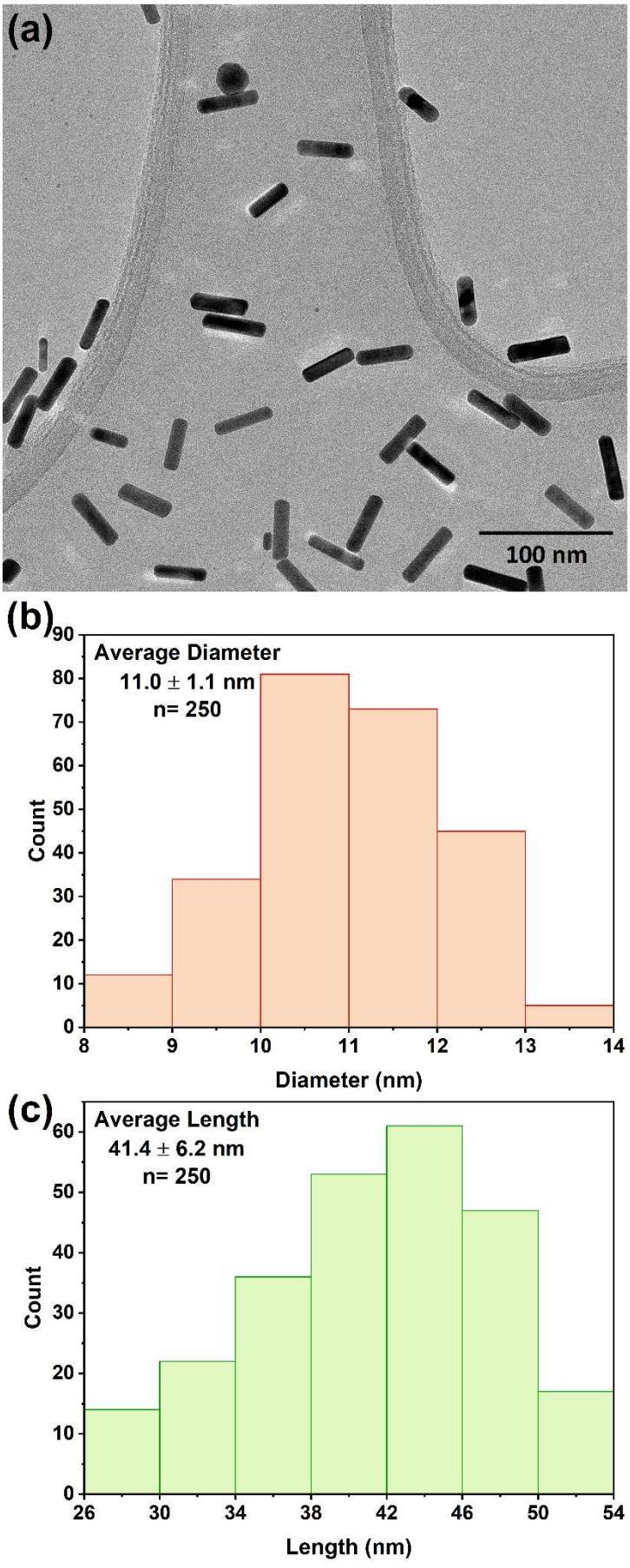

Figure A.2. (a) TEM image and histograms of (b) diameter and (c) length of AuNR_Core.

Naiara Vieira Godoy

Condition of the AuNR synthesis for the optimization of the centrifugation time shown in Figure 2.2a

AuNR was synthesized via a seed-mediated growth method following the procedure reported by Xu et al.[90] First, AuSeed nanoparticles were synthesized. In a round-bottom flask immersed in a water bath at 28 °C, 40.5 µL 1 % (w/v) $HAuCl_4$ was added to 4 mL 0.1 mol L^{-1} CTAB under stirring. Then, 24 µL 0.1 mol L^{-1} $NaBH_4$ was added to this solution. The stirring was stopped after 2 min and the colloid was aged at least for 2 h.

The second step consists of AuNR growth. 50 mL 0.1 mol L^{-1} CTAB, 30 µL 0.1 mol L^{-1} $AgNO_3$, and 1.03 mL 24.28 mmol L^{-1} $HAuCl_4$ were added in a round-bottom flask immersed in a water bath at 28 °C. Next, 163 µL 1 mol L^{-1} NaOH and 27.5 µL 30 % H_2O_2 were added and the solution was stirred for 1 min 150 µL of the seed colloid was added and the stirring was maintained for 30 s. The stirring was stopped, and the solution was kept at 28 °C at least for 1.5 h.

Table A.2. Instrumental parameters and measurement conditions for the gold quantification by ICP OES and ICP-MS.

ICP OES			
Instrumental parameters		*Measurements*	
Spray chamber	Cyclonic	Plasma view	Axial
Nebulizer	Meinhard®	Line, λ (nm)	242.7
Radiofrequency power (W)	1300	Replicates	3
Nebulizer Ar flow-rate ($L\ min^{-1}$)	0.45		
Auxiliary Ar flow-rate ($L\ min^{-1}$)	0.5		
ICP-MS			
Instrumental parameters		*Measurements*	
Spray chamber	Cyclonic	Scan mode	Peak hoping
Nebulizer	Meinhard®	Dwell time (s)	100
Radiofrequency power (W)	1200	Delay time (ns)	60
Nebulizer Ar flow-rate ($L\ min^{-1}$)	0.75	Sweeps	50
Auxiliary Ar flow-rate ($L\ min^{-1}$)	1.0	Integration time (ms)	5000
		m/z monitored	$^{197}Au^{+}$
		Replicates	5

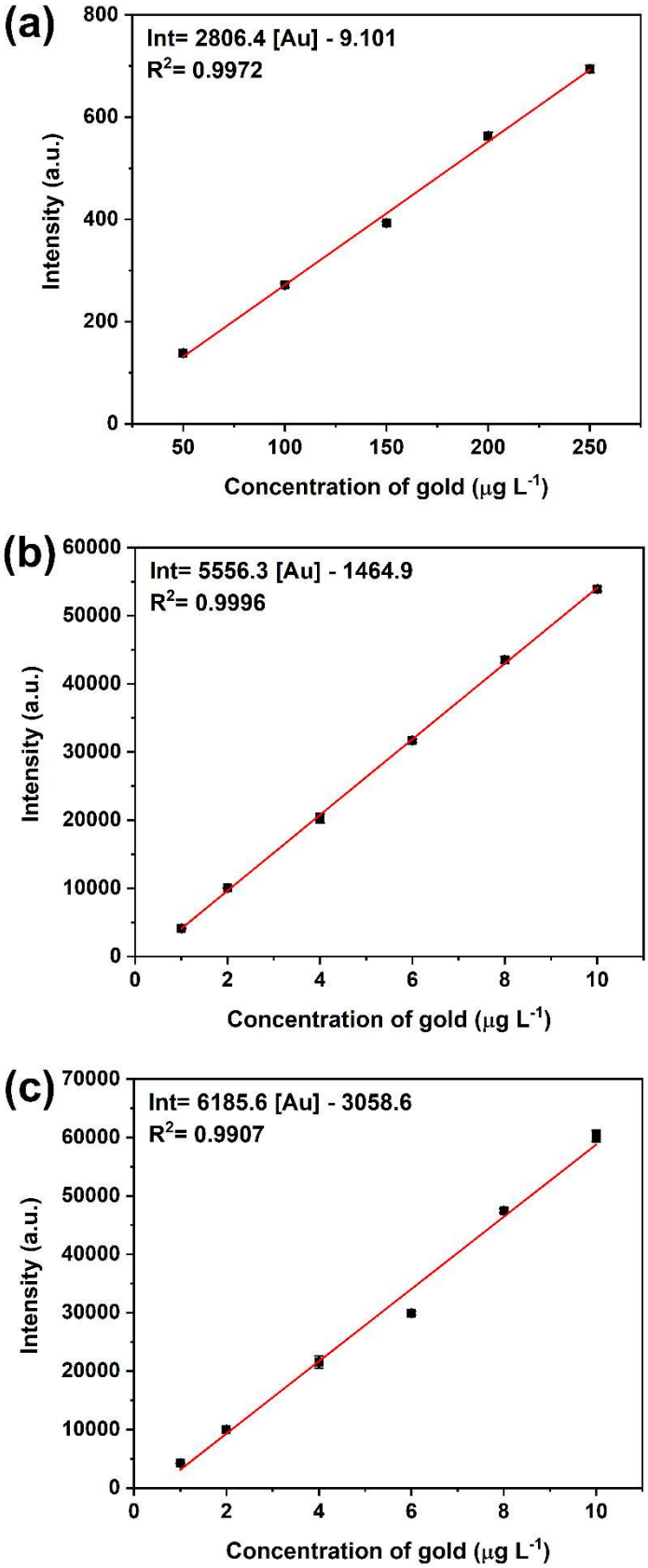

Figure A.3. Calibration curves of intensity versus concentration of gold used for the gold quantification of AuNR fractions by (a) ICP OES and (b) ICP-MS, and (c) AuNR_Core, Au@AgNR and AuSph fractions by ICP-MS.

Naiara Vieira Godoy

APPENDIX B

SUPPLEMENTARY MATERIAL OF CHAPTER 3

Determination of AuSeed volume for the AuSph growth

The theoretical equation for the determination of AuSeed volume needed for the AuSph growth is based on works in the literature[144,145] and it is described as follow:

$$D_{Final} = D_{Seed}\left[\frac{\left(V_{Au^+}[Au^+]/V_{Final}\right) + \left(V_{Seed}[Seed]/V_{Final}\right)}{V_{Seed}[Seed]/V_{Final}}\right]^{1/3} \quad \text{(B.1)}$$

where D_{Final} is the final diameter of the AuSph, D_{Seed} is the AuSeed diameter, V_{Au^+} and $[Au^+]$ are respectively the volume and concentration of Au^+ precursor ($HAuCl_4$), V_{Seed} and $[Seed]$ are respectively the volume and concentration of AuSeed (in terms of Au^0), and V_{Final} is the reaction volume. To calculate the AuSeed volume needed, the Equation (1) is rearranged into Equation (2):

$$V_{Seed} = \frac{\frac{D_{Seed}{}^3 V_{Au^+}[Au^+]}{D_{Final}{}^3 - D_{Seed}{}^3}}{[Seed]} \quad \text{(B.2)}$$

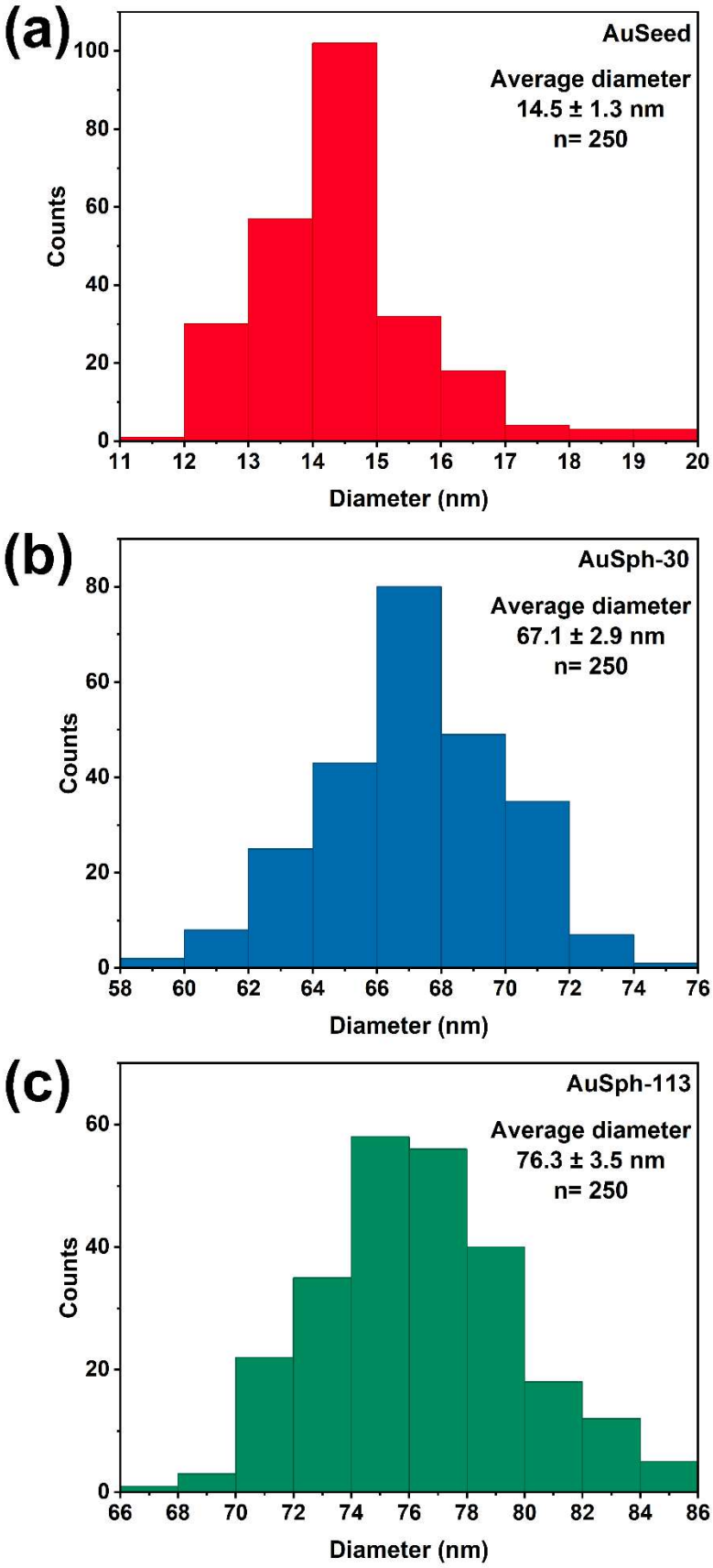

Figure B.1. Histogram of the diameter of (a) AuSeed, (b) AuSph-30 and (c) AuSph-113.

Determination of the nanoparticle concentration in AuSph Inks

The nanoparticle concentration (nanoparticles L^{-1}) in the AuSph Inks was determined according to Eq.(B.3):

$$\text{Nanoparticle concentration} = \frac{Mm_{Au}\,[Au^0]_{Ink}}{m_{Au/NP}} \quad \text{(B.3)}$$

where Mm_{Au} is the molar mass of Au, $[Au^0]_{Ink}$ is the Au^0 concentration of the AuSph ink, and $m_{Au/NP}$ is the mass of Au^0 per nanoparticle, which is determined according to Eq.(B.4).

$$m_{Au/NP} = V_{sphere}\, d_{Au} \quad \text{(B.4)}$$

where V_{sphere} is the volume of a sphere and d_{Au} is the density of gold (19.3 g cm^3). V_{sphere} is calculated according to Eq.(B.5), where the average diameter of the nanosphere (D_{sphere}) is determined by TEM analysis.

$$V_{sphere} = \frac{4}{3}\pi\left(\frac{D_{sphere}}{2}\right)^3 \quad \text{(B.5)}$$

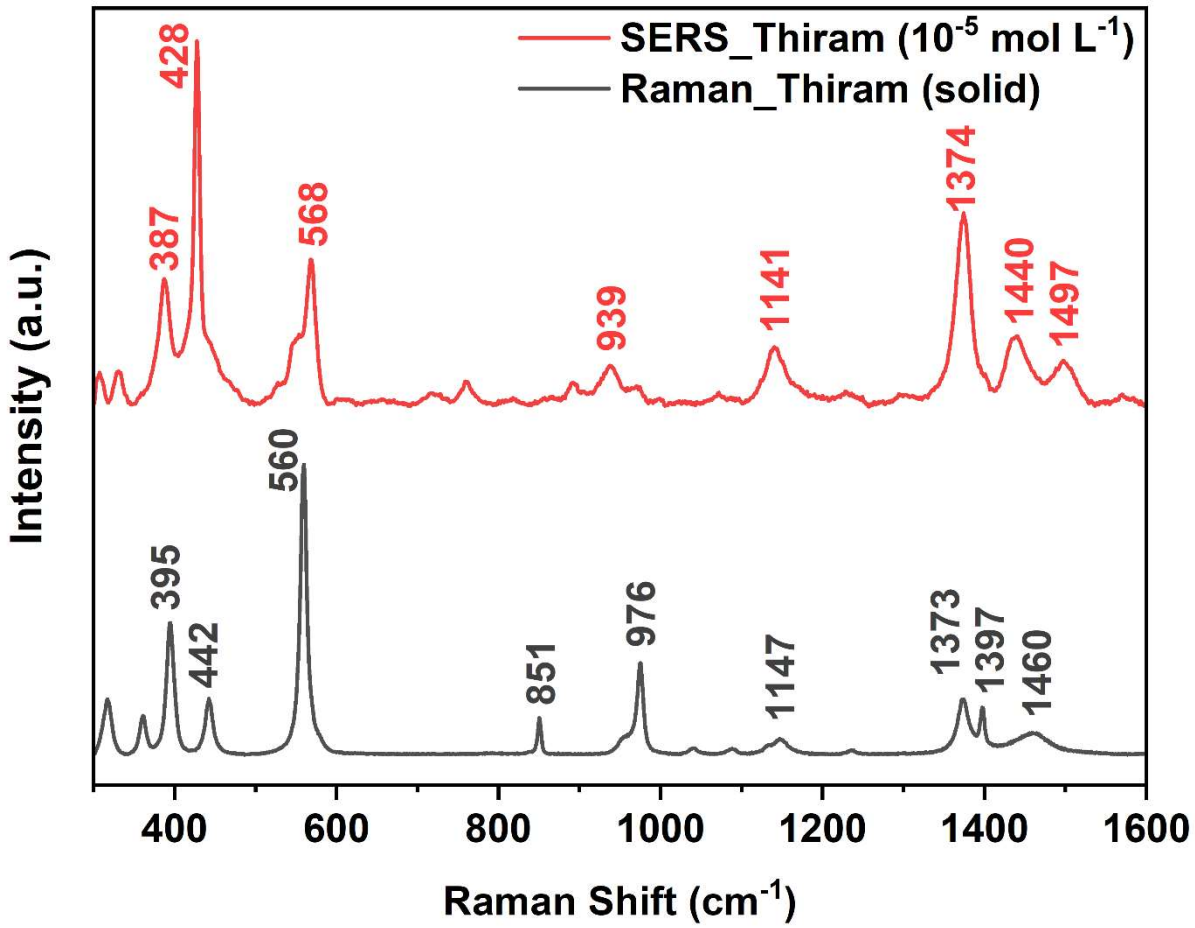

Figure B.2. Raman and SERS spectra of thiram. Raman spectrum of thiram (solid) was acquired with a 100x objective and 785 nm laser line with a maximum power density of 215.52 kW cm^{-2}, acquisition time 10 s, and 2 accumulations. The SERS spectrum of 2 µL thiram 10^{-5} mol L^{-1} on an inkjet-printed spot with five printing cycles was acquired with a 100x objective and 785 laser line with a maximum power density of 21.89 kW cm^{-2}, an acquisition time of 10 s, and 3 accumulation.

Table B.1. Raman and SERS vibrational assignments of pristine thiram (solid) and aqueous solution (10^{-5} mol L^{-1}) deposited on the inkjet-printed spot, respectively.

Raman (cm^{-1})	**SERS (cm^{-1})**	**Assignment**[157,158]
395	387	ν_{st}(CSS), $\delta((CH_3)_2N)$, ν_{st}(C=S)
442	428	$\delta(CH_3NC)$, ν_{st}(C=S)
560	568	ν_{st}(SS)
851	–	$\nu_{st}(CH_3N)$
–	939	$\nu_{st}(CH_3N)$, ν_{st}(C=S)
976	–	$\nu_{st}(CH_3N)$, ν_{st}(C=S) or ν_{as}(CSS)
1147	1141	$\nu_{st}(CN)$, $\rho(CH_3)$
1373	1374	$\delta(CH_3)$, $\nu_{st}(CN)$
1397	–	$\delta_{as}(CH_3)$
1460	1440	$\delta(CH_3)$
–	1497	$\nu_{st}(CN)$, $\delta(CH_3)$, $\rho(CH_3)$

δ= deformation, ν_{st} = stretching, ρ= rocking